

Crystallinity and Gas Barrier Properties in Compostable Polymer Films for Food Packaging: A Combined Simulation and Experimental Study

Nisha Middleton

University of Strathclyde Chemical and Process Engineering

Thesis submitted to the University of Strathclyde for the degree of Doctor of Philosophy

This thesis is the result of the author's original research. It has been composed by the author and has not been previously submitted for examination which has led to the award of a degree.

The copyright of this thesis belongs to the author under the terms of the United Kingdom Copyright Acts as qualified by University of Strathclyde Regulation 3.50. Due acknowledgement must always be made of the use of any material contained in, or derived from, this thesis.

Abstract

Polyhydroxyalkanoates (PHAs) are a promising class of sustainable plastics for food packaging, as environmentally friendly, compostable alternatives to conventional petroleum-based polymers. However, their barrier and mechanical properties are often limited by their crystallinity and microstructure. To address this, fillers and plasticisers are commonly added to modify these characteristics. This work investigates how such additives influence the structure, crystallinity, microstructure and ultimately the gas barrier and mechanical properties of PHAs.

Molecular dynamics simulations were used to provide insight into gas diffusion in crystal, amorphous and filled systems. First, a force field was modified to enable study of any combination of polyhydroxybutyrate (PHB), polyhydroxyvalerate (PHV) and their copolymers. This force field successfully reproduced experimental trends in density, surface energy and glass transition temperatures. The simulated lattice parameters for the PHB crystal were $a=5.86\pm0.15$ Å, $b=12.86\pm0.29$ Å and $c=6.02\pm0.12$ Å. For PHV, these were $a=9.67\pm0.19$ Å, $b=10.11\pm0.23$ Å and $c=5.63\pm0.11$ Å. Both sets of crystal parameters were in good agreement with experimental values. In terms of polymer dynamics, the amorphous PHB system simulated at 300 K was deemed to be in the glass phase, with reduced chain mobility compared to the melt phase at 500 K.

It was revealed, through computing diffusion coefficients (D), that PHB exhibits superior oxygen barrier performance compared to PHV, driven by its denser packing and cohesive interactions. In bulk amorphous PHB at 500 K, $D_{\rm H_2O} = 2.37 \pm 0.23$ and $D_{\rm O_2} = 3.76 \pm 0.25$ (\times 10⁻⁵ cm² s⁻¹). Water diffusion was slower than oxygen diffusion due to interactions between the polar water molecules and the ester groups on the PHA backbones. Simulations also demonstrated that crystalline domains inhibit the mobility of permeants, with negligible long-range diffusion for infinite and finite-chain crystals. The slower polymer chain dynamics in the presence of graphite caused a reduction in D for both oxygen and water. When the filler surface was added the diffusion coefficients were reduced, with $D_{\rm H_2O} = 1.63 \pm 0.36$ and $D_{\rm O_2} = 1.99 \pm 0.22$ (\times 10⁻⁵ cm² s⁻¹). The slower diffusion in filled systems was attributed to both reduced polymer mobility due to densification at the surface and the accumulation of permeants at the interface.

Experiments investigated thermal, mechanical and barrier properties of solvent-cast PHB films with added plasticiser triacetin and the filler boron nitride (BN). Incorporating triacetin reduced the melting temperature and increased distance to burst compared to pure PHB. However, plasticised films showed a poorer water barrier performance, indicated by a higher water permeability and lower water contact angles. BN acted as a nucleating agent, significantly enhancing crystallinity in all filled samples. The film containing only 0.06 wt% BN had an average crystalline content of 71.3 \pm 1.3 %, versus 41.0 \pm 2.5 % in pure PHB. While this low concentration of BN also improved the water barrier and mechanical performance (both strength and elasticity), higher BN content led to significantly increased water permeability, likely due to interfacial defects, highlighting the complex role of filler-polymer interactions.

Overall, this thesis provides useful insight and understanding into how molecular interactions and structural and interfacial features influence the functional performance of PHB-based materials. Taken together, the findings from simulations and experiment demonstrate that the barrier and mechanical performance of PHB-based films cannot be attributed to any single factor, but instead arise from the interplay between crystallinity, microstructure and additive interactions. By combining molecular simulation with experimental characterisation, this work provides an integrated framework for understanding and tailoring these interdependent effects, offering practical insight for the design of compostable polymer films that balance sustainability with the functional demands of food packaging.

Acknowledgements

First and foremost, I would like to thank my supervisors, Dr Karen Johnston and Dr Paul Mulheran, for giving me the opportunity to undertake this PhD and for their invaluable guidance, expertise and support throughout. I would also like to thank Dr Dominic Wadkin-Snaith for his patience and assistance in helping me debug my simulation issues.

I am grateful for the insightful input from the wider Smart Sustainable Plastic Packaging group, including Dr Vitor Magueijo from Chemical & Process Engineering and Prof John Liggat and Dr Katarzyna Majerczak from Pure & Applied Chemistry. Our discussions on sustainable polymers were invaluable to my research.

I would like to express my gratitude to the support team at the Archie-West HPC, particularly Dr Karina Kubiak-Ossowska, for providing such an essential service that enabled me to complete my simulation work and for promptly resolving any issues I encountered.

I also wish to thank Prof. James Elliot at the University of Cambridge for providing the PHB crystal structure file, which allowed me to conduct simulations on the crystal.

Last but not least, I would like to thank Robbie, Stuart and the rest of the department's PGR community. The lunches, after-work drinks and social events kept my spirits high throughout my PhD journey and made the department a genuinely enjoyable place to work. Good luck to all of you in completing your PhDs and in whatever comes next.

Introduction

The environmental impact of persistent plastic waste, particularly from single-use food packaging films, has driven the search for sustainable alternatives such as polyhydroxybutyrate (PHB), a type of polyhydroxyalkanoate (PHA). PHB has emerged as a promising material due to its compostability, biocompatibility and melt processability. However, PHB also presents challenges: it is brittle due to its high crystallinity and relatively high glass transition temperature $(T_{\rm g})$, has limited thermal stability near its melting point and displays a lower gas barrier compared to conventional synthetic polymers.

The properties of PHB depend on the crystallinity and microstructure, and can be altered by addition of plasticisers and fillers, and copolymerisation with the valerate monomer. This project investigated how the additives influence the microstructure and functional properties of PHAs, particularly in the context of gas barrier performance using a combined computational and experimental approach.

The computational work explored gas diffusion in amorphous and crystalline PHA systems, with and without filler surfaces. Experimental work probed how fillers and plasticisers affected the microstructure and barrier properties.

0.1 Layout of Thesis

Chapter 1 discusses widespread use of plastics in society and the environmental issues arising from their end-of-life disposal. Sustainable alternatives are then explored, with a focus on PHB and its microstructure and properties. A literature review of relevant PHB studies is presented, leading to the research aims and objectives of this project. Chapter 2 starts with an overview of molecular dynamics theory and describes the general simulation methodology used in this work. This is followed by a detailed description of the various experimental techniques employed. Chapter 3 presents the validation of the PHA force field model. Simulated properties of amorphous and crystalline PHAs are compared with experimental data from the literature, including amorphous and crystal structural properties and diffusion of water and oxygen in amorphous PHAs. Chapter 4 extends simu-

lation work to an investigation of how a filler surface incorporated into amorphous PHB affects gas diffusion. This chapter also includes results from simulations of water and oxygen diffusion in crystalline PHB. Chapter 5 presents experimental work on PHB films with and without additives. Thermal and mechanical properties, crystallinity and microstructure are characterised, and water permeation is measured. Finally, the overall conclusions and outlook are presented in Chapter 6.

0.2 Published Work

Chapter 3 is based on the following publication:

Middleton, N., Wadkin-Snaith, D., Mulheran, P., & Johnston, K. (2025). A versatile molecular dynamics force field for modelling polyhydroxyalkanoate structure and barrier properties. Macromolecular Theory and Simulations, e00048.

Contents

A	bstra	ıct	ii
A	ckno	wledgements	iv
Ir	trod	uction	\mathbf{v}
	0.1	Layout of Thesis	V
	0.2	Published Work	vi
\mathbf{L}	ist of	Figures	ix
L	ist of	Tables	xiv
1	Bac	ekground	2
	1.1	Plastic Waste and Life Cycle	2
	1.2	Sustainable Plastics	5
		1.2.1 Polyhydroxybutyrate	8
	1.3	PHB Properties	9
	1.4	Improving PHB Properties	12
		1.4.1 Copolymerisation	13
		1.4.2 Plasticiser Addition	14
		1.4.3 Filler Addition	15
	1.5	Project Aims and Objectives	16
2	Me	thodology	18
	2.1	Molecular Dynamics	18
		2.1.1 Force Field Models	20
		2.1.2 Force Fields Used in This Work	22
		2.1.3 Periodic Boundary Conditions	26
		2.1.4 Ensembles	26
		2.1.5 Thermostats and Barostats	27
		2.1.6 Energy Minimisation	28
	2.2	Experimental	29
		2.2.1 Film Preparation	29
		2.2.2. Characterisation Techniques	32

3		Versatile Molecular Dynamics Force Field for Modelling Poly-	
	•	Iroxyalkanoate Structure and Barrier Properties 42	
	3.1	Introduction	_
	3.2	Methodology	
		3.2.1 Force Field	
		3.2.2 Crystal Simulations	
		3.2.3 Amorphous Simulations	
		3.2.4 Diffusion Simulations	
	3.3	Results and Discussion	
		3.3.1 Crystal Properties	
		3.3.2 Amorphous Polymer Properties	
		3.3.3 Diffusion of Oxygen and Water Molecules 62	
	3.4	Summary and Conclusions 6	7
4	Wa	ter and Oxygen Diffusion in Crystalline and Filled Amorphous	
	Pol	yhydroxyalkanoates 69)
	4.1	Introduction)
	4.2	Methodology	2
		4.2.1 Crystalline Models	2
		4.2.2 Amorphous Model	3
		4.2.3 Filled Amorphous PHB	1
	4.3	Results and Discussion	ĵ
		4.3.1 Finite Chain Crystal Properties	3
		4.3.2 Diffusion in Crystalline Models	7
		4.3.3 Effect of Graphene Surface on Diffusion)
	4.4	Conclusions and Future Work	5
5	Cha	aracterisation of Solvent-Cast PHB Films 88	3
	5.1	Introduction	9
	5.2	Results and Discussion	1
		5.2.1 NMR	1
		5.2.2 Spherulitic Microstructure	1
		5.2.3 Crystallinity and Thermal Properties	1
		5.2.4 Water Barrier Properties	3
		5.2.5 Mechanical Properties	
		5.2.6 ANOVA Analysis of Measured Properties	
	5.3	Conclusions and Future Work	
6	Cor	aclusions 103	1
_	6.1	Summary of Results	
	6.2	Outlook and Future Work	

CONTENTS

\mathbf{A}	\mathbf{Add}	litional Force Field Details	105
	A.1	Partial Charges	105
		Force Field	105
		A.2.1 Water and Oxygen Models	106
		A.2.2 Bulk Water Properties	106
В	\mathbf{Add}	ditional Simulation Results	109
	B.1	Crystalline Systems	109
		B.1.1 Crystal Stability	109
		B.1.2 Surface Energy	110
		B.1.3 Lattice Energy	110
	B.2	Amorphous Polymer Simulations	111
		B.2.1 Structure and Conformation	111
		B.2.2 Dynamical Properties	112
		B.2.3 Glass Transition	113
	В.3	Diffusion Properties	113
	B.4	Finite Chain Crystal Model	115
	B.5	Graphene Systems	116
\mathbf{C}	Add	litional Experimental Results	118
		Water Barrier Properties	118
		C.1.1 Water Contact Angle	118
		C.1.2 WVTR and Permeability	118
	C.2	Crystallinity and Thermal Properties	118
	C.3	Mechanical Properties	118

List of Figures

1.1	Global plastic production in million metric tons from 1950 to 2023.	
	Data from Statista [1]	3
1.2	Composition of plastic packaging in kilotonnes that entered the	
	UK market in 2022 (left) and breakdown of films by polymer type	
	(right). Data from WRAP [2]	3
1.3	Classification of packaging polymers by origin and compostability.	
	Polyethylene terepthalate (PET), polyethylene (PE), polypropy-	
	lene (PP), polystyrene (PS), polybutylene adipate terephthalate	
	(PBAT), polycaprolactone (PCL), polylactic acid (PLA), polybuty-	
	lene succinate (PBS), polyhdroxyalkanoates (PHAs)	6
1.4	Chemical structure of PHAs. Different R side groups give a range	
	of polymers	7
1.5	PHB semi-crystalline microstructure. Adapted from Majerczak et	
	al.[3]	9
1.6	Oxygen and water barrier requirements for various food products,	
	MAP = modified atmosphere packaging. Obtained from Wang et	
	al. [4]	10
1.7	Comparison of water permeability of several packaging polymers.	
	Where provided by the authors, the test conditions are as follows:	
	cellulose 85% relative humidity (RH) [5], PCL 50% RH and 303 K	
	[6], PLA 50% RH and 303 K [6], PHB [7], PP 300 K and 21% RH	
	[8] and PET 298 K [9]	11
1.8	Chemical structure of isotactic PHVB copolymer, where ${f R}$ repre-	
	sents randomly ordered methyl and ethyl groups and the square	
	brackets denote individual monomers	13
2.1	Chain molecule showing bond length r_{23} , bond angle θ_{234} and di-	
	hedral torsional angle ϕ_{1234} [10]	21
2.2	Atom types used to represent a PHB molecule	23
2.3	(a) Water model and (b) oxygen model used in the current work.	$\frac{25}{25}$
2.4	Diagrammatic representation of periodic boundary conditions. Solid	
	outlines show the simulation box and particles, dashed lines repre-	
	sent the replicated images of the system	27
	1 0	

2.5 2.6	PHB film produced from solvent casting	30
~ _	T_{m2} curve	35
2.7 2.8	Contact angle formed at the solid/liquid/air interface Experimental set up used to determine water vapour permeability. The system is contained in an oven held at 298 K	37 38
2.9	Plot from texture analysis, with the peak indicating the breaking point of the film.	41
3.1	Chemical structure of (a) PHB (b) PHV	43
3.2	PHA trimer used for the calculation of partial charges. For PHB R is CH ₃ , and for PHV R is CH ₂ CH ₃	45
3.3	PHB α crystal, constructed using coordinates from ref [11]. Periodic bonding joins adjacent cells through the z axis	46
3.4	Snapshots of a single PHB chain and an amorphous PHB melt consisting of 50 chains, 10 monomers long	48
3.5	Histograms showing the four main backbone torsional angles along	
	the helical PHB backbone	53
3.6	PHB (left) and PHV (right) unit cells with periodic images shown. Non-bonded interactions between neighbouring chains which con-	
3.7	tribute to the surface energy are highlighted	54
	K, with $T_{\rm g}$ taken as the point of intersection. The uncertainty in $T_{\rm g}$ was calculated using the standard error of the gradient of the	56
3.8	best fit lines	90
	fits to results from current study: $R_{\rm e}=5.9~M^{0.5}$ and $R_{\rm g}=2.5~M^{0.5}$. The trendlines are extrapolated to $M=150$ for comparison	
	to literature results by Glova et al. [12]	58
3.9	δ vs M for PHAs from current study and literature. Dashed lines	
	show experimental values for PHB (blue) and PHV (green) [13]	60
3.10	MSDs of amorphous polymer systems with different chain lengths, run in NPT ensemble at 500 K and 1 atm	62
3.11	RMSDs of three water molecules within the immobilised PHB ma-	02
J.11	trix	64
3.12	MSDs of oxygen (orange) and water (blue) in amorphous PHB at (a) 300 K and (b) 500 K. Solid lines represent the $M=10$ polymer	01
	systems and dashed lines represent the $M=20$ systems	64

3.13	RDFs for permeant molecules around (a) the ester groups and (b) chain ends of the polymer molecules in the PHB $M=10$ system at $T=300$ K	65
3.14	MSDs of permeants in amorphous PHB and PHV. Simulations were carried out at 500K and results were averaged over two repeats.	66
4.1	(a) Infinite chain bulk crystal model. (b) Finite chain bulk crystal model	73
4.2	Graphene model with unit cells highlighted by green rhombus' with sides \mathbf{a}_1 and \mathbf{a}_2	74
4.3	AB stacking in multilayer graphite model	7 4 75
4.4	Torsional angles in the PHB backbone for finite and infinite chain crystalline systems. Averaged over 10 ns NPT run at 200 K and 1	10
4.5	atm	78
	meant diffusion in the amorphous polymer at 200 K is also plotted. Data has been averaged over two repeat simulations	79
4.6	Diffusion of (a) oxygen and (b) water molecules in finite chain crystals, showing total MSD and breakdown into each axis. Permeant diffusion in the amorphous polymer at 200 K is also plotted. Data	••
4.7	has been averaged over two repeat simulations	79
4.8	ers and (b) elongation of polymer chains at the surface (a) Polymer density in relation to the middle graphene sheet. Av-	81
4.0	eraged over 10 ns NVT simulation at 500 K. (b) Polymer density broken down into carbon, oxygen and hydrogen density. (c) Density	
	profiles of the carbonyl and ester oxygen atoms. (d) Snapshot showing proximity of carbonyl and ester oxygen atoms to the graphite	
	surface. σ is given in Å and ε in kcal mol ⁻¹	82
4.9	MSD of PHB in bulk system and graphite system during NPT simulation at 500 K and 1 atm	83
4.10	$x,\ y$ and z MSD components of water molecules in PHB/graphite	
4.11	system	84
	over three simulations	86
5.1	NMR spectra of purified PHB powder (in deuterated chloroform solution)	92
5.2	SEM images of PHB films.	93

5.3	Spherulite area analyses on SEM images of PHB_TA film. (a) Output of the Segment Anything tool [14] (b) Voronoi analysis using	
5.4	ImageJ software	94 95
5.5	Water barrier properties of PHB films	96
5.6	Snapshot from KRUSS Advance software, showing a water droplet	
	placed on a PHB film	97
5.7	Mechanical properties of PHB films	98
A.1	Partial charges for each monomer in the PHB trimer. Units for charge $= e$ (multiple of electron charge)	106
A.2	Partial charges for each monomer in the PHV trimer. Units for charge $= e$ (multiple of electron charge)	107
A.3	Simulation failure caused by H (white) and O (red) atoms on carboxylic end group collapsing into each other.	107
B.1	(a) PHB crystal backbone dihedral and (b) lattice parameter vari-	
	ation during an NPT simulation at 200 K and 1 atm	109
B.2	Variation in crystal unit cell dimensions with increasing tempera-	
	ture (a) PHB and (b) PHV. Sudden deviations from the equilibrium	
	cell lengths indicate thermal instability of the crystal	110
B.3	Surface energy of PHB as a function of (a) vacuum layer thickness	
D 4	Δ L and (b) slab thickness R , for both the (100) and (010) surfaces.	111
B.4	Surface energy of PHV as a function of (a) vacuum layer thickness	
Dr	Δ L and (b) slab thickness R , for both the (100) and (010) surfaces.	111
B.5	Lattice energy of polymer crystals, where ΔL is the change in box	110
$D \in$	length from the unit cell in x and y directions	112
B.6 B.7	End-to-end vector autocorrelation with fitted exponential decay. Block averaged density vs temperature on cooling $M=10$ chains	113
D.1	from 500 K to 100 K. The crosses mark the estimated $T_{\rm g}$ for each	
	polymer. Block averaging was used only for visualisation purposes.	112
B.8	Snapshot of water molecules (blue) within the amorphous PHB	110
D .0	matrix (orange)	114
B.9	(a) MSD data for oxygen in PHB with $M=10$ at 300 K, indicating	
2.0	the linear region in the middle of the graph used to compute the	
	diffusion coefficient. (b) log-log plot of MSD data, with slope ≈ 1	
	indicating diffusion is in Einstein regime [15]	115
B.10	(a) Infinite chain crystal containing five unit cells. (b) Finite chain	
	model with free chain ends. (c) Finite chain crystal replicated into	
	bulk slab.	115

B.11 Density profile plots from three water diffusion simulations.	Den-
sity data was sampled every 1 ns from a 100 ns production r	un in
the NVT ensemble at 500 K	116
B.12 Density profile plots from three oxygen diffusion simulations.	Den-
sity data was sampled every 1 ns from a 100 ns production r	un in
the NVT ensemble at 500 K	117

List of Tables

1.1	Classification of packaging polymers films based on recommendations from Wang et al. [4]	12
2.1 2.2 2.3	GAFF atom types used for building a model of PHB Formulations used for PHB films	23 32
	V_w are the mass and volume of water vapour, respectively, t is time, A and l are film area and thickness, respectively, and ΔP is the pressure difference of water vapour across the film	40
3.1	Crystal properties of energy minimised structures and NPT simulations at 200 K (averaged over 10 ns) compared with experimental properties. NPT data points were sampled every 1 ps and average values are reported \pm the standard deviation. Experimental densities were measured using the flotation method [16, 17] or calculated	
0.0	from reported lattice constants [11]	52
3.2 3.3	Comparison of PHB torsional angles (°) with literature data Density of amorphous PHAs, from current work and literature data.	52
5.5	All densities reported from the current work are averages from NPT	
3.4	runs, with standard deviations $\leq 0.01 \text{ g cm}^{-3}$	55 56
3.5	$T_{\rm g}$ of each amorphous system	50
5.5	reported characteristic ratios using equation 3.11	59
3.6	$E_{\rm coh}$ and δ for PHA systems from the present work computed at	00
	300 K and from literature. Results from present work were averaged	
	over three snapshots of a trajectory. Standard deviation $\leq 0.3 \text{ kJ}$	
	$\mathrm{mol}^{-1} \mathrm{mon}^{-1}$ for E_{coh} and $\leq 0.2 \mathrm{MPa}^{0.5}$ for δ	60
3.7	Polymer relaxation times τ ± standard deviation across multiple	
	simulation windows. Polymer self-diffusion coefficients D (500 K)	
	\pm standard error in slope of line fitted to MSD curves	61

3.8	Diffusion coefficients, D , computed from MSDs, and experimental results from literature [18, 19]. The uncertainty in D is the standard deviation of two repeat simulations at 500 K or three repeat simulations at 300 K	63
4.1	Comparison of density and lattice parameters in crystalline PHB models. Data was sampled every picosecond during a 10 ns NPT run at 200 K and 1 atm. Errors given are standard deviations of	
4.2	the measured data	77 80
4.3	Diffusion coefficients of water and oxygen in bulk PHB and PHB/grap system. Average of three repeat runs \pm standard deviation. Simulations were run in the NVT ensemble at 500 K	
5.1	Thermal properties of PHB films. Results are an average of three repeats \pm the standard deviation. Values for each repeat are listed in Appendix C	95
5.25.3	Water barrier properties of PHB films. WVTR and permeability are an average of three tests \pm standard deviation. θ values are an average of five tests \pm standard deviation. Individual measurements are listed in Appendix C	96
5.4	average of five repeats. Individual measurements can be found in Appendix C	98 99
A.1 A.2 A.3	Force field parameters for SPC/E water model [20, 21] Force field parameters for Javanainen oxygen model [22] Properties of liquid water using the SPC/E model in the current work compared to simulation results from literature [20] and the experimentally measured density [23] and diffusion coefficient [24].	108 108
В.1	Chain conformation properties of amorphous PHB, PHV and PHVB at 500 K.	112
B.2	Density (ρ) of M -monomer systems at a temperature of 300 K or 500 K. Standard deviation in all systems is ≤ 0.01 g cm ⁻³	114
C.1 C.2 C.3 C.4	Contact angle of water droplet placed on film surface	119 119 120 120
C.5	Water barrier properties of PHB + 1 wt % BN	120

C.6 Water barrier properties of PHB $+$ 0.25 wt $\%$ BN	121
C.7 Water barrier properties of PHB $+$ 0.0625 wt $\%$ BN	121
C.8 Water barrier properties of PET	121
C.9 Thermal properties and crystallinity of neat PHB	121
C.10 Thermal properties and crystallinity of PHB $+$ 10 wt $\%$ TA	122
C.11 Thermal properties and crystallinity of PHB $+$ 10 wt $\%$ TA $+$ 1	
wt % BN	122
C.12 Thermal properties and crystallinity of PHB $+$ 1 wt $\%$ BN	122
C.13 Thermal properties and crystallinity of PHB + 0.25 wt $\%$ BN	122
C.14 Thermal properties and crystallinity of PHB + 0.0625 wt $\%$ BN	123
C.15 Force and distance to burst of neat PHB	123
C.16 Force and distance to burst of PHB + 10 wt $\%$ TA	123
C.17 Force and distance to burst of PHB $+$ 10 wt % TA $+$ 1 wt % BN.	124
C.18 Force and distance to burst of PHB $+$ 1 wt $\%$ BN	124
C.19 Force and distance to burst of PHB + 0.25 wt $\%$ BN	124
C.20 Force and distance to burst of PHB + 0.0625 wt % BN	125

Chapter 1

Background

1.1 Plastic Waste and Life Cycle

Since their large-scale commercial introduction in the mid-20th century, plastics have transformed nearly every aspect of modern life. Their versatility, durability and low production cost have made them indispensable across a wide range of industries, from construction and automotive manufacturing to electronics and healthcare. In particular, the packaging sector has seen a dramatic shift away from metal and glass towards plastic materials, driven by their ability to provide lightweight, flexible and protective solutions at low cost. As demand for convenience and longer shelf life has grown, so too has the reliance on plastic packaging, especially single-use items. This widespread adoption has led to continual growth in global plastic production over the past few decades, with significant environmental implications. In 2022 global plastic production surpassed 400 million metric tonnes, with less than 10% of this being made from recycled content [25]. Figure 1.1 shows the increase in global plastic production from 1950 to 2023 [1]. It is estimated that 22% of plastic worldwide is either not collected, disposed of improperly or ends up as litter [26].

Packaging represents a large share of this global plastic use, much of it in the form of single-use items derived from non-renewable petrochemicals. In the UK alone, approximately 1.3 million tonnes of consumer plastic packaging were placed on the market in 2022 [2]. Of this, around 337,000 tonnes were films and flexibles (see Figure 1.2), which are particularly problematic due to their high prevalence in food, retail and e-commerce packaging, combined with their low recyclability.

A significant proportion of these films and flexibles are used specifically in food packaging applications, where they are typically made from polymers such as polypropylene (PP), polyethylene (PE) and polyethylene terephthalate (PET). These materials are valued for their combination of functional and processing ad-

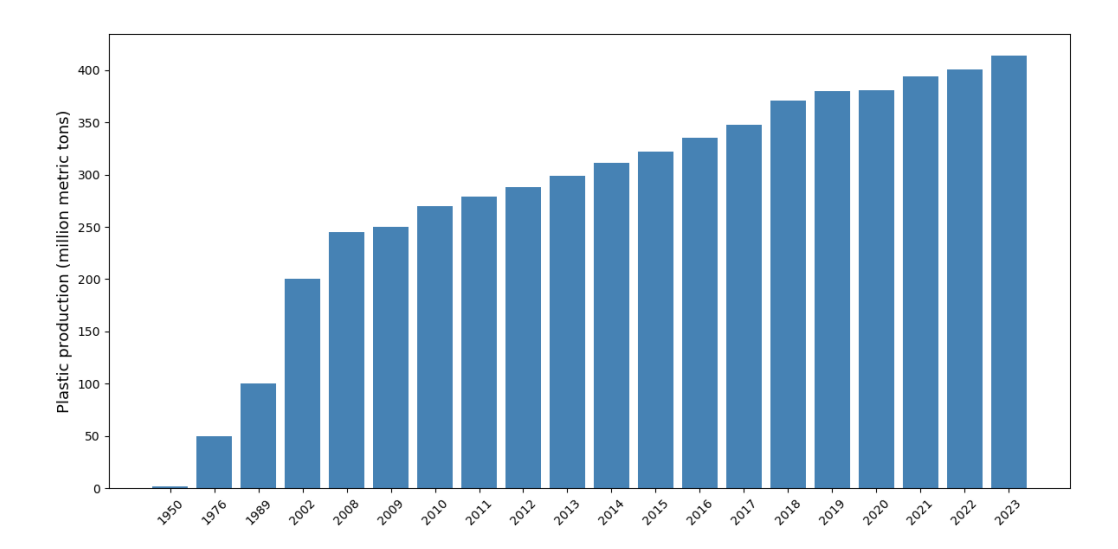


Figure 1.1: Global plastic production in million metric tons from 1950 to 2023. Data from Statista [1].

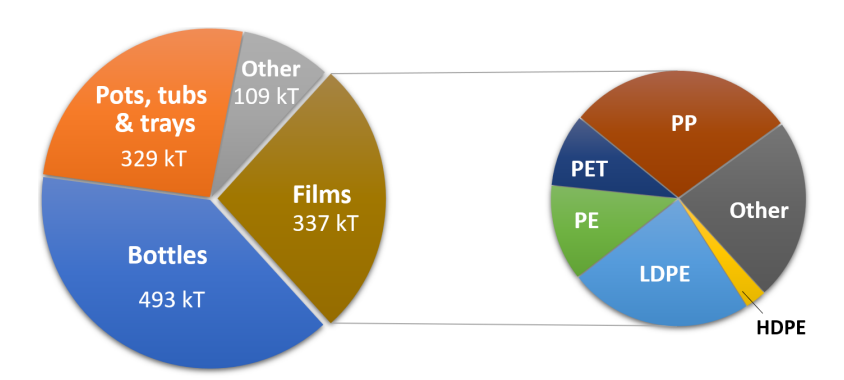


Figure 1.2: Composition of plastic packaging in kilotonnes that entered the UK market in 2022 (left) and breakdown of films by polymer type (right). Data from WRAP [2].

vantages. They are easily shaped using industrial techniques such as melt extrusion and blown film processing, making them highly versatile and cost-effective for mass production. Their lightweight and flexible nature allows for efficient wrapping and sealing of irregularly shaped food products, helping to reduce material use and transportation costs. In addition, many packaging films offer good optical clarity, allowing consumers to visually inspect food before purchase, which can be a key requirement in retail settings. The ability to tailor the mechanical strength, sealing behaviour and appearance of these films has contributed to their dominance in the packaging industry. However, their persistence in the environment and challenges with end-of-life management have prompted increasing interest in

sustainable alternatives.

Recycling rates in the UK for post-consumer plastic films and flexible plastics remain very low due (around 7% [2]) to a range of technical, logistical and economic challenges [2]. These challenges begin at the collection stage. In most UK local authorities, flexible films are not accepted in kerbside recycling schemes, leaving front-of-store recycling (FOSR) as the primary disposal route for many households. While the number of participating retailers has increased, uptake remains limited; WRAP estimated that in 2023, only 1 in 5 UK citizens used FOSR to recycle their plastic film waste [2]. The lack of widespread, convenient collection infrastructure significantly reduces the volume and quality of recovered material.

Even if collection were to be improved, current recycling infrastructure presents further barriers. The physical properties of flexible films, particularly their low bulk density, make them difficult and inefficient to handle, transport and process [27]. Standard recycling equipment is typically designed for rigid plastics and is poorly suited to the characteristics of films, which are prone to clogging machinery and being misdirected in automated systems. In material recovery facilities, films are often misclassified or treated as contaminants and removed from the recycling stream entirely [27]. While technologies such as near-infrared sorting and ballistic separators can help identify plastic films, they often struggle with thin or multimaterial layers, reducing sorting accuracy and efficiency.

Another major obstacle is the complex composition of many flexible plastic films. These materials are often multilayered, combining two or more polymers, and sometimes non-plastic layers such as aluminium or paper, to achieve specific functional properties such as strength, sealability and barrier performance [2]. However, these multi-material combinations are incompatible with conventional mechanical recycling, as they are difficult to separate. Emerging techniques such as delamination and solvent-based recovery show promise, but are still at the development stage and have not yet been widely adopted at commercial scale [28].

Contamination poses an additional barrier to recycling success. Plastic films used in food and agricultural applications are frequently contaminated with food residues, inks, adhesives, coatings or soil, all of which reduce the quality of the recovered polymer and complicate the cleaning and reprocessing steps [28, 29]. Household-sourced films in particular tend to be highly contaminated due to a lack of source separation and inconsistent cleaning prior to disposal [29].

In summary, the low recycling rates of plastic films and flexible packaging can be attributed to collection limitations, handling difficulties, sorting inefficiencies, complex material compositions and widespread contamination. While research and pilot projects are underway to address these issues through chemical recycling and improved collection strategies, major technical and economic barriers remain before these materials can be effectively recycled at scale [28].

1.2 Sustainable Plastics

Reducing the use of plastic films, such as by removing packaging from food products and promoting the sale of loose items, is often presented as a way to mitigate plastic pollution. This has contributed to the rise of zero-waste and refill shopping models in towns and cities across the UK [30]. While this approach can reduce unnecessary packaging for dry goods and bulk groceries, it is less suitable for fresh and perishable produce. For these items, plastic packaging, particularly flexible films, plays a vital role in protecting against mechanical damage, contamination and moisture loss, while also extending shelf life by slowing spoilage. Eliminating plastic packaging from the fresh food supply chain could lead to increased food waste, both during transportation and after purchase. Food waste is not only a social and economic issue but also a major environmental concern, accounting for an estimated one third of all food produced globally and contributing 8-10% of global greenhouse gas emissions [31, 32]. When food is discarded, the embedded energy, water and land resources are also lost and if sent to landfill, it produces methane, a potent greenhouse gas with over 25 times the global warming potential of CO₂ [33]. Packaging that helps extend shelf life can therefore play a key role in reducing food-related emissions. In this context, rather than eliminating plastic films altogether, developing smarter and more sustainable packaging solutions may offer a more effective strategy for reducing both plastic pollution and food-related carbon emissions.

In the search for sustainable packaging solutions, terms like biodegradable and compostable are often used, however they are not interchangeable. A biodegradable polymer is one that can be broken down by microorganisms into natural substances such as water, carbon dioxide (or methane in anaerobic conditions) and biomass. However, the rate and conditions of biodegradation can vary greatly. Compostable polymers are a more specific category: they must not only biodegrade, but also do so under controlled conditions without leaving toxic residues. The European standard EN 13432 outlines the criteria for industrial compostability, requiring materials to disintegrate within 12 weeks and biodegrade by at least 90% within 180 days under controlled aerobic composting conditions at 331 K, with defined humidity and oxygen levels [34]. Home composting, by contrast, occurs at ambient temperatures and varies with climate, meaning only certain materials are suitable for effective breakdown outside of industrial facilities. Un-

derstanding these distinctions is essential for evaluating the environmental performance of compostable packaging and for ensuring compatibility with available waste management infrastructure.

It is also important to distinguish between bio-based and compostable polymers, as the two terms are often mistakenly used interchangeably. Bio-based polymers are derived from renewable biological sources such as corn starch, sugarcane or cellulose, rather than fossil fuels. However, being bio-based does not necessarily mean the material is biodegradable or compostable. Conversely, compostable polymers are capable of breaking down into natural elements under composting conditions, but they may still be derived from fossil resources. For example, some aliphatic polyesters made from petrochemicals are engineered to be biodegradable, such as polycaprolactone (PCL). Additionally, Bio-PE and Bio-PET are molecularly identical to their oil-derived counterparts but made from biomass feedstocks, so renewable in origin but not compostable. The intersection of these classifications can be summarised in a matrix of oil-derived vs bio-derived and compostable vs non-compostable materials, as shown in Figure 1.3.

	Oil-derived	Bio-derived
Non- compostable	PET PE PP PS	Bio-PET Bio-PE
Compostable	PBAT PCL	PLA Bio-PBS Polysaccharides PHAs

Figure 1.3: Classification of packaging polymers by origin and compostability. Polyethylene terepthalate (PET), polyethylene (PE), polypropylene (PP), polystyrene (PS), polybutylene adipate terephthalate (PBAT), polycaprolactone (PCL), polylactic acid (PLA), polybutylene succinate (PBS), polyhdroxyalkanoates (PHAs).

Among the growing class of bio-derived and compostable polyesters, several materials have emerged as promising candidates for sustainable packaging applications. Polysaccharide-based polymers consist of cellulose, starch, alginate and chitosan. These materials are typically home-compostable and are derived from abundant, renewable feedstocks. However, they tend to be sensitive to moisture

and can degrade prematurely in humid environments [4, 35]. While coating technologies have been developed to address this issue in food packaging applications, their stand-alone use in packaging is limited. One of the most commercially developed compostable polymers is polylactic acid (PLA), which is synthesised via the fermentation of sugars derived from renewable sources such as corn or sugarcane. PLA offers good clarity, stiffness and processability, making it suitable for rigid containers, films and thermoformed packaging [6]. However, it has limited flexibility and poor moisture barrier properties and its compostability typically requires industrial composting conditions [36]. Polybutylene succinate (PBS) is another polyester that can be synthesised from bio-based monomers. PBS exhibits good thermal stability and mechanical properties and it is more flexible than PLA, making it suitable for film applications [37]. While it is compostable, PBS production costs remain relatively high and its gas barrier properties are lacking [38]. Finally, polyhydroxyalkanoates (PHAs) represent a unique class of polyesters synthesised by various microorganisms as intracellular carbon and energy storage compounds. Commercially, they are typically produced through microbial fermentation, in which carbon-rich substrates are converted into polymer by specific bacteria. Altering the growing conditions used in production, such as the type of growth media, can produce different types of PHAs, each containing different side groups. To date, there are more than 150 types of PHAs known [39, 40]. The chemical structure of a PHA polymer is shown in Figure 1.4, where R is an alkyl group. In polyhydroxybutyrate (PHB) \mathbf{R} is CH_3 and in polyhydroxyvalerate (PHV) \mathbf{R} is $\mathrm{CH}_2\mathrm{CH}_3$.

Figure 1.4: Chemical structure of PHAs. Different \mathbf{R} side groups give a range of polymers.

As biodegradable and bio-based materials, PHAs have gained considerable interest for their potential use in sustainable food packaging. Their desirable properties, including moisture resistance, biocompatibility and mechanical strength comparable to conventional plastics, make them strong candidates to replace petrochemical-derived polymers. Furthermore, PHAs can be produced from low-value renewable resources such as agricultural and food waste streams, further enhancing their environmental appeal. In addition to their environmental benefits, PHAs have several technical properties that make it well suited for food packaging. As a thermoplastic, PHAs are compatible with conventional polymer

processing techniques such as extrusion and injection moulding [41], and they can be melted and remoulded, making them recyclable. Moreover, PHAs and their degradation products are naturally occurring in the human body, making them non-toxic and biocompatible [42], an important consideration for food contact materials.

1.2.1 Polyhydroxybutyrate

PHB is the most extensively studied member of the PHA family. First isolated and characterised in 1925 by microbiologist Maurice Lemoigne [43], PHB was identified as a bacterial energy storage compound, produced by organisms such as *Alcaligenes eutrophus* under nutrient-limited conditions. While it received little commercial interest initially, research into PHB's potential as a plastic alternative began to grow in the 1960s. By the 1980s, the British chemical company Imperial Chemical Industries had developed a pilot-scale plant to produce PHB, which was marketed under the brand name Biopol [44].

The microstructure of a polymer refers to its internal structural arrangement on the molecular and microscopic scale, including features such as crystalline domains, amorphous regions and spherulites. This microstructure plays a key role in determining a polymer's properties and is highly sensitive to how the material is processed. Polymer processing conditions such as cooling rates, presence of impurities and extrusion speed all influence the resulting microstructure. Therefore to ensure consistent material properties, it is crucial to precisely control processing parameters. PHB has a semicrystalline microstructure, with amorphous regions filling the gaps between the large spherulitic crystal structures. During the crystallisation process, polymer chains elongate from their randomly coiled amorphous state and adopt a helical configuration. The most common crystal polymorph of PHB is the $2_1 \alpha$ helix [45], consisting of two monomers per one twist of the helix. PHB is generally of high crystallinity owing to the close packing of the helical chains, mediated by electrostatic and van der Waals (vdW) forces, whereby disruption caused by the methyl side group is minimised. The β crystal form is less understood and remains the subject of discussion [3]. The elongated helices then organise into lamellae and chains can either fold back into the same crystalline region or extend into the surrounding amorphous phase. These lamellae stack into microfibrillar structures, which then grow radially to form larger spherulitic domains [46]. Spherulites can grow up to the millimetre scale and can be visible to the naked eye.

The amorphous polymer regions in close proximity to crystalline spherulites exhibit restricted chain mobility due to physical constraints imposed by the surrounding ordered structures [47]. This interfacial zone is referred to as the rigid

amorphous region. In this region, the polymer behaves more like a glassy material: molecular motion is significantly hindered, resulting in higher density, brittleness and low chain segmental mobility. The glass transition temperature $(T_{\rm g})$ can be observed experimentally as a step-change in a differential scanning calorimetry (DSC) curve, indicating a change in the polymer's heat capacity. Below $T_{\rm g}$, the amorphous phase is glassy, with properties such as reduced elongation at break, higher modulus and greater brittleness. Above $T_{\rm g}$, by contrast, the amorphous phase is rubbery, characterised by increased chain flexibility, higher impact resistance and enhanced ductility. Amorphous regions further from the crystalline domains retain greater molecular mobility and therefore behave more like the rubbery state above $T_{\rm g}$, making a greater contribution to the overall ductile behaviour of the polymer.

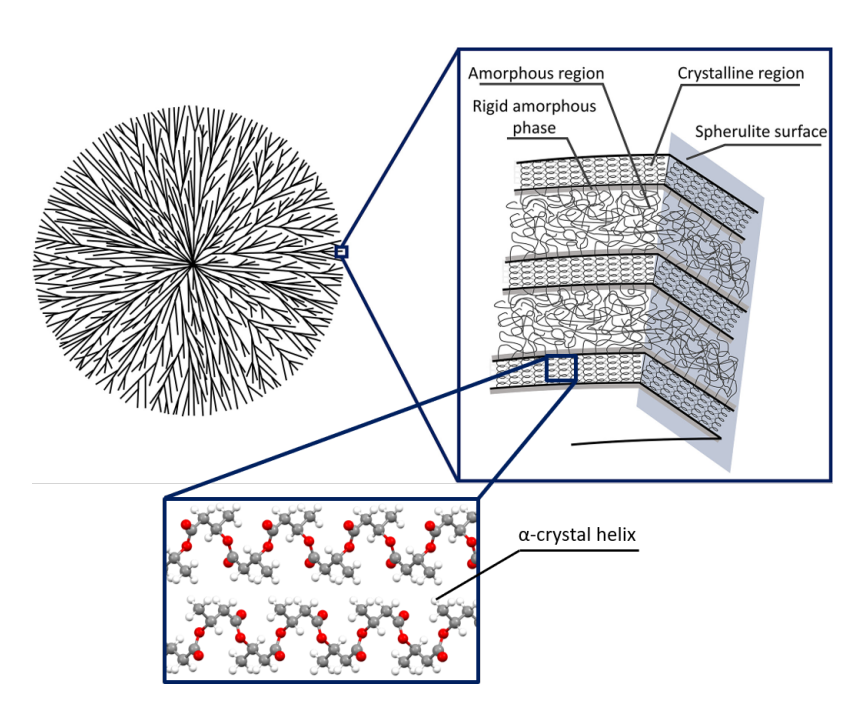


Figure 1.5: PHB semi-crystalline microstructure. Adapted from Majerczak et al.[3]

1.3 PHB Properties

A strong water and oxygen barrier in plastic food packaging is critical to maintaining the quality, safety and shelf life of food products. By preventing the ingress of moisture, effective water barrier materials protect food from spoilage, microbial growth and undesirable texture changes. This is particularly important for moisture-sensitive products such as dry snacks, cereals or powdered goods,

which can become clumpy or lose their crispness if exposed to humidity. Likewise, oxygen barrier performance is vital for slowing down oxidative reactions, such as rancidity in fats and oils, enzymatic browning and the growth of aerobic microorganisms. Oxygen-sensitive products like nuts, dairy and ready meals benefit significantly from reduced oxygen exposure. Figure 1.6 shows the packaging barrier requirements for various types of food products [4]. Additionally, water and oxygen barriers help prevent the loss of moisture from perishable items like fruits or baked goods, helping to retain freshness. Beyond product protection, robust barrier properties can reduce the need for additional packaging layers, thereby minimising material usage and waste. Thus, selecting plastics with strong water and oxygen barrier properties is essential for ensuring both functional performance and environmental efficiency in food packaging.

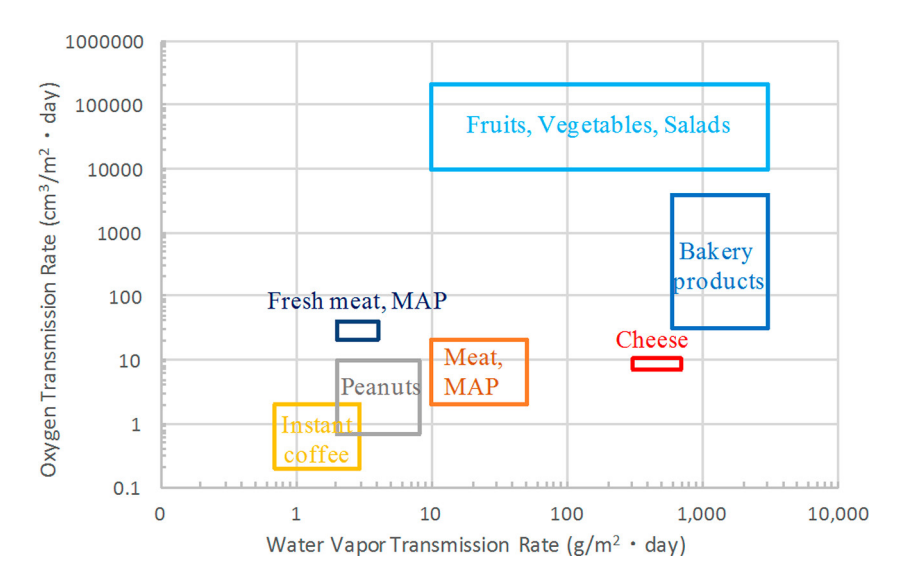


Figure 1.6: Oxygen and water barrier requirements for various food products, MAP = modified atmosphere packaging. Obtained from Wang *et al.* [4].

Figure 1.7 highlights significant differences in the water barrier properties of various packaging polymers, with PHB demonstrating intermediate performance. The polymers are graded poor to high barrier, based on classification recommended by Wang et al. in their study on barrier properties of cellulose films [4]. The permeability range for each grade is listed in Table 1.1. PP and PET exhibit the lowest permeability coefficients, at 766 [8] and 130 Barrer [9], respectively, indicating superior water barrier properties. These polymers are well-established in packaging applications due to their excellent moisture resistance, which is critical for protecting moisture-sensitive products. In contrast, cellulose exhibits the highest permeability at 7666 Barrer [5] due to its hydrophilic nature, rendering it a poor barrier to water vapour. PCL and PLA are considered low water barriers,

based on permeabilities reported by Siparsky et al. (4266 and 2933 Barrer, respectively) [6]. This limitation restricts their use in applications requiring robust moisture resistance unless additional coatings or treatments are applied. PHB, with a permeability of 1582 Barrer [7], is deemed a medium water barrier. It outperforms the other three compostable polymers but has a notably higher permeability than PET. PHB's water barrier properties are relatively aligned with those of PP, underscoring its potential as a viable alternative to conventional plastics, particularly in applications where moderate moisture resistance is sufficient. While its compostable nature offers a significant sustainability advantage, for applications requiring high moisture resistance, such as packaging for highly perishable goods, PHB may need enhancements, such as blending with other polymers, or applying barrier coatings. Overall, this data demonstrates that while PHB does not yet match the water barrier properties of PET, it represents a promising sustainable option with properties superior to those of widely used compostable packaging polymers such as PLA.

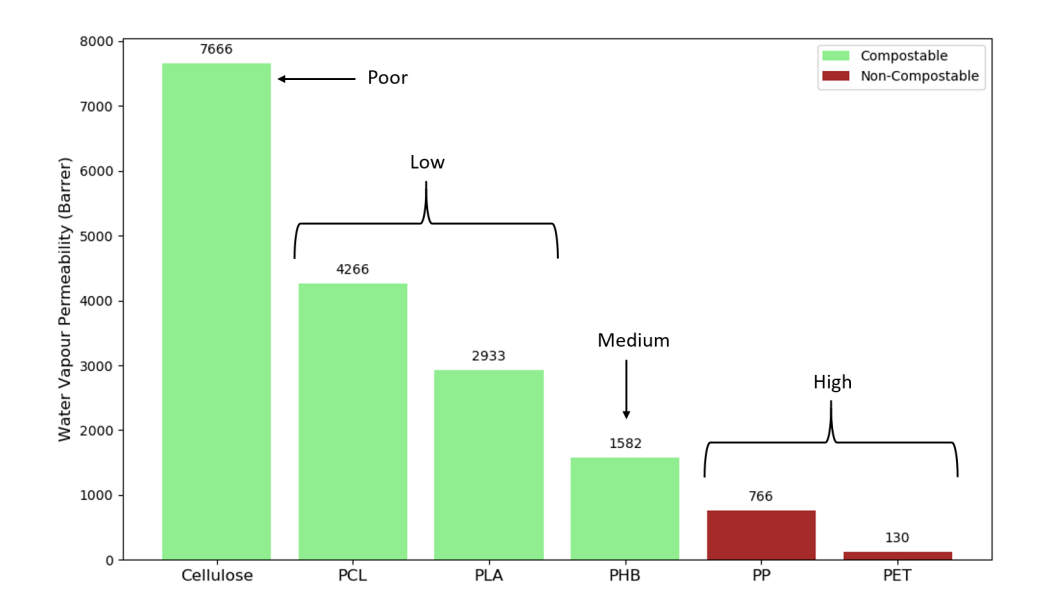


Figure 1.7: Comparison of water permeability of several packaging polymers. Where provided by the authors, the test conditions are as follows: cellulose 85% relative humidity (RH) [5], PCL 50% RH and 303 K [6], PLA 50% RH and 303 K [6], PHB [7], PP 300 K and 21% RH [8] and PET 298 K [9].

PHB has a melting temperature $(T_{\rm m})$ of ~ 448 K, which makes it compatible with conventional polymer processing techniques such as extrusion and injection moulding. It can be processed using standard industrial equipment without the need for specialised machinery. However, the thermal decomposition temperature of PHB is relatively close, at around 493 K [48], resulting in a narrow processing

Grade	Water Vapour Permeability	
	g $\mu {\rm m} \ {\rm m}^{-2} \ {\rm d}^{-1} \ {\rm kPa}^{-1}$	Barrer
Poor	>3000	>5757
Low	1000-3000	1919-5757
Medium	400-1000	768-1919
High	40-400	77-768
Very high	<40	<77

Table 1.1: Classification of packaging polymers films based on recommendations from Wang et al. [4].

window. As such, precise temperature control is essential during melt processing to avoid thermal degradation and material breakdown [39]. The $T_{\rm g}$ of PHB also poses challenges for certain applications. With a $T_{\rm g}$ of approximately 277 K [49], the polymer transitions into a rigid, glassy state below this temperature. In the context of food packaging, this means that when stored in refrigerated or frozen conditions, PHB is likely to lose its flexibility, becoming more brittle and susceptible to cracking or mechanical failure.

In terms of mechanical properties, PHB is, in some respects, comparable to conventional thermoplastics such as polypropylene. It has a relatively high Young's modulus (2–4 GPa) [50, 51] and tensile strength (30–40 MPa) [50, 52], indicating good stiffness and strength. However, PHB is also known for its brittleness, due to its high crystallinity and limited chain mobility. It typically shows low elongation at break (often less than 5%) [53, 54], which results in poor flexibility and impact resistance. These limitations can hinder its use in applications requiring ductile behaviour or resistance to mechanical stress.

1.4 Improving PHB Properties

Several of the limitations previously discussed in relation to pure PHB, such as brittleness, thermal instability and a narrow processing window, can be addressed through material modification strategies. The properties of PHB can be tailored to suit specific packaging applications using a variety of approaches, including blending with other polymers, copolymerisation and the incorporation of functional additives. The use of additives offers an effective means of modifying the thermal, mechanical and barrier behaviour of PHB. Additives can also enhance processability, helping to overcome some of PHB's inherent challenges in melt processing. For food packaging applications, it is essential that any additives used are non-toxic, approved for food contact and exhibit minimal migration to

ensure consumer safety and preserve material integrity. Furthermore, in the context of sustainable packaging design, additives should be environmentally benign, avoiding substances that persist in the environment or compromise recyclability or compostability.

1.4.1 Copolymerisation

PHB can be copolymerised with hydroxyvalerate (HV) monomers- that is, chemically combined with a second type of monomer during polymerisation- to produce the random isotactic copolymer, poly(hydroxybutyrate-co-hydroxyvalerate) (PHVB). In this structure, the HV and hydroxybutyrate (HB) units are randomly distributed along the polymer chain, while the stereochemistry remains isotactic, meaning the side groups are oriented in the same direction, as shown in Figure 1.8. This stereoregularity promotes semi-crystalline order in the copolymer.

Figure 1.8: Chemical structure of isotactic PHVB copolymer, where \mathbf{R} represents randomly ordered methyl and ethyl groups and the square brackets denote individual monomers.

PHVB has been widely studied due to its enhanced properties compared to pure PHB, particularly in terms of thermal stability, flexibility and processability. DSC, Orts et al. reported a decrease in the $T_{\rm m}$ of PHVB of up to 340 K as HV content was increased from 0 to 27 mol% [55]. However, X-ray diffraction and inverse gas chromatography measurements showed no significant change in the degree of crystallinity (X_c) , which remained around 60%. This was attributed to the co-crystallisation of the HB and HV units, which introduces defects into the crystal lattice. These defects lower the energy required to disrupt the lattice structure, thereby reducing $T_{\rm m}$ without significantly affecting X_c . A lower melting point is advantageous for processing, as it widens the thermal processing window and reduces the risk of thermal degradation during melt processing. In a separate study, Majerczak et al. observed a decrease in the $T_{\rm g}$ from 4°C to -1°C as the HV content increased from 0 to 21 mol% [49]. This shift was attributed to internal plasticisation, as the larger side groups of the HV units increase free volume and molecular mobility. A lower T_g allows the copolymer to remain flexible at lower temperatures, which is beneficial for applications requiring improved ductility and toughness.

Beyond thermal performance, copolymerisation with HV can also improve the barrier properties of PHB. Follain et al. found that PHVB with 3 mol% HV exhibited lower diffusion coefficients for water, oxygen, nitrogen and carbon dioxide compared to neat PHB [18]. Interestingly, the PHVB films in their study showed higher X_c than the PHB films. This increase in X_c was used to explain the enhanced barrier properties, as a denser crystalline structure limits the mobility of permeant molecules through the polymer matrix.

1.4.2 Plasticiser Addition

Plasticisers are additives used to enhance the flexibility, softness and processability of polymers by reducing intermolecular forces and increasing the free volume within the polymer matrix [56]. By interfering with polymer chain interactions, plasticisers allow the chains to move more freely, which imparts greater elasticity and reduces brittleness. They are particularly effective in amorphous or semi-crystalline polymers, where their incorporation leads to a significant reduction in the $T_{\rm g}$.

In addition to lowering $T_{\rm g}$, plasticisers can also reduce the $T_{\rm m}$ of a polymer, which facilitates processing at lower temperatures and can improve compatibility with other materials in blends or multilayer systems. The selection of an appropriate plasticiser depends on several factors, including its compatibility with the polymer, volatility, migration behaviour and toxicity, which is especially important in food-contact applications. Plasticisers may be of petrochemical origin (e.g. phthalates, which are now largely avoided due to health concerns) or derived from bio-based sources such as citrate esters, poly(ethylene glycol) or vegetable oils. The key factors which can determine a plasticiser's effectiveness in improving polymer properties are molecular weight, polarity, concentration used and type of functional groups present [39].

PHB is known for its high crystallinity and intrinsic brittleness, which limits its flexibility and impact resistance. The addition of suitable plasticisers can not only enhance the mechanical performance of PHB by improving its ductility but also lower its melting point, helping to reduce thermal degradation during processing. For these reasons, the use of plasticisers has been widely explored as a strategy to expand the applicability of PHB in flexible packaging formats. A study by Jost et al. looked at the effect of plasticisers on mechanical, thermal and barrier properties of PHVB films [39]. The plasticisers tested had a range of molecular weights and functional groups. It was found that medium weight plasticisers containing ether or ketone groups made for effective plasticisers in PHVB, due to interactions of the polymer with the oxygen in the functional groups. Glyceride plasticisers containing long fatty acid groups were deemed ineffective plasticisers for PHVB,

due to the long chains hindering interactions with the polymer. All plasticisers tested led to an increase in both water and oxygen permeability, with the general trend of increasing water and oxygen permeability with higher concentrations of plasticiser used. An improvement in mechanical properties, through the increase in elongation at break, was found for all tested plasticisers. Triethyl citrate (TEC) had the most notable effect, with an elongation at break of 2.3% vs 0.8% for pure PHVB.

Choi and Park also found TEC to be a highly effective PHB plasticiser, with elongation at break nearly doubling on TEC addition [57]. Break strength was reduced from 45 MPa for neat PHVB to 10 MPa when TEC was added and the tensile modulus fell from 245 to 98 MPa. Incorporation of TEC also saw a significant decrease in $T_{\rm m}$ of 290 K and decrease in $T_{\rm g}$ of 296 K, indicating effective plasticisation. Triacetin (TA) and acetyl tributyl citrate (ATBC) as PHB plasticisers were studied by Majerczak and Liggat [49]. Both plasticisers led to a decrease in $T_{\rm m}$, $T_{\rm g}$ and $T_{\rm c}$, however TA was concluded to be the more effective plasticiser for PHB.

1.4.3 Filler Addition

Filler particles are solid additives incorporated into polymer matrices to modify and enhance a wide range of material properties. Among these, nucleating agents (nucleants) are a specific class of fillers that influence the crystallisation behaviour of semi-crystalline polymers by providing sites for heterogeneous nucleation [44]. This can accelerate the rate of crystallisation, reduce overall crystallisation time and lead to a finer, more uniform crystalline structure [3]. These microstructural changes can improve stiffness, dimensional stability and thermal resistance, while also making processing more efficient. In semi-crystalline polymers like PHB, nucleating fillers have been shown to reduce spherulite size and increase spherulite density [44, 58, 59], which can improve mechanical properties such as tensile strength and modulus, and reduce the inherent brittleness of the material. A wide range of fillers have been studied for use with PHB, including graphene [60, 61], clays [49, 58, 62], silica [63], cellulose [64, 65] and boron nitride (BN) [59, 66]. Additionally, certain filler types, such as graphene and cellulose nanocrystals, can influence barrier performance by increasing the tortuosity of diffusion pathways for gases or moisture [60, 64], which is particularly advantageous for food packaging applications.

The overall effect of fillers on the X_c in PHB, however, is not always straightforward. A review paper on the effect of fillers on PHB found that some fillers enhance crystallinity, but others may hinder polymer chain mobility or aggregate at higher concentrations, leading to less predictable outcomes [3]. The effective-

ness of a filler depends on its chemical compatibility with the matrix, surface properties, dispersion and the specific processing conditions used. Among the many fillers investigated, BN has shown particular promise [59]. BN acts as a highly effective nucleating agent in PHB, significantly reducing spherulite size and increasing the number of nucleation sites [3]. This results in a finer, more uniform spherulitic structure, which enhances toughness and reduces brittleness. Although its impact on overall crystallinity can vary slightly [59, 66], BN generally helps to maintain or modestly increase crystallinity while promoting a more favourable microstructure. These characteristics make BN a valuable additive for improving both the processability and end-use performance of PHB-based packaging materials.

1.5 Project Aims and Objectives

A notable literature gap lies in the use of molecular dynamics (MD) simulation to investigate barrier properties of PHA-based polymers. Although experimental studies have measured water and oxygen permeability in PHB films, there is limited insight into how individual permeant molecules interact with and diffuse through the polymer matrix, particularly in relation to microstructural features. MD simulations are uniquely suited to provide this level of detail, yet few studies have applied them to model gas or water transport in PHAs.

Experimentally, while the semi-crystalline nature of PHB has been widely reported, there remains no clear, mechanistic understanding of how its microstructure, such as spherulite size and degree of crystallinity, affects key physical properties, including barrier performance. The lack of integration between simulation and experiment also means that structure-property relationships in PHB are poorly defined, limiting opportunities for simulation-informed design of PHB-based films for packaging applications.

While experimental techniques are valuable for characterising polymer crystallinity and physical properties, MD simulations offer a complementary perspective by enabling detailed analysis of polymer behaviour at the nanoscale. Several MD studies have explored the structural and thermal properties of amorphous PHB. Kyles and Tonelli modelled the conformational characteristics of PHB, which were consistent with experimental observations in dilute solutions [67]. Glova et al. carried out atomistic simulations of blends of PLA and PHB and demonstrated that the two polymers are miscible, with their miscibility exhibiting scale dependence [12]. Their follow up study used MD simulations to investigate PHB and PLA composite systems, containing cellulose nanocrystal filler particles and they discovered that grafted PHB chains extend away from the

surface, whereas grafted PLA chains are able to fold back to the surface to form hairpin-like structures [65]. Papchenko *et al.* simulated the diffusion and sorption of gases CH₄ and CO₂ through a range of amorphous PHAs and obtained promising results for the solubility–selectivity of the two gases [68].

To date, there appear to be no published MD studies of crystalline PHB or PHV, despite their significance as semi-crystalline materials. Likewise, MD investigations of amorphous PHV and PHVB copolymers remain limited and unexplored. This project aims to address these knowledge gaps through a combination of MD simulations and experimental work. The central hypothesis is that microstructural features in PHB, including crystallinity, additive content and HV incorporation, play a key role in determining barrier properties. To investigate this, the project will pursue the following objectives:

- Create and validate a force field model for crystal and amorphous PHAs.
- Use MD simulations to understand gas diffusion in PHB and PHV.
- Use MD simulations to explore the effect of fillers on diffusion.
- Characterise the mechanical and barrier properties and the role of fillers and plasticisers in PHA films.

Chapter 2

Methodology

This chapter outlines the methodology used in both the molecular dynamics (MD) simulations and the experimental characterisation of polyhydroxybutyrate (PHB) films. The first part of the chapter provides an overview of MD simulations, including the theoretical foundations of the technique, the role of force fields and potential functions and the treatment of key simulation parameters such as periodic boundary conditions, thermodynamic ensembles and partial charge calculations. The models used for water and oxygen molecules are described, alongside the implementation of constraints, energy minimisation protocols and the use of thermostats and barostats. The detailed simulation methodology varies for each of the models studied. The specific procedure for modelling amorphous PHB and PHV, as well as the PHB and PHV unit cells can be found in Section 3.2 (Chapter 3). For further information on modelling larger crystalline PHB systems and PHB/graphene composite systems, see Section 4.2 (Chapter 4). The second part of the chapter describes the experimental methods employed to prepare and characterise PHB films. This includes film fabrication by solvent casting, verification of polymer composition and purity using nuclear magnetic resonance (NMR) and thermal analysis via differential scanning calorimetry (DSC). Structural and surface characterisation were conducted using scanning electron microscopy (SEM) and water contact angle measurements, respectively, while barrier and mechanical properties were assessed using water vapour permeation testing and texture analysis.

2.1 Molecular Dynamics

Classical MD is a computational technique used to model the physical movements of atoms and molecules over time. It provides a powerful means of studying the structure, dynamics and interactions of molecular systems at the atomic and molecular level. In a classical MD simulation, atoms are treated as particles whose trajectories evolve according to Newton's laws of motion. By numerically

integrating these equations, it is possible to predict how a molecular system responds to various physical conditions, providing insight into phenomena such as molecular diffusion, conformational changes and mechanical or thermal behaviour.

At the heart of an MD simulation are the equations of motion, which describe how the position and velocity of each atom changes over time under the influence of forces derived from the potential energy of the system. The fundamental relationship is Newton's second law:

$$F_i = m_i a_i = m_i \frac{d^2 r_i}{dt^2}$$

where F_i is the force acting on atom i, m_i is its mass and a_i is its acceleration, which is the second derivative of its position r_i with respect to time t [69]. The forces are typically obtained from empirical interatomic potentials that describe bonded and non-bonded interactions. Numerical integration algorithms are used to solve the equations of motion for all particles in the system. One of the most commonly used algorithms is Verlet, which computes new positions of particles but does not calculate their velocities. The Velocity-Verlet algorithm is an extension of Verlet, where particle velocities are computed. All simulations in this work used Velocity-Verlet. The integrations are performed at every timestep, which is defined by the user. For atomistic simulations, the integration algorithms require short timesteps, typically one or two femtoseconds (fs), to ensure the atoms don't move too far between timesteps. For course-grained simulations, longer timesteps can be used. At each timestep, new positions and velocities are computed for each particle, which can be saved to a trajectory file for post-processing. A timestep of 1 fs was used for all simulations in this work.

Constraint algorithms are used in MD to fix certain degrees of freedom, such as bond lengths or angles, to enable the use of longer integration time steps. These constraints are particularly useful for limiting the fastest vibrational motions in the system, which are often associated with light atoms such as hydrogen. By constraining these high-frequency motions, simulations can be run more efficiently without compromising overall accuracy. One commonly used constraint algorithm is SHAKE, which is designed to iteratively adjust atom positions during each time step to enforce fixed bond lengths or angles. SHAKE is typically used for bonds between hydrogen atoms and heavier atoms (e.g., C-H, O-H, N-H). By applying SHAKE to these bonds, the time step can be safely increased (e.g., to 1 or 2 fs), significantly improving computational efficiency while maintaining realistic molecular behaviour.

In MD, each atom is represented as a point particle with a defined position, velocity and mass. The atomic coordinates evolve with time and interactions be-

tween atoms are calculated based on these coordinates. Bonds between two atoms can stretch and contract and the angles between three atoms can bend, corresponding to bond and angle potentials. For four atoms bonded linearly, twisting around the central bond is subject to a dihedral torsion potential. If three atoms are bonded to a central fourth atom, a similar improper dihedral potential is applied. Non-bonded interactions include van der Waals (vdW) interactions, which are typically modelled using potential functions such as the Lennard-Jones (LJ) pair potential, and electrostatic interactions.

Several software packages are available for performing MD simulations, including GROMACS, AMBER, NAMD and LAMMPS. Each has particular strengths depending on the system being studied and the type of analysis required. For this study, the open-source software LAMMPS (Large-scale Atomic/Molecular Massively Parallel Simulator), version lammps/intel-2020.4/23Jun2022 [70] was used due to its flexibility and strong support for modelling both polymers and solids, allowing the simulation of polymer composites. LAMMPS is particularly well-suited to simulating large, heterogeneous systems and provides robust tools for customising force fields, imposing periodic boundary conditions and modelling both bonded (e.g. bonds, angles, dihedrals) and non-bonded interactions efficiently. LAMMPS also offers good scalability on high-performance computing clusters, allowing simulations of polymer systems over long timescales and large spatial domains. Its support for coarse-grained models, user-defined potentials and a wide range of thermostats and barostats make it an ideal choice for simulating the dynamic behaviour and thermophysical properties of polymers and their interaction with small molecules such as water and oxygen. For the analysis of simulation trajectories, Python scripts were used, making use of the open-source MDAnalysis library [71]. Simulation trajectories were visualised using VMD [72].

2.1.1 Force Field Models

A force field describes the intra- and inter-molecular energy potentials of atoms in a simulation. Force field parameters are derived from both quantum mechanical calculations and experiments and they allow the potential energy of atoms in a simulated system to be calculated and hence the system properties. Selecting an appropriate force field is an important step in setting up an MD simulation. Much research has gone into the development of transferable force fields so there is a wide variety to choose from to describe a particular system. Some of the most commonly used force fields include AMBER, OPLS, GROMOS and CHARMM. Different force fields use different classifications for grouping together atom types, as well as different parameters for each type of atom, bond, angle etc. The chosen force field will define the exact equation used to calculate all potentials, including all the force constants to be used. The bonded interactions which the force field

must describe include bond stretching, angle bending and dihedral (torsional) angles. These are shown in an example molecule in Figure 2.1.

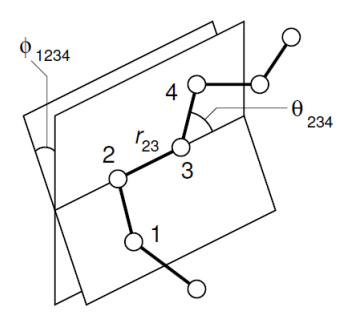


Figure 2.1: Chain molecule showing bond length r_{23} , bond angle θ_{234} and dihedral torsional angle ϕ_{1234} [10].

Non-bonded interactions include vdW and electrostatic interactions. Despite being represented as points, atoms are associated with an effective size through a vdW radius, σ , which influences how closely atoms can approach one another. The LJ potential is used to compute the short-range dispersion forces between two particles. σ and the potential energy well-depth, ε , are assigned to each atom type and these parameters are used to compute the vdW forces. Since vdW interactions are only significant at short interatomic distances, a cut-off is used to smooth the LJ potential to zero at a specified distance. By not having to calculate intermolecular interactions of atoms greater than the cut-off distance apart, computational requirements are significantly reduced.

In order to include electrostatic interactions in a simulation, partial charges for each atom must be assigned. Some atoms will be positively charged and some negatively charged, but the sum of all charges should be zero to simulate a neutral system. A Coulomb potential is used to compute the electrostatic interactions between two particles, where the proximity of the particles and the product of their charges defines the electrostatic energy. As with vdW interactions, a cut-off is also used to switch the potential at a given separation distance. For all simulations in this work, a cut-off of 10 Å was used for both the vdW and short-range electrostatic potentials. This cut-off distance provides a good compromise between accuracy and computational cost. vdW interactions decay rapidly and are negligible beyond this distance. However, the electrostatic potential decays to zero slower than LJ so after the cut-off distance, a long-range solver can be used to correct for this. In LAMMPS, the long range electrostatic interactions are computed using the PPPM method (particle-particle/particle-mesh) [73].

Some force fields come with pre-assigned partial charges for specific atom types in commonly used molecular fragments. Often, however, the force field used may require the prior determination of partial charges using quantum mechanical methods. While these partial charges still depend on the atom type, they are not transferable directly between two different atoms of the same type. The chemical environment of an atom, i.e. the types of atoms surrounding it, will influence the charge associated with it.

2.1.2 Force Fields Used in This Work.

GAFF

The General Amber Force Field (GAFF) [74] was selected for modelling polymers in the current work because of its broad applicability and proven reliability across a wide range of organic systems. GAFF is parameterised to cover the functional groups present in PHB, including ester linkages, aliphatic backbones and carbonyl moieties, making it particularly suitable for simulating aliphatic polyesters without requiring extensive reparameterisation. As an extension of the AMBER (Assisted Model Building and Energy Refinement) force field [75], originally designed for biomacromolecules, GAFF inherits the ability to handle large molecular systems, making it well-suited for long-chain polymers containing thousands of atoms. Its versatility has also made it one of the most widely adopted force fields for polymer and biomaterial simulations, including heterogeneous systems such as polymer/filler composites [12, 76, 77, 78, 79]. Importantly, previous MD studies by Glova et al. successfully used GAFF to model amorphous PHB and reproduced experimental properties [12, 65]. Consistent with these reports, the structural and thermal properties of PHB obtained in the present work agreed well with values in the literature (see Chapter 3), further supporting the suitability of GAFF for this system. While alternative force fields could also be considered, benchmarking multiple force fields is highly time-consuming and was beyond the scope of the current study.

GAFF uses 57 atom types, made up of 35 'basic' atoms and 22 'special' atoms, based on their chemical environment. For example, 'hn' is a hydrogen atom that's bonded to a nitrogen atom and 'ca' is a carbon atom in an aromatic system. Of these 57 atom types in GAFF, only 8 of them are required to construct a PHB molecule. These atom types are described in Table 2.1 and shown schematically for a PHB molecule in Figure 2.2.

Once atoms have been defined, bonds, angles, dihedrals and impropers must all be included in the LAMMPS input file. The force field used will define the styles of interaction potentials for bonded and non-bonded interactions. GAFF uses a harmonic potential for bond stretching and angle bending, given by the

Atom Type	Description
С	sp^2 C in carboxyl groups
c3	sp^3 C
О	O in carboxyl groups
oh	O in hydroxyl groups
os	O in ester groups
hc	H on aliphatic C
ho	H in hydroxyl groups
h1	H on aliphatic C with 1 electron withdrawing group

Table 2.1: GAFF atom types used for building a model of PHB.

Figure 2.2: Atom types used to represent a PHB molecule.

following equations:

$$E_{bond} = K_r(r - r_0)^2$$
 $E_{angle} = K_{\theta}(\theta - \theta_0)^2$

Where K_r and K_{θ} are the bond and angle force constants, r_0 and θ_0 are the equilibrium bond length and equilibrium bond angle and r and θ are the bond length and bond angle, respectively. In GAFF, the Fourier potential is used for dihedral torsion:

$$\sum_{i=1}^{m} E_{dihedral} = K_{\phi,i} [1 + \cos(n_i \phi - \gamma_i)]$$

Where m is an integer ≥ 1 , $K_{\phi,i}$ is the dihedral force constant, ϕ is the dihedral angle, n_i is the periodicity of torsion (integer) and γ_i is the phase angle. For improper dihedrals, the consistent valence force field (CVFF) style is used in GAFF. The potential is given by:

$$E_{improper} = K_{\beta}[1 + d \cos(n\beta)]$$

Where K_{β} is the improper force constant, β is the improper angle, n is the periodicity of torsion (integer) and $d = cos(\gamma)$ (d = +1 or -1), where γ is the phase angle.

For non-bonded atoms, the Coulomb potential is used to compute electrostatic interactions:

$$E_{Coul} = \frac{Cq_iq_j}{\epsilon r_{ij}}$$

Where q_i is the partial charge on the ith atom, i and j are the two interacting atoms, C is an energy-conversion constant, ϵ is the dielectric constant and r_{ij} is the distance between atoms i and j. For assigning partial atomic charges compatible with GAFF, quantum mechanical calculations were performed using the Gaussian software package [80]. The molecular electrostatic potential (ESP) was calculated at the Hartree-Fock level of theory with the 6-31G* basis set (HF/6-31G*), as recommended for use with GAFF. The resulting Gaussian output file was then processed using Antechamber, a tool within the AmberTools suite [81], to perform a restrained electrostatic potential (RESP) fitting. In this step, Antechamber extracted the ESP data from the quantum mechanical calculation and applied the RESP method to derive partial charges for each atom, while applying restraints to prevent overfitting and to ensure chemically reasonable values.

Finally, the LJ potential is used to describe the non-bonded dispersion forces between two atoms. This is given by:

$$E_{LJ} = 4\varepsilon_{ij} \left[\left(\frac{\sigma_{ij}}{r_{ij}} \right)^{12} - \left(\frac{\sigma_{ij}}{r_{ij}} \right)^{6} \right]$$

Where r_{ij} is the interatomic distance, σ_{ij} is the effective vdW radius and ε_{ij} is the minimum energy between atoms i and j. To obtain the LJ parameters σ_{ij} and ε_{ij} , the Lorentz-Berthelot mixing rules are applied for each atom pair as follows:

$$\sigma_{ij} = \frac{1}{2}(\sigma_i + \sigma_j)$$
 $\varepsilon_{ij} = \sqrt{(\varepsilon_i \varepsilon_j)}$

When simulating the polymer chains, the SHAKE algorithm was used to fix the bond lengths and angles of the H atoms to their equilibrium values. This is common practice when simulating large organic molecules.

While non-bonded interactions are still experienced between two atoms in the same molecule, the values of these interactions are usually either zeroed or scaled down for atoms which are separated by two or three bonds. These are referred to as 1-4 interactions and in LAMMPS the scaling can be set via the *special_bonds* command. For AMBER-type force fields, including GAFF, the interactions between atoms which are two bonds apart are set to zero. For atoms three bonds apart, the LJ component is scaled by $\frac{1}{2}$ and the Coulombic component is scaled by $\frac{5}{6}$.

Water and Oxygen Force Field Models

In MD simulations, water models are simplified representations used to mimic the behaviour of water molecules, capturing their structural and thermodynamic properties while remaining computationally efficient. Since water plays a central role in many biological and materials systems, selecting an appropriate water model is crucial to ensure accurate results. These models typically consist of rigid or flexible arrangements of point charges and LJ interaction sites, designed to reproduce key physical properties such as density, diffusion coefficient, dielectric constant and hydrogen bonding behaviour. Among the many available models, such as TIP3P, TIP4P and SPC, the SPC/E (Extended Simple Point Charge) model is widely used due to its favourable balance between accuracy and computational cost. This model was chosen for simulating diffusion of water molecules. SPC/E represents each water molecule with three interaction sites and includes a LJ potential on the oxygen atom [21]. A schematic of the SPC/E model is shown in Figure 2.3. Compared to simpler models like SPC or TIP3P, SPC/E provides better agreement with experimental data for properties such as liquid density, radial distribution functions and self-diffusion coefficients, making it a robust choice for simulating water transport and interactions in polymer systems [20]. Additionally, this water model has been shown in the literature to be compatible with GAFF [82, 83, 84]. The SHAKE algorithm was used to constrain the bond lengths and angles to their equilibrium values, as is required when using the SPC/E model.

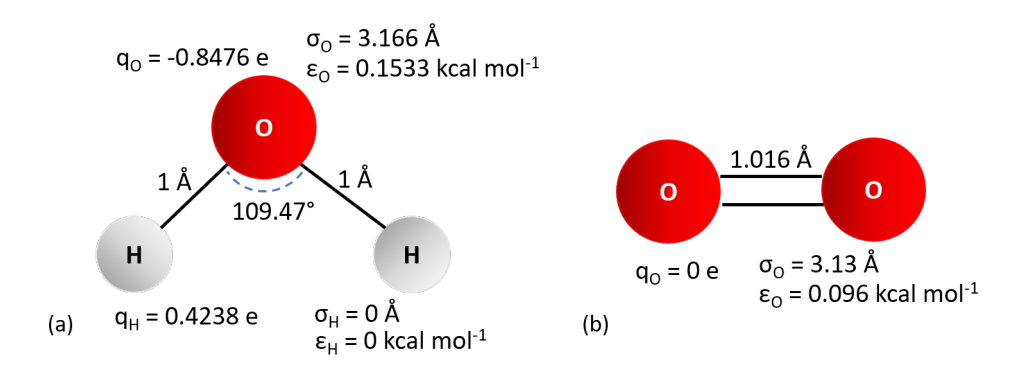


Figure 2.3: (a) Water model and (b) oxygen model used in the current work.

Similarly, when simulating oxygen molecules, it is crucial to select a model

that can accurately reproduce the key physical properties of molecular oxygen. Javanainen et al. reviewed the performance of 14 oxygen models, including those from the TraPPE and CHARMM families, and subsequently developed three new models; two with partial charges and one without [22]. They assessed the models based on their ability to reproduce experimental density, free energy of hydration, enthalpy of vaporisation and solvation free energy. The three new models demonstrated significant improvements over earlier models in capturing these thermodynamic properties and were in good agreement with experimental data. In particular, Javanainen's models, which are designed to be compatible with widely used water models like SPC/E, accurately reproduced experimental oxygen-oxygen radial distribution functions, solubility in water and diffusion coefficients. Furthermore, it was successfully used by Lightfoot et al. to model diffusion of oxygen through polyethylene terephthalate and polyethylene furanoate [85]. This model was adopted in the current study to investigate oxygen diffusion through polymer matrices. Specifically, the version of the model without partial charges was chosen here, as it exhibited the smallest deviations from experimental values and thus should provide the most reliable results for oxygen transport behaviour. SHAKE was used to constrain the O=O bond to its equilibrium value, as this particular model was developed with a constraint rather than a defined bond force constant.

2.1.3 Periodic Boundary Conditions

Since MD simulations typically use a relatively small number of atoms compared to experimental systems, periodic boundary conditions should be used to avoid finite size effects. In this way, the simulation box is replicated in some or all dimensions, creating an infinite lattice. During the simulation, each atom has a periodic image in the neighbouring boxes which moves in an identical way to the original atom, shown diagrammatically in Figure 2.4. When an atom moves across a box boundary, it reappears on the opposite face boundary. In this way, the total number of atoms in the simulation box is conserved.

All simulations carried out in the current work had periodic boundary conditions applied in all three Cartesian directions.

2.1.4 Ensembles

Statistical mechanics allows for the conversion of microscopic level information (such as atom coordinates and velocities) to macroscopic detail (such as temperature and pressure). The concept of an ensemble refers to a statistical collection of systems, each representing a possible state that the system can adopt under specified thermodynamic conditions. The choice of ensemble determines which thermodynamic variables are held constant and which are allowed to fluctuate,

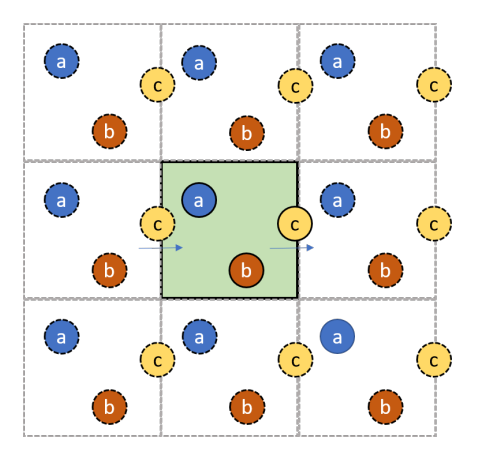


Figure 2.4: Diagrammatic representation of periodic boundary conditions. Solid outlines show the simulation box and particles, dashed lines represent the replicated images of the system.

thereby influencing the statistical properties sampled during the simulation. The most commonly used ensembles in MD are the microcanonical (NVE), canonical (NVT) and isothermal-isobaric (NPT) ensembles. The NVE ensemble maintains constant number of particles (N), volume (V) and energy (E), and is often used for studying energy conservation in isolated systems. Often in simulations it is desirable to control the temperature of the system. The NVT ensemble keeps the number of particles, volume and temperature (T) constant by employing thermostats to regulate temperature. The NPT ensemble, which maintains constant pressure (P) in addition to temperature, is particularly useful for simulating systems under experimentally relevant conditions, such as biological environments or materials under ambient pressure. The selection of an appropriate ensemble depends on the specific goals of the simulation and the physical conditions one wishes to replicate.

In the current work, the NVT ensemble was used when the box size was to be fixed and the NPT ensemble was used when changes in density were of interest.

2.1.5 Thermostats and Barostats

In MD simulations, thermostats and barostats are essential algorithms used to regulate the system's temperature and pressure, respectively. In real-world experimental conditions, materials exchange energy with their surroundings to maintain constant thermodynamic conditions. To reproduce such environments computationally, thermostats and barostats are employed to ensure the system samples the appropriate statistical ensemble, such as the NVT or NPT ensemble. Thermostats work by adjusting atomic velocities to maintain a target temperature,

while barostats modify the simulation box volume to control pressure. A variety of thermostat algorithms exist, including Berendsen, Andersen, Langevin, velocity rescale and Nosé-Hoover, each with different trade-offs in accuracy and computational cost. Likewise, barostat options include the Berendsen, Parrinello-Rahman and Nosé-Hoover methods. Among these, the Nosé-Hoover thermostat and barostat are widely used due to their ability to accurately reproduce the desired thermodynamic ensembles through extended equations of motion. These methods introduce fictitious degrees of freedom that act as thermal or pressure reservoirs, enabling energy exchange while preserving the system's physical dynamics.

In this study, the Nosé-Hoover thermostat and barostat [86] were used to maintain the target temperature and pressure throughout the simulations. Compared to simpler methods such as the Berendsen thermostat, which applies exponential damping to enforce temperature control, the Nosé-Hoover method allows for natural fluctuations of temperature and pressure around the desired setpoints. This leads to more accurate sampling of the NVT and NPT ensembles [87]. These features make the Nosé-Hoover approach particularly suitable for polymer simulations, where it is important to preserve realistic dynamical behaviour for accurate analysis of properties like diffusion, chain mobility and structural relaxation. In LAMMPS, Nosé-Hoover thermostat and barostat are implemented using ensemble-specific fix commands such as fix nvt or fix npt. The user specifies parameters including the initial and final temperatures $(T_{\text{start}}, T_{\text{stop}})$ and the thermostat damping constant $(T_{\rm damp})$, which controls how quickly the system relaxes to the target temperature. When a constant temperature is required, $T_{\rm start} = T_{\rm stop}$. Similarly, the Nosé-Hoover barostat uses parameters $P_{\rm start}$, $P_{\rm stop}$ and P_{damp} . Pressure coupling can be applied isotropically, where the x, y, and z box dimensions scale together, or anisotropically, where each direction is scaled independently.

In the current study, isotropic pressure control was used when simulating amorphous PHAs in a cubic simulation box, to maintain equal dimensions in all directions. In contrast, for simulations of PHA crystals, anisotropic pressure control was applied to allow the lattice parameters to adjust independently, better reflecting the anisotropic nature of the crystalline unit cells.

2.1.6 Energy Minimisation

Energy minimisation is a preparatory step in simulations used to remove steric clashes or unfavourable geometries from an initial molecular structure. It involves iteratively adjusting atomic positions to find a local minimum on the potential energy surface, where the net forces acting on atoms are reduced to near zero.

Commonly used algorithms for energy minimisation include conjugate gradient [88] and steepest descent [89]. Unlike MD, which simulates motion over time, energy minimisation is a static process that seeks a more stable configuration by descending along the potential energy gradient. This step is particularly important when a system has been built or modified manually, such as after combining molecular components, inserting molecules into a simulation box or generating initial structures through modelling. Performing energy minimisation helps prevent large, unphysical forces that could destabilise the simulation when MD steps begin, thereby improving the reliability and stability of subsequent equilibration and production runs. The steepest descents algorithm was used to minimise the energy of the polymer systems in the current work, prior to any MD steps being run. This algorithm has previously been used for simulating PHB molecules [12, 65]. In the case of randomly inserted polymer chains, this energy minimisation was a necessary step to prevent the system blowing up due to overlapping atoms.

2.2 Experimental

The following sections describe the methods used for the experimental part of this project. Results can be found in Chapter 5.

2.2.1 Film Preparation

There are various methods for producing PHA films, each offering advantages depending on the intended application and the physical properties required. The film preparation process directly influences the final film's microstructure, thickness and mechanical properties, which in turn impact many other properties. In this study, obtaining thin, uniform films was critical for accurate water vapour transmission rate (WVTR) measurements and for capturing clear spherulitic structures under SEM. Therefore, careful selection of the preparation method was crucial to ensure that the films met these experimental requirements and reflected the properties of the bulk polymer.

Extrusion is a common method, particularly in industrial-scale processing. In this technique, the molten polymer is forced through a channel to form a thin sheet or film, which is then cooled and solidified. Melt pressing is another widely used technique that involves applying high pressure to PHA powder at a temperature above its melting point. This process results in dense, uniform films and is suitable for applications where mechanical strength and dimensional stability are prioritised. After film formation, the cooling step significantly affects the polymer microstructure. The film can be allowed to cool slowly at room temperature, promoting gradual crystallisation and the growth of larger, well-defined spherulites.

Alternatively, it can be quenched rapidly, such as by immersion in liquid nitrogen, to suppress crystallisation and produce an amorphous or less crystalline structure. This rapid cooling 'freezes in' the molecular arrangement at the point of quenching. Initial testing of the film characterisation techniques used previously-prepared melt-pressed PHB films. Attempts using these samples found that they were too thick to allow clear spherulite imaging under SEM and their brittleness caused difficulties in sample preparation for WVTR measurements. As a result, it was decided that solvent casting would be used to prepare the PHB films for the current study.

Solvent casting is particularly well-suited for laboratory-scale film preparation. It involves dissolving the polymer powder in an appropriate solvent, spreading the solution into a thin layer using a casting blade and allowing the solvent to evaporate. As the solvent leaves the system, a uniform polymer film is left behind. Solvent casting allows for excellent control over film thickness and composition, and it is compatible with the incorporation of additives or fillers during the dissolution stage.

As mentioned, solvent casting enabled the ability to generate films that were thin enough to enable both microscopy imaging of spherulites and measurements of WVTR. In contrast to the melt-pressed samples, the solvent-cast films were thin, flexible and easy to handle, cut and test without breaking. Additionally, they were optically transparent and relatively quick to produce, making them suitable for high-throughput testing. One of the films produced is shown in Figure 2.5.



Figure 2.5: PHB film produced from solvent casting.

Although solvent casting may not directly mirror the large-scale industrial processing of PHB, such as extrusion or melt pressing, the films obtained nevertheless provide a meaningful model system for investigating structure-property relationships. In particular, the spherulitic morphologies observed in solvent-cast PHB films are comparable to those reported in melt-pressed and extruded samples,

where crystallisation from the melt also results in lamellar spherulites of similar organisation [58]. This structural similarity enhances the translatability of the experimental data to the MD simulations, which model the influence of additive incorporation, and crystalline and amorphous domains on barrier performance.

The presence of solvent may influence the properties of polymer films by affecting chain organisation during the casting and drying process [90]. Solvents with slower evaporation rates can allow more time for molecular rearrangement, which may alter crystal growth rate and morphology [91], compared to those which evaporate faster. Furthermore, residual solvent can act as a temporary plasticiser until completely evaporated from the film. Solvent selection and drying conditions are therefore not only practical considerations but also factors which could potentially influence the properties of PHB films. The solvent of choice in this study was chloroform, which is widely used for dissolving PHAs due to its high solubility capacity for these polymers. Selecting an appropriate solvent is essential to ensure complete dissolution of PHB powder, uniform film formation and reproducibility. PHB is notoriously insoluble in most common, non-chlorinated solvents (e.g., ethanol, acetone, DMSO, THF), particularly at room temperature, whereas it dissolves effectively in halogenated solvents such as chloroform [92]. The superior dissolving power of chloroform arises from its polarisable chlorine atom, which interacts favourably with the carbonyl groups of the PHB polymer chain, allowing efficient dissolution even of the homopolymer, which is more difficult to solvate than PHVB copolymers [13, 92]. Many PHB-based film studies therefore employ chloroform, making this approach well-established in the field [18, 64, 93, 94, 95, 96]. While chloroform is classified as a toxic and hazardous solvent, it remains a practical choice in small-scale laboratory work, not only because of its dissolving power but also because of its low boiling point (334 K), which facilitates rapid evaporation and shortens drying times. This rapid evaporation also minimises the risk of phase separation or filler sedimentation during casting, thereby ensuring uniform film composition.

To make the polymer solution, PHB powder (Helian Polymers, PB3000) was first washed in ethanol to remove impurities and dried at room temperature in a desiccator containing silica gel. A sample of the purified PHB powder was analysed using nuclear magnetic resonance (NMR) (details below). The PHB powder was then dissolved in chloroform at a concentration of 10% weight/volume (i.e. 1g of PHB per 10 mL of chloroform) in a glass jar. For the films with additives, the BN (Sigma-Aldrich, 255,475, 98%, powder, ca. 0.6 μm) and/or TA (Sigma-Aldrich, W200700, 99%, liquid) were added at this stage and the mixture was stirred to disperse the powders in solution. Details on the formulations are given in Table 2.2.

PHB	Pure PHB
PHB_TA	PHB + 10 wt% TA
PHB_TA/1BN	PHB + 10 wt% TA + 1 wt% BN
PHB_1BN	PHB + 1 wt% BN
PHB_0.25BN	PHB + 0.25 wt% BN
PHB_0.06BN	PHB + 0.0625 wt% BN

Table 2.2: Formulations used for PHB films.

The glass jars were secured with a lid and a rubber seal to prevent chloroform evaporating during heating. The mixtures were then heated in an oven at 333 K for approximately one hour until the PHB powder had visibly dissolved, resulting in a viscous solution. To ensure even distribution of the dissolved polymer and additives, the solution was stirred again for 30 minutes using a magnetic stirrer bead before being left to cool to room temperature.

To cast the films, 10 mL of polymer solution was poured into the opening of the casting blade, which then moved across a glass support to create an even coating of PHB solution. Once cast, the films were left in a fume cupboard for at least four hours to allow safe and complete evaporation of the chloroform, leaving behind the solid polymer films. In order to remove the film from the glass support without damaging it, it was necessary to place the support in a basin of water briefly. This caused the PHB film to peel away easily from the glass and, due to the hydrophobic nature of PHB, the films could be quickly blotted dry with paper towel. Before characterisation, the films were further stored under vacuum for 12 hours to ensure removal of any residual solvent. A thermal post-treatment step was not performed, as it was considered unnecessary for the intended analyses. While some studies have reported applying thermal annealing to alter crystallinity or remove residual solvent [64, 97], others have demonstrated that simple room temperature or vacuum drying is sufficient to produce stable PHB films for characterisation [18, 95, 96]. Given this precedent in the literature, and since the focus of this work was on films cast and dried under mild conditions, no additional thermal treatment was applied. A micrometer was used to determine the thickness of the films, averaging over ten measurements taken across the film. The average thickness of the films was $20 \pm 3 \mu m$.

2.2.2 Characterisation Techniques

The following subsections describe the experimental techniques used to investigate PHB film properties.

Nuclear Magnetic Resonance Measurements

For polymer analysis, Nuclear Magnetic Resonance (NMR) is particularly useful for confirming monomer composition, detecting impurities and identifying copolymer ratios. In the case of PHAs, NMR can distinguish between different types of monomers incorporated into the polymer chain. This is important because the fermentation conditions and feedstock used during biosynthesis can result in various copolymers, such as PHVB, rather than the homopolymer PHB. NMR spectroscopy is a powerful analytical technique used to elucidate the chemical structure of organic compounds by detecting the magnetic environments of atomic nuclei, most commonly hydrogen (¹H) and carbon (¹³C). The method relies on the principle that certain nuclei possess a magnetic moment and will align with or against an external magnetic field. When subjected to radiofrequency radiation, these nuclei can absorb energy and transition between energy levels. The resulting signal, known as a chemical shift, is sensitive to the electronic environment surrounding each nucleus, allowing for identification of functional groups and molecular structure.

In this study, ¹H NMR spectroscopy was employed to analyse PHB powder following purification in ethanol. The NMR spectra served three purposes: (1) to confirm the absence of residual impurities or contaminants in the polymer, (2) to verify that ethanol from the purification process had been fully removed and (3) to confirm that only 3-hydroxybutyrate (HB) units were present, indicating that the polymer was a PHB homopolymer rather than a PHVB copolymer.

For sample preparation, PHB powder was dissolved in deuterated chloroform at a concentration of 1 wt%. The resulting solution was transferred into an NMR tube and analysed using a Bruker AV3 HD 500 spectrometer. The scan was conducted at 298 K with a frequency of 400 MHz. Spectra were processed using Topspin (version 4.4.1), and the chemical shifts were compared with reference data for PHB and polyhydroxyvalerate (PHV) reported in the literature.

Differential Scanning Calorimetry

Differential Scanning Calorimetry (DSC) is a widely used thermal analysis technique for characterising the crystallinity and thermal behaviour of polymers. In particular, it provides quantitative information on melting and crystallisation temperatures, enthalpies and degrees of crystallinity, making it an essential tool for assessing how additives or processing conditions influence the crystalline content and thermal stability of polymer films.

DSC works by measuring the difference in heat flow between a sample and an inert reference (typically an empty sample pan) as a function of temperature or time, under a controlled heating or cooling program. As a relative technique, DSC does not directly measure the absolute heat flow into the sample; rather, it detects the difference in the amount of heat required to increase the temperature of sample and the reference. This differential approach allows the identification of thermal transitions such as the glass transition temperature (T_g) , crystallisation temperature (T_c) and melting temperature (T_m) , which are key indicators of a polymer's microstructure and processability. The fundamental principle underlying DSC is the relation:

$$Q = C_p \Delta T \tag{2.1}$$

Where Q is the heat flow, C_p is the specific heat capacity of the sample and ΔT is the change in temperature experienced due to the heating or cooling program. A heat-cool-reheat (HCR) cycle is often used for polymer samples to obtain a first melting temperature (T_{m1}) , a crystallisation temperature (T_c) and a second melting temperature (T_{m2}) . The first heat reflects the polymers thermal history caused by its previous processing, e.g. quenching from a melt. After heating to the melt phase, the sample is cooled at a fixed rate allowing for recrystallisation from the melt. The second heating run then provides a clearer picture of the polymer's intrinsic thermal properties, as the effects of prior processing are removed. As such, T_{m1} may differ from T_{m2} due to changes in crystallinity or crystal perfection upon controlled crystallisation. A DSC spectra from a HCR cycle will contain three peaks (one per temperature ramp) each of which can be integrated to obtain the enthalpy change associated with the melting/crystallisation process. Degree of crystallinity (X_c) of the polymer sample can be calculated by:

$$X_c = \frac{\Delta H_m}{W_P \cdot \Delta H_m^0} \times 100 \tag{2.2}$$

where ΔH_m is the enthalpy of melting the sample, ΔH_m^0 is the theoretical enthalpy of melting a fully crystalline sample (= 146 J g⁻¹ for PHB [44]) and W_p is the weight fraction of the polymer ($W_p = 1$ for a pure sample or $W_p < 1$ when additives have been incorporated).

In the current work, HCR cycles were carried out on the solvent cast films in order to determine the change in T_{m1} , T_c and X_c of PHB films caused by the incorporation of filler or plasticiser. Tests were done using the PerkinElmer DSC4000, calibrated using indium standard, with a HCR cycle. Nitrogen was used as a purge gas, with a flowrate of 20 mL min⁻¹. Nitrogen is chemically inert under the DSC conditions used and it helps to prevent oxidation or degradation of the polymer during heating. Additionally, the use of a continuous purge gas flushes out moisture, oxygen and volatile impurities from the DSC cell, ensuring consistent results. The cycle consisted of the following steps a) isothermal equilibration for 1 min at 313 K, b) heating at a rate of 10 K min⁻¹ from 313 K to 473 K,

c) isothermal equilibration for 2 min at 473 K, d) cooling at 10 K min⁻¹ from 473 K to 223 K, e) isothermal equilibration for 5 min at 223 K and f) heating at 10 K min⁻¹ from 223 K to 473 K. Heating to 473 K ensured the polymer was above its melting temperature but still below its thermal degradation temperature, while cooling the samples to 223 K ensured the polymer would be below both the crystallisation temperature and its glass transition temperature, allowing the detection of three distinct phase transitions. Similar HCR cycles have been used in the literature [49, 98]. Resulting DSC spectra were analysed using Pyris, the PerkinElmer instrument software. Results were averaged over three repeats per film. A typical DSC plot for PHB, from a HCR cycle is shown in Figure 2.6. The three peaks indicate T_c , T_{m2} and T_{m1} , from left to right.

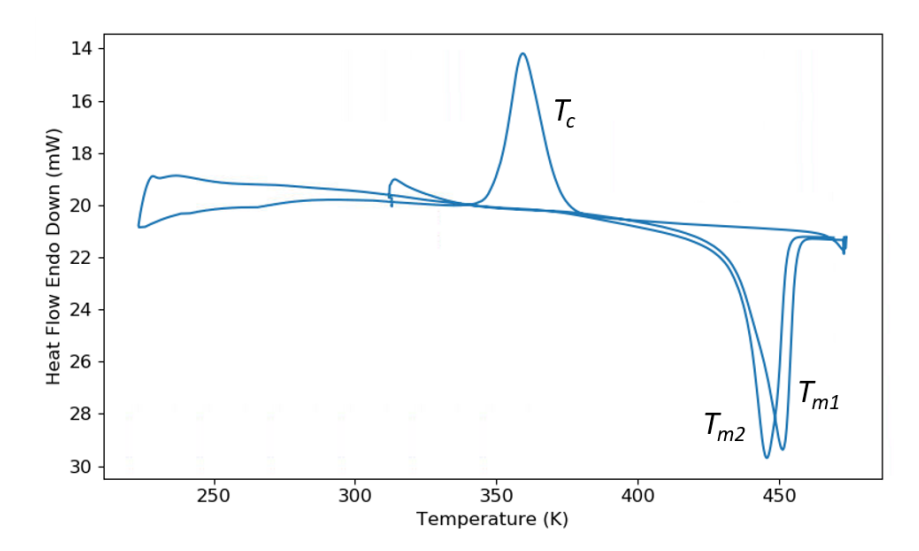


Figure 2.6: DSC curve of a PHB film sample, generated from a HCR cycle. The first heating step is shown by T_{m1} curve, the T_c curve then shows the cooling step and the second heating step is shown by the T_{m2} curve.

Scanning Electron Microscopy

SEM is a powerful imaging technique used to examine the surface morphology of materials at high magnification and resolution. In this work, it was particularly valuable for visualising the crystalline microstructure of PHB films, enabling direct observation of spherulite size, shape and distribution, and for assessing how these features were altered by the incorporation of fillers and plasticisers.

Unlike optical microscopy, which uses visible light and lenses, SEM operates by scanning a focused beam of high-energy electrons across the surface of a specimen. As the electrons interact with the atoms in the sample, they generate various signals, most notably secondary electrons, that are collected to produce a detailed image of the sample's topography. The electron beam in an SEM is generated in an electron gun and accelerated under vacuum through a series of electromagnetic lenses that focus the beam into a narrow spot. As the beam is scanned across the surface, detectors capture secondary electrons emitted from the sample's surface layers. The intensity of these signals depends on the surface features and composition, allowing fine surface details such as ridges, voids and crystallites to be visualised. Backscattered electrons and X-rays can also be detected for compositional analysis. For polymer films, SEM is particularly useful in characterising microstructural features, such as spherulites, cracks, voids and phase separation. In semicrystalline polymers like PHB, SEM can reveal the presence and size of spherulitic structures, which form as the polymer crystallises from the melt or solution. These features appear as radially grown crystalline domains and are key indicators of the polymer's crystallisation behaviour and thermal history.

In this work, imaging was carried out using a tungsten low-vacuum SEM (JEOL model JSM-IT100). For sample preparation, small pieces of polymer film were cut and affixed flat onto SEM sample holders using carbon adhesive tape. Sputter coating with metal nanoparticles was not required, as the SEM was equipped with a charge reduction holder. This system works by slightly increasing the chamber pressure to improve charge neutralisation on non-conductive samples such as polymers. During imaging, parameters including probe current, accelerating voltage and magnification were optimised to achieve clear visualisation of spherulites. Once images were obtained for each formulation, spherulite areas were analysed using image analysis software, including ImageJ and Segment Anything, an AI tool developed by Meta [14]. Changes in the size and distribution of spherulites, as well as the presence of defects or discontinuities in the film, provided insight into how formulation influences the final microstructure.

Water Contact Angle Measurements

Water contact angle measurements are commonly used to evaluate the surface wettability of polymer films, providing an indirect assessment of their water barrier properties. The technique involves placing a small droplet of water onto the surface of the polymer and measuring the angle formed between the droplet and the surface at the liquid-solid-air interface, shown in Figure 2.7.

A high contact angle (typically >90°) indicates a hydrophobic surface, where water tends to bead up rather than spread out, suggesting limited interaction between the polymer and water. Conversely, a lower contact angle (<90°) reflects a more hydrophilic surface, where water readily spreads, often correlating with higher water permeability or poorer barrier performance. While contact an-

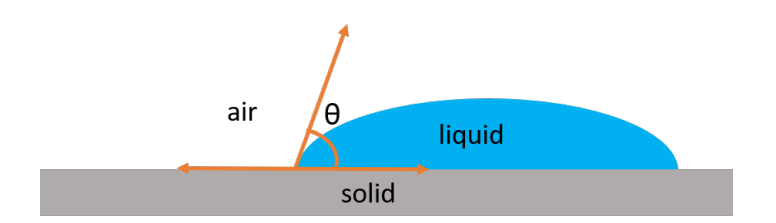


Figure 2.7: Contact angle formed at the solid/liquid/air interface.

gle does not measure water vapour transmission or absorption directly, it offers insight into the surface energy and potential interactions of the polymer with moisture. This is particularly useful for comparing surface modifications, polymer blends or coatings designed to enhance barrier properties. However, it is important to note that contact angle is a surface-sensitive technique and does not account for bulk characteristics such as porosity or internal microstructure, which also influence water barrier performance. Therefore, contact angle is best used in combination with other techniques like WVTR or gravimetric sorption measurements to build a more complete picture of a polymer film's barrier capabilities.

To measure the water contact angle on PHB films, the KRUSS (model DSA25E) apparatus was used with the drop shape analysis method in the KRUSS Advance software. This method involves capturing a high-quality image of a sessile drop on a surface and measuring the angle at the point of interaction between the drop contour and the projection of the surface (baseline). Before measurement, a test droplet of water was placed on the viewing platform in order to calibrate the camera zoom and focus to obtain clear images. After calibration, a small piece of film ($\approx 2 \times 2$ cm) was cut and placed on the platform, ensuring smooth contact with no kinks in the film. To ensure that that no dust or residues were present in the samples, the film surface was wiped with ethanol. A micropipette was used to place a 20 μ L drop of deionised water in the centre of the film and an image was taken as soon as the software detected the baseline and droplet. The contact angle was automatically measured using the circle method, which assumes the formation of a circular arc from the water droplet. An average was taken from five repeats for each film tested.

Water Permeation Measurements

Understanding how water vapour moves through polymer films is critical in evaluating their suitability for food packaging applications, where excessive moisture transfer can compromise product shelf life and overall performance. In order to test the permeability of water through polymer films, experiments can be run in which the mass of water transported through the film is measured over a set period of time. One widely recognised approach for this is the ASTM E96 stan-

dard (Standard Test Methods for Gravimetric Determination of Water Vapour Transmission Rate of Materials) [99], which provides a consistent framework for determining the WVTR of materials. This method involves sealing the film over the opening of a test dish and monitoring the rate at which water vapour passes through the film under controlled environmental conditions. Two variations of the method are commonly used: the dry cup and wet cup methods, which differ based on whether the water vapour is moving into or out of the test dish. For this project, the wet cup method was employed.

To set up the experiment, approximately 25 mL of deionised water was added to 30 mL glass jars, and pieces of polymer film were cut to size and affixed to the openings of the jars using epoxy resin adhesive. The adhesive was allowed to cure for approximately 20 minutes to ensure a secure seal. Subsequently, the sealed jars were weighed and placed in an oven maintained at 298 K. To create a dry testing environment, silica beads were placed in the oven and a temperature and humidity probe was utilised to verify stable conditions at both the beginning and end of the experiment. The experimental set up used is shown in Figure 2.8.

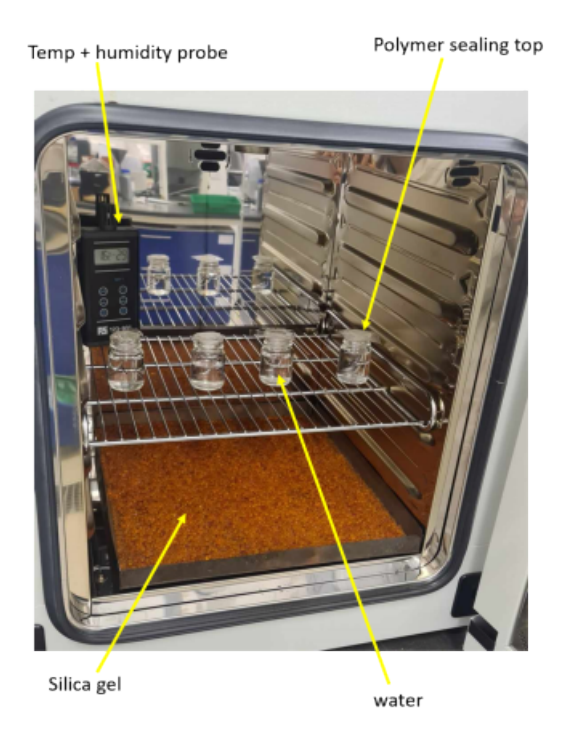


Figure 2.8: Experimental set up used to determine water vapour permeability. The system is contained in an oven held at 298 K.

Over time, water vapour migrates from the high-humidity environment inside the cup through the film to the drier external environment. The jars were left undisturbed in the oven for a duration of five days, with the oven door remaining closed in order to maintain consistent environmental conditions. After this time, the jars were reweighed to determine the mass of water lost due to permeation through the polymer films. From the mass lost, the WVTR is calculated using the following equation:

$$WVTR = \frac{\Delta m}{A\Delta t} \tag{2.3}$$

where Δm is the change in mass of water inside the dish, A is the exposed surface area of the film and Δt is the time period over which the measurement is taken. This method allows for the direct comparison of the water barrier performance of films with different compositions or treatments under controlled, repeatable conditions.

In addition to WVTR, water permeance and permeability are often reported when characterising the barrier properties of polymer films. Permeance is calculated by dividing the WVTR by the partial pressure difference of water vapour across the film. Unlike WVTR and permeance, permeability also accounts for the film thickness, making it a more intrinsic material property. While WVTR is typically expressed as the mass (or volume) of water transmitted per unit area per unit time, permeability introduces additional terms for film thickness and the water vapour partial pressure difference, ΔP . A commonly used unit for permeability is the Barrer, in which the volume of permeated water vapour is corrected to standard temperature and pressure (273 K, 1 atm) [100]. These units facilitate direct comparison with data reported for other polymers in the literature. The definitions, units and relationships between WVTR, permeance and permeability are summarised in Table 2.3.

To validate the water resistance of the epoxy sealant, a control experiment was conducted wherein jars were sealed with aluminium foil instead of polymer film. After five days in a dry oven, no detectable mass change was observed in any of the three samples, indicating effective sealing. Additionally, to assess the reliability of the experimental setup, polyethylene terephthalate (PET) films (50 microns thick, sourced from Fujifilm) were used as a substitute for PHB. Water vapour permeability in PET has been reported in the range of 130 - 410 Barrer [9, 101, 102]. An average permeability of 211 ± 4 Barrer was obtained from the current experiments on PET, which is within the range reported in literature. This further confirmed the validity of the experimental setup. These validation tests collectively demonstrate that the experimental setup was reliable and that the epoxy sealant maintained its water resistance throughout the duration of the WVTR tests.

Measurement	Calculation	Units
WVTR	$rac{m_w}{tA}$	$\mathrm{g}\;\mathrm{m}^{-2}\;\mathrm{d}^{-1}$
WVTR	$\frac{V_w}{tA}$	${\rm cm^3~cm^{-2}~s^{-1}}$
Permeance	$\frac{V_w}{tA\Delta P}$	${\rm cm^3~cm^{-2}~s^{-1}~cmHg^{-1}}$
Permeability	$rac{V_w l}{t A \Delta P}$	${\rm cm^3~cm~cm^{-2}~s^{-1}~cmHg^{-1}}$
Permeability	$\frac{V_w(STP)l}{t\ A\ \Delta P}$	Barrer $(\times 10^{-10} \text{ cm}^3(\text{STP}) \text{ cm cm}^{-2} \text{ s}^{-1} \text{ cmHg}^{-1})$

Table 2.3: Calculation and units of water permeation measurements. m_w and V_w are the mass and volume of water vapour, respectively, t is time, A and l are film area and thickness, respectively, and ΔP is the pressure difference of water vapour across the film.

Texture Analysis

Texture analysis is a valuable tool for characterising the mechanical behaviour of polymer films. In this study, it was used to quantify strength and elasticity of PHB films, providing direct insight into how the incorporation of additives modified their mechanical performance.

To carry out the tests, Stable Micro Systems model TA.XTplus100C was used. The testing procedure involved securing a small film sample $(2 \times 2 \text{ cm})$ between two metal plates, each containing a central hole. A pressure-sensitive spherical probe was then driven through the hole until it punctured the film. The key parameters recorded were the distance to burst and the force required for burst. The distance to burst was determined as the difference between the probe height at initial contact with the film and its height at the point of rupture, providing insight into the film's elasticity or brittleness. The force to burst represented the force required to puncture the film, serving as an indicator of the film's strength. Five replicates of each film formulation were tested and the average values are reported. Figure 2.9 shows a typical plot generated from texture analysis of a PHB film.

Although there are a range of standardised methods available for detailed mechanical characterisation such as tensile testing, which yields stress-strain curves and values for Young's modulus, tensile strength and elongation at break, this level of analysis was beyond the scope of the current project. Instead, texture analysis was selected as a practical and efficient alternative for comparing mechanical performance across film formulations. It offered a quick setup, minimal sample preparation and was well-suited to high-throughput screening, making it

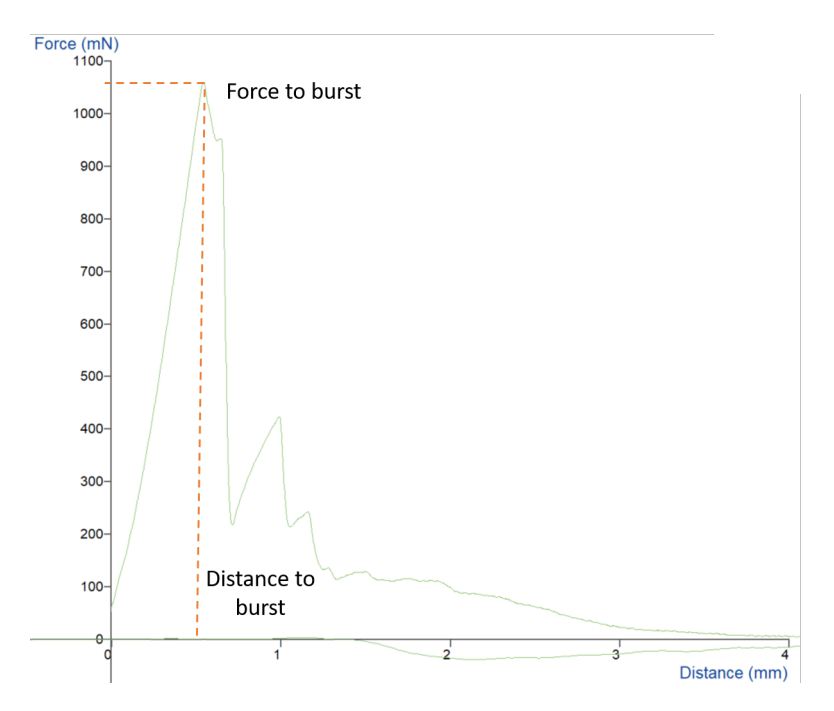


Figure 2.9: Plot from texture analysis, with the peak indicating the breaking point of the film.

an ideal tool for identifying trends in mechanical behaviour linked to compositional changes. Texture analysis data can be interpreted in conjunction with DSC results and SEM imaging to explore the influence of different formulations on the crystalline microstructure.

Chapter 3

A Versatile Molecular Dynamics Force Field for Modelling Polyhydroxyalkanoate Structure and Barrier Properties

Abstract

Polyhydroxybutyrate (PHB) is a sustainable and compostable polyester, which has great potential for use as food packaging film, having similar barrier properties to conventional plastics. PHB is semi-crystalline and is often copolymerised with polyhydroxyvalerate (PHV) to form poly(3-hydroxybutyrate-co-3-hydroxyvalerate) (PHVB). Molecular dynamics (MD) simulations provide valuable insight into the polymer structure and gas diffusion, but the accuracy of MD simulations depends on the force field. This work presents a modified all-atom General Amber Force Field that enables PHB, PHV and PHVB copolymers to be modelled. The structural properties of crystal and amorphous phases of PHB and PHV were in good agreement with experiment. The diffusion coefficients of water and oxygen in amorphous PHB were also in good agreement with experimental values. The diffusion coefficient of oxygen in PHV was larger than in PHB, mainly due to the lower density of PHV. The diffusion coefficient of water in PHV was similar to PHB as its diffusion is hindered by the interaction of water with the polar ester groups on the polymer chains. This force field can be used to investigate the diffusion of water and oxygen in PHB, PHV and PHVB copolymers, and to optimise the barrier properties of PHVB-based plastic film.

3.1 Introduction

Discarded plastic products accumulate in landfills, oceans, and other ecosystems, posing a serious threat to wildlife and the environment, while the production of plastic also contributes to the depletion of non-renewable petroleum resources [103]. One possible solution to the environmental problems posed by flexible packaging films is the use of compostable polymers. Polyhydroxyalkanoates (PHAs) are a family of polyesters which are both bioderived and biodegradable, eliminating the need for petroleum feedstocks. Polyhydroxybutyrate (PHB) and polyhydroxyvalerate (PHV) are the most widely used and researched members of the PHA family, owing to their good thermal [104] and barrier [19, 105] properties which make them viable substitutes for conventional thermoplastics such as polypropylene and polyethylene, particularly in food packaging applications.

The link between crystallinity and gas barrier properties is crucial for design of food packaging films, with strong barrier properties leading to better preservation of food products. Pure PHB crystallises readily, with the formation of large spherulitic structures in the polymer matrix. Spherulitic polymers are semi-crystalline, with the spherulites consisting of crystalline lamella interspersed with rigid amorphous regions [47]. Molecules generally do not penetrate the crystal regions [106], and will diffuse only through the amorphous or rigid amorphous regions.

PHB can be melt processed above the melting temperature of around 175 °C [58]. However, thermal decomposition has been reported at 219 °C [48], giving a rather narrow window for melt processing. Both of these problems in pure PHB can be mitigated by copolymerisation with PHV. One experimental study by Orts et al. found that incorporating 27 mol% of HV comonomers significantly lowers the melting temperature without affecting crystalline content [55]. PHV is chemically very similar to PHB, the difference being an extra CH₂ on the side group, as shown in Figure 3.1.

Figure 3.1: Chemical structure of (a) PHB (b) PHV.

Molecular dynamics (MD) simulations are a useful tool for providing insight

into how the structure of polymers affects their properties. Although there have been numerous experimental investigations carried out on PHB, the number of simulation studies published is relatively scarce [106]. While the existing MD studies provide a valuable insight into the structure and behaviour of PHB at a microscopic level [12, 65, 67, 68], they did not explore the crystal structure of PHB or PHV. Furthermore, to our knowledge, there are currently no published MD studies which investigate diffusion of water or oxygen through PHB.

In this work, we: i) develop a versatile force field for PHB and PHV that can also be used to study any combination of PHVB copolymers; ii) test the force field model for PHB and PHV in both amorphous and crystalline forms, with various structural and dynamic properties measured, and iii) calculate the diffusion coefficients of oxygen and water molecules in the amorphous phase of PHB and PHV and compare the results to experimental values. In this way, we demonstrate the versatility of our model, and pave the way to material design and the optimisation of PHA barrier properties.

3.2 Methodology

In this section we first describe the force field model, followed by the system set up, equilibration and production runs for the crystalline and amorphous systems. Finally, the methodology for simulations of oxygen and water diffusion in PHB and PHV is presented.

3.2.1 Force Field

The General Amber Force Field (GAFF) [74] was used for the bonded and non-bonded interactions in all simulations in this work. See Section 2.1.2, Chapter 2 for more details on GAFF. Moltemplate, a program for converting structure files into LAMMPS input files, was used to obtain the GAFF bonding and van der Waals (vdW) parameters [107]. This process involved writing a text file listing all of the atomic information (types, coordinates, charges) and bonds. The GAFF force field repository stored within the program was imported, which allowed the text file to be transformed into a LAMMPS data file containing all of the necessary topology information and force field parameters required to run a LAMMPS simulation.

The partial charge calculations were performed using PHA trimers with two distinct chain end monomers and a central monomer that can be repeated to create larger polymers, as shown in Figure 3.2. The partial charges were scaled slightly to ensure that i) the total charge on end group A was equal and opposite to the total charge on end group C, and ii) the total charge on repeat unit B

was zero, regardless of the R group used. This scaling allows charge neutrality to be maintained during the construction of both PHB and PHV homopolymer and copolymer chains. A full list of partial charges can be found in Appendix A.

Figure 3.2: PHA trimer used for the calculation of partial charges. For PHB \mathbf{R} is CH₃, and for PHV \mathbf{R} is CH₂CH₃.

In initial simulations of the polymer, an instability arose in which the terminal hydroxyl hydrogen (see unit \mathbf{C} in Figure 3.2) collapsed into the carboxyl oxygen three bonds away, and similar issues have been reported in the literature [108, 109]. This instability was a result of the zero values for LJ parameters σ and ε assigned to hydroxyl hydrogen atoms, as used in GAFF. To prevent this instability, we turned off the 1-4 non-bonded interactions between the hydroxyl hydrogen and carboxyl oxygen in the chain end labelled \mathbf{C} in Figure 3.2. This minor modification to the force field was only applied to the end \mathbf{C} monomer of each chain and does not affect the interactions with neighbouring chains. Further information can be found in Appendix A.

For the diffusion simulations, we used the simple point charge extended (SPC/E) water model [21], and the atomistic oxygen force field developed by Javanainen *et al.* [22]. Our calculated properties for bulk SPC/E water can be found in Appendix A.

3.2.2 Crystal Simulations

PHB and PHV infinite-chain crystals, where the start and end of the chains are bonded through the periodic c-axis of the perfect crystal, are studied. Moltemplate [107] was used to generate the LAMMPS data files containing all the topology information of the polymer systems.

To build the crystalline PHB model, the α -crystal unit cell based on the experimentally determined coordinates and cell parameters by Wang *et al.* were employed [11]. The PHB α -crystal consists of two anti-parallel chains twisted into a 2_1 helix (two monomers per one helical turn). The unit cell is orthorhombic, with a space group symmetry of $P2_12_12_1-D_2$ and lattice parameters a=5.73 Å,

b=13.15 Å, c=5.93 Å. The PHB α -crystal unit cell and helical structure are shown in Figure 3.3.

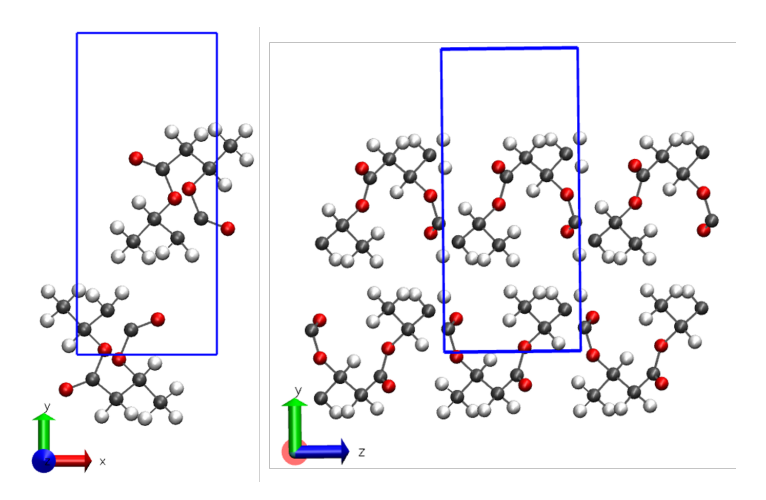


Figure 3.3: PHB α crystal, constructed using coordinates from ref [11]. Periodic bonding joins adjacent cells through the z axis.

To construct the PHV crystal unit cell, the CH₃ methyl side group in PHB was replaced by a CH₂CH₃ ethyl side group. Structural data such as lattice constants and torsional angles from the experimental study of Yokouchi et al. [17] were used to construct the PHV crystal lattice. The space group for PHV is the same as that of PHB and the initial lattice constants were a=9.32 Å, b=10.02 Å and c=5.56 Å. After setting up the crystals, an energy minimisation was carried out, using the steepest descent algorithm. After energy minimisation, a 50 ps NVT simulation at 200 K was performed. This was followed by a 10 ns NPT simulation at a temperature of 200 K and a pressure of 1 atm. A Nosé-Hoover thermostat and barostat (anisotropic) were used to control the temperature and pressure. Initial test simulations used a temperature of 300 K, in order to model the crystal at room temperature. However this higher temperature resulted in instabilities, which are discussed in Section 3.3.1.

To check crystal stability and confirm whether the chains had remained in their helical conformation during the NPT simulation, the backbone torsional angles and lattice parameters were monitored throughout the simulation. In order to test the thermal stability of the two crystalline systems, NPT simulations were performed with a linear temperature ramp increasing from 200 K at a rate of 2.5×10^{10} K s⁻¹ until the crystalline structure was lost with the chains separating.

The lattice energy (E_{lat}) of the energy-minimised crystal structure was calcu-

lated as:

$$E_{\text{lat}} = 2E_{\text{chain}} - E_{\text{unitcell}} \tag{3.1}$$

where E_{unitcell} is the potential energy of the bulk crystal unit cell and E_{chain} is the potential energy of a single, infinite helical chain with vacuum separating the chains in x and y. The lattice energy was converged by increasing the L_x and L_y box lengths from the unit cell lattice parameter values in increments of 2 Å until the energy changes were less than 0.08 kJ mol⁻¹. Since the cutoff distance for vdW and short-range electrostatic interactions was set to 10 Å, a 12 Å separation was sufficient to observe a plateau.

The surface energies (E_{surf}) of the energy-minimised polymer crystals were calculated as:

$$E_{\text{surf}} = \frac{E_{\text{slab}} - R_x R_y E_{\text{unitcell}}}{2A} \tag{3.2}$$

where $E_{\rm unitcell}$ is the potential energy of the bulk crystal unit cell, A is the surface area, and $E_{\rm slab}$ is the potential energy of a crystal slab containing R_x and R_y unit cells in the x and y directions, respectively. The (100) and (010) surfaces were created by separating the chains in the x and y directions, respectively. The (001) surface energy was not considered as the chains were infinite in the z-direction. The surface energies were converged with respect to the slab thickness by using the replicate function in LAMMPS to create crystalline systems with $R_{x,y}$ of 1, 2 and 4 unit cells thick. To converge $E_{\rm surf}$ with respect to the vacuum, the L_x and L_y box lengths were increased in 2 Å increments until the change in energy relative to the original system was less than 4 J mol⁻¹ Å⁻². Again, a 12 Å separation was sufficient to observe a plateau. Snapshots of the simulated slabs can be found in the supporting information as well as the convergence of the surface energies with slab and vacuum thickness.

3.2.3 Amorphous Simulations

Three different amorphous polymer systems with different chain lengths were investigated, namely pure PHB, pure PHV and the copolymer PHVB, with chains made up of 1) all HB monomers 2) all HV monomers or 3) alternating HB and HV monomers, respectively. To create these systems, a single chain of 10 monomers was first run for 50 ps in the NVT ensemble at 500 K to allow the chain to relax into a coiled configuration. This elevated temperature was used as it is roughly 50 K higher than the experimental melting temperature of PHB (448 K [58]) ensuring the polymer is in the melt phase. Then 50 relaxed chains were inserted with random positions and orientations inside a cubic simulation box with sides of length 40 Å. Figure 3.4 shows a coiled 10-monomer PHB chain and the corre-

sponding amorphous PHB melt containing 50 chains.

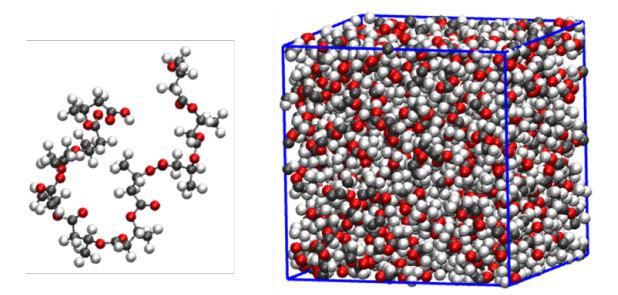


Figure 3.4: Snapshots of a single PHB chain and an amorphous PHB melt consisting of 50 chains, 10 monomers long.

For pure PHB, three additional systems were constructed with 5, 20 and 50 monomer chains. Systems are referred to as M=5, 10, 20 or 50. The total number of monomers in the amorphous system was kept constant at 500 by adjusting the number of chains inserted (100 chains for M=5, 25 chains for M=20 and 10 chains for M=50). After random insertion of the coiled chains, a short NVT simulation of 10 ps was performed at 500 K using soft pairwise potentials to remove high energy configurations with overlapping atoms. The pairwise potentials were then switched back to the Lennard-Jones/Coulomb settings for a 50 ps NVT run followed by a final NPT simulation using a Nosé-Hoover thermostat and barostat (isotropic) at 500 K and 1 atm. The duration of the NPT equilibration run increased with increasing chain length (20 ns for M=5, 30 ns for M=10, 50 ns for M=20 and 250 ns for M=50). Equilibration was checked using several measures:

- i. the density of the system reached a steady state.
- ii. the radius of gyration $(R_{\rm g})$ and chain end-end distance $(R_{\rm e})$ reached a steady state and had the typical ratio of a polymer melt where $\langle R_{\rm e}^2 \rangle = 6 \langle R_{\rm g}^2 \rangle$ [110].
- iii. the mean squared displacement (MSD) of the chains surpassed a distance of R_g^2 .
- iv. the end-to-end vector autocorrelation function (ACF) (denoted $R_{ee}(t)$):

$$R_{\rm ee}(t) = \frac{1}{N} \sum \frac{R_{\rm e}(t) \cdot R_{\rm e}(t_0)}{|R_{\rm e}(t)||R_{\rm e}(t_0)|}$$
(3.3)

decayed to 1/e.

v. plotting the potential energy with time to ensure it plateaued to a constant value and to check for any sudden spikes in energy which could indicate system instability.

After equilibration was complete, the system was run for an additional 10 ns in an NPT ensemble at 1 atm and 500 K from which system equilibrium properties were analysed. Since most experimental properties of polymers in the literature are reported at room temperature, the M=10 systems were also analysed at 300 K. For these simulations, the 500 K systems were cooled to 300 K at a rate of 2.5×10^{10} K s⁻¹ and then run for a further 5 ns at 300 K and 1 atm to allow for thermal equilibration and volume changes associated with the lower temperature.

To calculate $T_{\rm g}$, the equilibrated polymer melts were cooled from 500 K to 100 K at a steady rate of 2.5×10^{10} K s⁻¹. $T_{\rm g}$ was estimated for each equilibrated amorphous system by analysing the changes in density $\rho(T)$ upon cooling. $T_{\rm g}$ was estimated from the intersection of linear fits to the $\rho(T)$ data in high (400-500 K) and low (100-200 K) temperature ranges [111].

To compute the polymer persistence length (L_p) , which is a measure of chain stiffness, the polymer module in MDAnalysis [71] was used. This computes the autocorrelation of two bond vectors, separated by n bonds:

$$C(n) = \langle \cos \theta_{i,i+n} \rangle = \langle \mathbf{a_i} \cdot \mathbf{a_{i+n}} \rangle \tag{3.4}$$

and fits the data to an exponential decay function:

$$C(n) \approx \exp\left(-\frac{n\bar{l_B}}{L_p}\right).$$
 (3.5)

Here, n is the number of bonds separating the two bond vectors and \bar{l}_B is the average bond length in the polymer backbone ($\bar{l}_B = 1.46 \text{ Å}$).

The Hildebrand solubility coefficient (δ) is determined as

$$\delta = \sqrt{\frac{E_{\rm coh}}{V_m}} \tag{3.6}$$

where V_m is the molar volume of the amorphous system and E_{coh} is the amorphous cohesive energy defined as

$$E_{\rm coh} = \sum_{i=1}^{N} E_{\rm chain}^{i} - E_{\rm bulk}$$
 (3.7)

where E_{bulk} is the potential energy of the amorphous system of N chains, and E_{chain}^{i} is the potential energy of each single chain, i, in its melt configuration. This was calculated for three different snapshots in the trajectory to get an average E_{coh} and standard deviation. The resulting units for δ are $(\text{J cm}^{-3})^{0.5}$, which is equivalent to the commonly reported units of $(\text{MPa})^{0.5}$.

3.2.4 Diffusion Simulations

The diffusion of oxygen and water molecules in amorphous PHB and PHV was studied using systems with 10 and 20 monomer chains. After equilibration of the polymer systems (described previously), water or oxygen molecules were inserted with random positions and orientations into the amorphous matrix. The number of molecules that were inserted into the dense polymer matrix was 13 in all systems. This number is somewhat arbitrary, as it arose from the random insertion algorithm used in LAMMPS, but it was chosen to balance two considerations: maintaining a low permeant concentration to avoid possible clustering of permeants, while ensuring sufficient statistics for calculating diffusion. Youn et al. reported a saturation range for water in PHB of $1.5-11.0 \times 10^{-3}$ g(water)/g(polymer) [19]. Our setup corresponds to 0.1×10^{-3} g(water)/g(polymer) for the M = 10 PHB system, i.e. roughly an order of magnitude lower than the experimental solubility range. This was considered appropriate, as the simulations were intended to represent dilute permeant diffusion from the gas phase rather than bulk liquid water uptake. Although the number of permeant molecules was not explicitly varied, the results were not expected to differ significantly for other values at such low concentrations. Running multiple long-timescale diffusion simulations with different permeant numbers would substantially increase computational cost, and therefore the environmental impact of high-performance computing, without adding meaningful insight. Furthermore, the diffusion coefficients obtained with 13 permeants were found to be in reasonable agreement with the range of values reported experimentally, supporting the validity of the chosen setup.

After an energy minimisation, the system was run for 10 ps in the NVT ensemble at 500 K followed by 1 ns NPT simulation at 500 K and 1 atm to allow changes in volume to accommodate the inserted molecules. After equilibration, a production run was carried out for 200 ns in the NVT ensemble. During the production run, the centre of mass of the system was fixed to ensure that the calculated MSDs of the permeants were not affected by centre-of-mass drift. This process was repeated once more at 500 K to enable average MSDs to be computed. In order to compare with experimental diffusion studies carried out at room temperature, the same steps were then carried out at 300 K, this time with three independent runs to improve statistics.

The MSD Analysis module from the MDAnalysis library [71] was used to calculate the target species' MSD, denoted S(t), defined as follows:

$$S(t) = \left\langle \frac{1}{N} \sum_{i=1}^{N} |r_i(t+t_0) - r_i(t_0)|^2 \right\rangle_{t_0}$$
 (3.8)

where N is the number of diffusing particles of the target species, $r_i(t)$ represents

the coordinates of the particle at time t and the angled brackets denote averaging over reference positions using multiple time origins t_0 . Diffusion coefficients were obtained from the MSDs using the Einstein formula:

$$D = \frac{1}{6} \frac{d}{dt} S(t) \tag{3.9}$$

The MSD data was averaged over all runs for the specific temperature and chain length. Averaging the data from multiple simulations produced an MSD curve with less noise and wider range of linear trend. The time interval in which the slope was most linear was chosen for analysis. For the 500 K systems, this was approximately the first 175 ns and at 300 K the linear region selected was roughly 15 to 170 ns. Further details on this process can be found in Appendix B. A Python linear regression model was used to fit a trendline to this region and the regression coefficient (R^2) was used to determine the accuracy of the fit. An extra check of the linearity of the MSD plot, and therefore the Einstein diffusion regime, involved plotting $\log(\text{MSD})$ vs $\log(\text{time})$ and confirming that the gradient of this slope was close to a value of one [15]. Once the linear region was deemed suitable, the diffusion coefficient (D) was calculated from the gradient of this line.

3.3 Results and Discussion

In this section, we first present the properties of crystalline PHB and PHV, then present the properties of amorphous PHB, PHVB, and PHV. Finally, we investigate the diffusion of water and oxygen through PHB and PHV and report the diffusion coefficients.

3.3.1 Crystal Properties

The PHB and PHV unit cell lattice parameters (a, b and c) and density (ρ) for the energy minimised structures and averaged values for 10 ns NPT simulations at 200 K, are shown in Table 3.1. As expected, the average lattice parameters from NPT simulations are larger than the energy minimised lattice parameters due to thermal fluctuations when temperature is applied to the system. The lattice parameters and density calculated at 200 K are in very good agreement with experimentally obtained values from previous works [11, 16, 17] although we note that our simulations were at a lower temperature than experimental measurements.

The most common torsional angles adopted by the PHB backbone (indicated by peaks of the histograms in Figure 3.5) are listed in Table 3.2 and are in good agreement with experimental measurements [11, 17, 45].

	T (K)	a (Å)	b (Å)	c (Å)	$\rho \; (\mathrm{g} \; \mathrm{cm}^{-3})$	
PHB						
Emin	0	5.73	12.72	5.93	1.32	
NPT	200	5.86 ± 0.15	12.86 ± 0.29	6.02 ± 0.12	1.26 ± 0.04	
Expt [11]	296	5.73 ± 0.01	13.15 ± 0.02	5.93 ± 0.01	1.28 ± 0.01	
Expt [16]	_	5.76	13.20	5.96	1.24 ± 0.01	
PHV						
Emin	0	9.42	9.95	5.58	1.27	
NPT	200	9.67 ± 0.19	10.11 ± 0.23	5.63 ± 0.11	1.21 ± 0.03	
Expt [17]	_	9.32	10.02	5.56	1.20	

Table 3.1: Crystal properties of energy minimised structures and NPT simulations at 200 K (averaged over 10 ns) compared with experimental properties. NPT data points were sampled every 1 ps and average values are reported \pm the standard deviation. Experimental densities were measured using the flotation method [16, 17] or calculated from reported lattice constants [11].

	Present	Yokouchi [16]	Cornibert [45]	Wang [11]
ω	127	128	123	116
ϕ	132	133	148	143
ψ	0	5	0	11
τ	341	332	321	331

Table 3.2: Comparison of PHB torsional angles (°) with literature data.

A visual analysis of the NPT simulation at 200 K shows that the polymer chains remain in their helical conformation and the backbone torsional angle distribution is shown in Figure 3.5.

The stability of the crystals during the NPT simulations at 200 K was confirmed by plotting the torsional angles and the lattice parameters with time, which are shown in Appendix B. The crystal stability with temperature was further investigated by heating from 200 K to 400 K at a rate of 2.5×10^{10} K s⁻¹ using NPT at 1 atm. The PHV crystal becomes unstable at ≈ 233 K, compared to ≈ 327 K for the PHB crystal, which is consistent with the experimental trend. Thermal instabilities for the crystal models can be seen through plots of lattice parameters with increasing temperature, shown in Appendix B. We note that these temperatures in the simulations where the instabilities arise overestimate the melting temperatures of the model as the simulations use infinite chains.

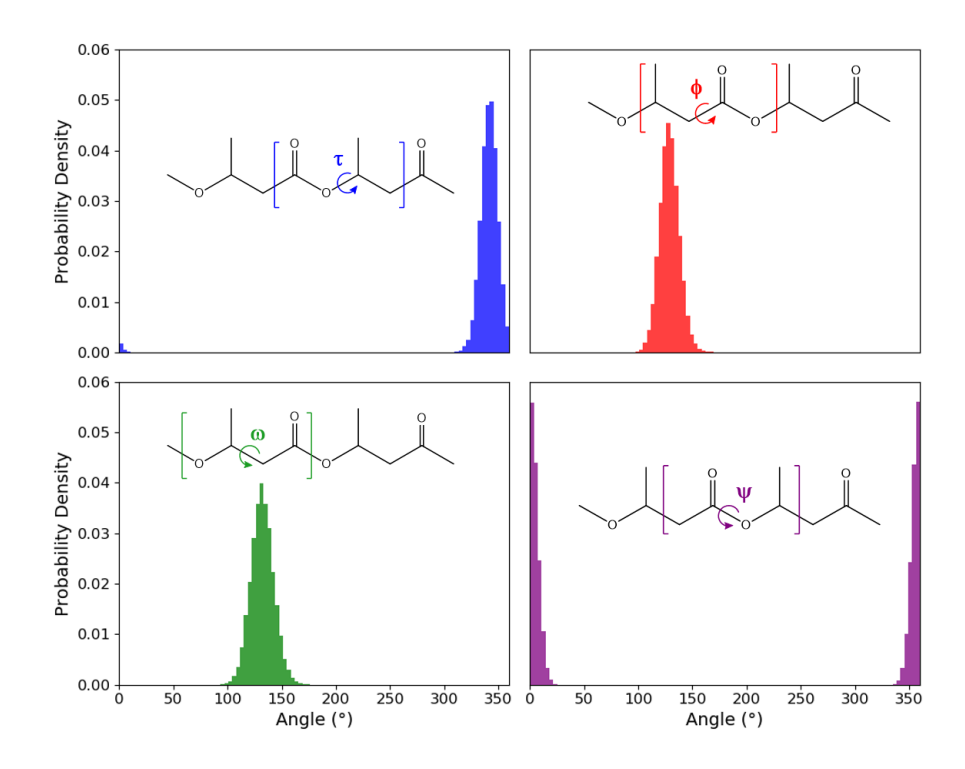


Figure 3.5: Histograms showing the four main backbone torsional angles along the helical PHB backbone.

The lattice energy was found to be 164.62 kJ mol⁻¹ for PHB and 98.54 kJ mol⁻¹ for PHV, equivalent to 1.71 eV and 1.02 eV per unit cell for PHB and PHV, respectively. The higher lattice energy of PHB compared to PHV is expected as the larger side group in PHV keeps the chains further apart, resulting in less stable crystals, lower lattice energy, and lower melting temperature of 378 K for PHV [16] compared to 448 K for PHB [58]. We were unable to find experimental values for the lattice energy of PHAs, but these values are comparable to polyethylene's lattice energy of 0.80 eV per unit cell [112] and to density functional theory (DFT) calculations of the lattice energies of poly(vinyl chloride) and poly(glycolic acid) of 0.87-0.95 eV and 1.45-1.55 eV per unit cell, respectively [113].

The (100) and (010) surface energies for PHB are 162.6 mJ m^{-2} and 90.5 mJ m^{-2} , respectively. The (100) surface energy is significantly higher than the (010) surface energy, which is consistent with the work by Mori *et al.* who reported that hydrogen bonding between CH₃ and C=O groups in the x axis are stronger than the vdW interactions in the y axis [114]. These neighbouring groups are highlighted in Figure 3.6. The (100) and (010) surface energies for PHV are 90.3 mJ m⁻² and 86.8 mJ m^{-2} respectively. The difference in surface energies of the two planes is much smaller for PHV than PHB. The lower (100) surface energy for PHV is con-

sistent with the direction of the ethyl side group, shielding the effects of the polar carbonyl group in the x axis. In the y axis in PHV, there is sufficient distance between a polar C=O group and the CH₃ group on a neighbouring chain, offering limited resistance to separation of chains in this direction.

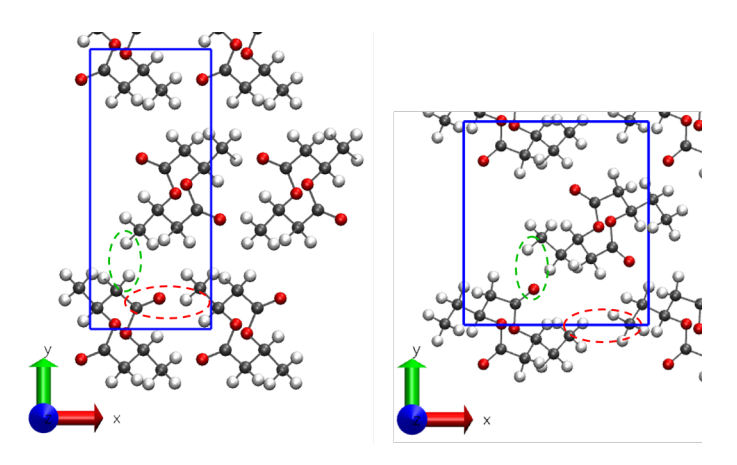


Figure 3.6: PHB (left) and PHV (right) unit cells with periodic images shown. Non-bonded interactions between neighbouring chains which contribute to the surface energy are highlighted.

Experimentally measured surface energies are reported to be in the range from $34-40 \text{ mJ m}^{-2}$ [96, 115, 116] for PHB, and 24.6 mJ m⁻² for a 12 mol % HV copolymer [117], which are much smaller than our simulated values, although the trends are in agreement. It should be noted that PHAs are typically semi-crystalline, and it is possible that amorphous content present in the experimental samples leads to a lower measurement of surface energy in comparison to the perfect crystal structure in the current simulations. The discrepancies between simulated and experimental polymer crystal surface energies may also stem from the choice of force field, as different force fields may not accurately capture the complex intermolecular interactions and structural properties of polymers, leading to variations in computed surface energies. Our results are comparable to calculated surface energies of 166 and 176 mJ m⁻² for fully crystalline PET and PEF atomistic MD models, respectively [85]. Although comparable to the those computed by DFT calculations [85], the PET and PEF surface energies obtained by MD methods are also an order of magnitude higher than the experimental polymer surface energies $(41.0 \text{ and } 61.7 \text{ mJ m}^{-2} \text{ for PET } [118] \text{ and PEF } [119], \text{ respectively}).$

While the absolute values of energetic properties of polymer crystals computed by MD methods are difficult to compare to experimentally determined values, the trends observed when comparing PHB and PHV are consistent with the data available in the literature, demonstrating that the modified GAFF force field gives a good description of the PHA crystal structures in the α -phase. It should be noted, however, that the simulated crystals are made of infinite helical chains and the effect of chain ends on the stability of the systems has not been tested.

3.3.2 Amorphous Polymer Properties

The density of the amorphous systems at 300 K and 500 K are reported in Table 3.3. It was expected that density would increase slightly with increasing molecular weight due to fewer chain ends disrupting the packing efficiency, however this trend was not observed here. It is plausible that the M=50 chains needed longer to equilibrate, however the densities obtained for all systems are within 0.02 g cm⁻³ of reported experimental [120] and simulation [12, 68] values. Furthermore, the trend of decreasing density with increasing HV content observed by both Barker et al. [120] and Papchenko et al. [68] is observed here. This effect is a result of the larger side group present in HV monomers.

			ρ (g o	em^{-3})
Polymer	Source	M	300 K	500 K
PHB	Present	5	1.17	1.05
PHB	Present	10	1.17	1.05
РНВ	Present	20	1.17	1.04
PHB	Present	50	1.16	1.04
PHB	MD [12]	150	1.15	1.03
РНВ	MD [68]	150	1.19	-
РНВ	Expt [120]	-	1.18	-
PHVB	Present	10	1.14	1.01
PHVB	MD [68]	150	1.15	-
PHVB	Expt [120]	-	1.14	-
PHV	Present	10	1.10	0.97
PHV	MD [68]	150	1.12	-
PHV	Expt [120]	_	1.11	-

Table 3.3: Density of amorphous PHAs, from current work and literature data. All densities reported from the current work are averages from NPT runs, with standard deviations $\leq 0.01 \text{ g cm}^{-3}$.

The glass transition temperature was obtained from the change in density gradient during cooling from 500 K to 100 K, as described in the methodology. This

is shown for the PHB M=10 system in Figure 3.7.

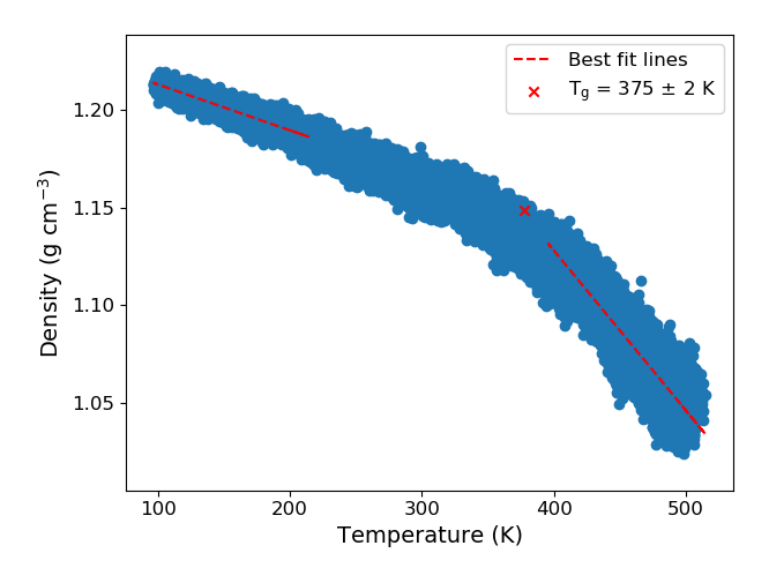


Figure 3.7: Density vs temperature on cooling PHB from 500 K to 100 K. Lines were fitted to data in the ranges 100 K to 200 K and 400 K to 500 K, with $T_{\rm g}$ taken as the point of intersection. The uncertainty in $T_{\rm g}$ was calculated using the standard error of the gradient of the best fit lines.

The glass transition temperatures for each system are given in Table 3.4. It can be seen that the addition of HV monomers lowers the $T_{\rm g}$, compared to pure PHB, in agreement with the trend observed experimentally, and is due to the bulkier HV side groups creating steric hindrance and affecting the polymers ability to pack into a dense, glassy configuration [49].

Polymer	M	$T_{\rm g}$ (K)
PHB	5	349 ± 3
PHB	10	375 ± 2
PHB	20	363 ± 3
PHB	50	350 ± 4
PHVB	10	328 ± 3
PHV	10	319 ± 2

Table 3.4: $T_{\rm g}$ of each amorphous system.

It would be expected that $T_{\rm g}$ would increase as chain length increases, in accordance with the Fox-Flory relationship [121]:

$$T_{\rm g} = T_{\rm g}^{\infty} - \frac{K_g}{M_w} \tag{3.10}$$

where $T_{\rm g}^{\infty}$ is the asymptotic glass transition temperature reached at infinite polymer molecular weight (M_w) and K_q is an adjustable polymer-specific constant which accounts for the free volume contribution of chain ends. However, the trend in $T_{\rm g}$ with increasing PHB chain length is unclear. It is possible that the cooling rates used in the $T_{\rm g}$ simulations should have been lower for the longer chain systems, to allow greater time for density to adjust at each new temperature. $T_{\rm g}$ can vary depending on the cooling rate used, with faster cooling generally leading to higher $T_{\rm g}$ values [122, 123] as the polymer is 'frozen' into a higher-energy configuration. McKechnie et al. have previously shown that increasing the cooling rate by two orders of magnitude can lead to an increase in T_g by ≈ 40 K [124]. Additionally, the present work has only one cooling simulation per system, and it has been shown that there can be significant statistical variation in $T_{\rm g}$ across multiple repeat simulations [124]. Our values are in line with $T_{\rm g}=374\pm6~{\rm K}$ found by Glova et al. for a 150 monomer PHB system [12], however, they are significantly higher than the experimental $T_{\rm g}$ of 275-288 K [125]. This discrepancy is commonly observed in atomistic simulations of polymers because the cooling rates applied in simulations are more than 10 orders of magnitude greater than those used in experiments, although it may also be due to the force field itself, or statistical variation.

We note that the $T_{\rm g}$ obtained here for PHB and PHV are higher than the estimated melting temperatures of the crystals, described in Section 3.3.1. Experimentally, PHB melts at 448 K, and becomes a glass at around 275-288 K [58, 125]. The model does not reproduce the crystal phase transition or glass transition behaviour of the real PHB system, and would not be capable of crystallising PHB from the melt, as the polymer would become a glass above the crystallisation temperature. However, it may still be possible to study semi-crystalline structures, by partially melting non-infinite chain crystals, and then cooling to below $T_{\rm g}$. Alternatively, future work could involve connecting crystalline PHA structures to an amorphous PHA matrix via tie-chains, as has been done by Atiq *et al.* for polyethylene [126], in order to model the semi-crystalline polymer. The glassy amorphous phase in between crystals may be a reasonable approximation for the rigid amorphous phase in semi-crystalline PHB.

The ensemble averaged radius of gyration and end-to-end distance, $R_{\rm g}$ and $R_{\rm e}$, computed from the NPT simulations at 500 K are shown in Table 3.5, along with literature values computed by Glova *et al.* [12]. As expected, $R_{\rm g}$ and $R_{\rm e}$ follow an $M^{0.5}$ scaling (see Figure 3.8). Extrapolating to M=150 gives $R_{\rm g}=31$ Å and $R_{\rm e}=72$ Å, which is in good agreement with the values of 32 Å and 79 Å reported by Glova *et al.* We also note, from the trendlines in Figure 3.8, that $5.9^2/2.5^2\approx 6$,

as expected for an equilibrated melt [110].

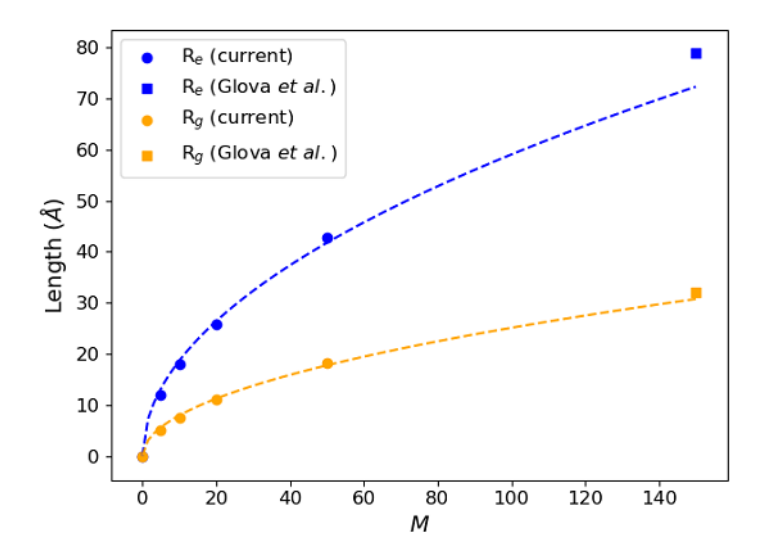


Figure 3.8: $R_{\rm g}$ and $R_{\rm e}$ vs number of monomers M of PHB. Dashed lines are fits to results from current study: $R_{\rm e}=5.9~M^{0.5}$ and $R_{\rm g}=2.5~M^{0.5}$. The trendlines are extrapolated to M=150 for comparison to literature results by Glova *et al.* [12].

The persistence length (L_p) is a measure of the flexibility of the polymer chain. As seen in Table 3.5, the average L_p of PHB in the current study is in the range 6.3-7.0 Å, and is independent of chain length, as expected. PHV and PHVB have average persistence lengths similar to PHB within the range of uncertainty, which is consistent with their similar $R_{\rm g}$ and $R_{\rm e}$ values for the M=10 systems.

The characteristic ratios (C_{∞}) reported by Kyles and Tonelli (MD) [67] and Sasanuma *et al.* (experimental) [127] can be used to calculate L_p , according to the equation:

$$L_p = \frac{\bar{l}_B(C_\infty + 1)}{2} [128] \tag{3.11}$$

where the average bond length in the backbone, \bar{l}_B , is 1.46 Å. The L_p of PHB obtained here is in line with that reported in other MD studies [12, 67]. It is also in agreement with the experimentally obtained L_p of 5.2 Å, reported by Sasanuma et al. [127]. However, Beaucage et al. obtained L_p values of 26-31 Å (depending on the method used) in their experimental study [128], which are significantly higher than the current results. The higher values obtained may be a result of the semi-crystalline nature of their samples, which were obtained from quenching

Polymer	Source	M	T (K)	L_p	(Å)	$R_{\rm g}$	(Å)	$R_{ m e}$	(Å)
PHB	Present	5	500	6.8	$\pm \ 0.4$	5.1	$\pm \ 0.1$	12.0	± 0.4
PHB	Present	10	500	6.7	± 0.4	7.6	± 0.2	18.1	± 0.8
PHB	Present	20	500	6.5	± 0.9	11.0	± 0.4	25.9	± 2.1
PHB	Present	50	500	7.0	$\pm~0.8$	18.2	± 1.5	42.7	± 5.8
PHVB	Present	10	500	6.6	$\pm~0.7$	7.7	± 0.2	18.4	$\pm~0.8$
PHV	Present	10	500	6.2	± 0.5	7.7	± 0.2	18.1	± 0.9
PHB	Present	10	300	6.3	± 0.5	7.3	± 0.1	16.5	± 0.2
PHB*	MD [67]	100	500	6.5	_	-	_	-	-
PHB	MD [12]	150	550	5.0	± 1.0	79	-	32	-
PHB*	Expt [127]	_	298	5.2		_	-	_	-
PHB	Expt [128]	_	_	26-31	-	_	-	_	-

Table 3.5: L_p , R_g and R_e of amorphous PHAs. PHB* was calculated from reported characteristic ratios using equation 3.11.

molten PHB. Elongated crystalline polymer chains would be expected to have a higher L_p , and therefore higher stiffness, compared to randomly coiled amorphous chains. This consistency with both simulation and experiment in the literature shows that PHB chain stiffness is represented well in the current simulation model.

The Hildebrand solubility parameter (δ) quantifies the cohesive energy density of a polymeric material, reflecting the intermolecular forces within it; materials with similar δ values are likely to be miscible [12]. The cohesive energies ($E_{\rm coh}$) and δ for the amorphous systems are shown in Table 3.6, as well as those previously reported in the literature. δ as a function of chain length is plotted in Figure 3.9.

It can be seen that both $E_{\rm coh}$ and δ decrease as the chain length increases, but they more or less plateau at M=50. The cohesive energy of 25.1 kJ mol⁻¹ mon⁻¹ for the M=50 PHB system in the current work is in agreement with the cohesive energies computed in other simulation studies [12, 68]. It is also lower than the lattice energy of 41.2 kJ mol⁻¹ mon⁻¹ for the infinite-chain crystal, which is to be expected, since crystalline polymers exhibit ordered structures with efficient chain packing in conformations that maximise intermolecular forces, leading to higher cohesive energies. For the longer chain systems (M=20 and M=50) the solubility parameters are in agreement with an experimental value of 19.8 (MPa)^{0.5} reported by Terada and Marchessault [13]. Comparing the M=10 chains, it can be seen that the solubility parameter decreases with HV content. This trend has

Polymer	Source	M	$E_{\rm coh}~({\rm kJ~mol^{-1}~mon^{-1}})$	$\delta (\mathrm{MPa^{0.5}})$
PHB	Present	5	48.8	25.2
PHB	Present	10	37.1	22.1
PHB	Present	20	30.5	20.1
PHB	Present	50	25.1	18.3
PHB	MD [12]	150	23.3	17.6
PHB	MD [68]	150	26.4	19.2
PHB	Expt [13]	_	-	19.8
PHVB	Present	10	39.3	21.5
PHVB	MD [68]	150	25.2	17.6
PHV	Present	10	39.4	20.5
PHV	MD [68]	150	25.6	17.0
PHV	Expt [13]	_	-	19.4

Table 3.6: $E_{\rm coh}$ and δ for PHA systems from the present work computed at 300 K and from literature. Results from present work were averaged over three snapshots of a trajectory. Standard deviation ≤ 0.3 kJ mol⁻¹ mon⁻¹ for $E_{\rm coh}$ and ≤ 0.2 MPa^{0.5} for δ .

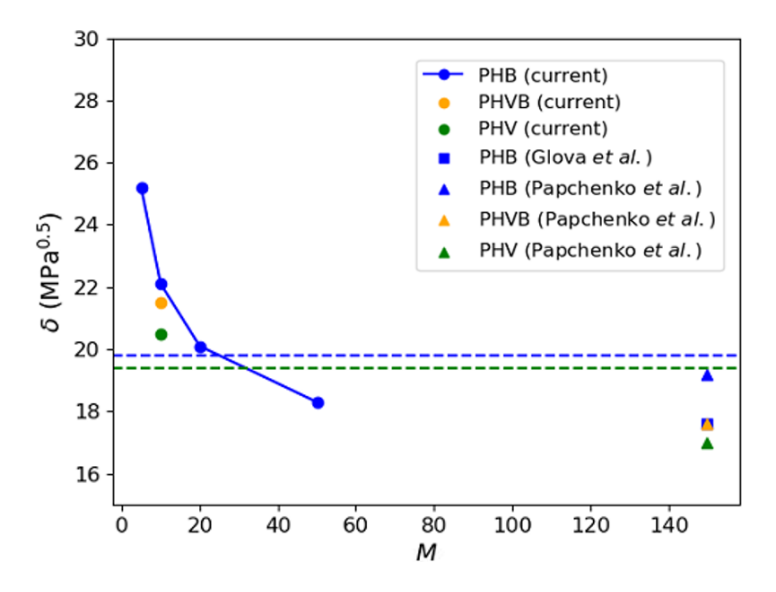


Figure 3.9: δ vs M for PHAs from current study and literature. Dashed lines show experimental values for PHB (blue) and PHV (green) [13].

been observed in both previous simulation and experimental studies [13, 68]. The addition of ethyl side chains can be attributed to the reduction in cohesive energy density. The introduction of ethyl groups decreases polymer density, leading

to weaker intermolecular interactions and, consequently, a lower solubility. This trend aligns with the understanding that bulkier side chains can disrupt polymer packing, reducing cohesive forces and solubility parameters [13].

Now we present the polymer dynamics of the amorphous systems at 500 K. The autocorrelation function of the end-to-end vector ($R_{\rm ee}$) was calculated for the different systems, and τ is the time taken for $R_{\rm ee}$ to decay to 1/e. As expected, τ increases for longer chains, and a longer equilibration time and duration for MSD calculations were required. The uncertainty in τ also increases significantly to 36% for the longest chain system. τ increases with increasing HV content in the M=10 chains, most likely due to the added steric restrictions from the side groups.

Polymer	M	τ (ns)	$D (\times 10^{-8} \text{ cm}^2 \text{ s}^{-1})$
PHB	5	1.0 ± 0.1	55.4 ± 0.6
PHB	10	4.0 ± 0.2	25.8 ± 0.5
PHB	20	14.6 ± 3.3	5.5 ± 0.1
PHB	50	74.8 ± 27.0	4.0 ± 0.2
PHVB	10	5.5 ± 0.5	33.4 ± 0.2
PHV	10	6.8 ± 0.3	31.1 ± 0.7

Table 3.7: Polymer relaxation times $\tau \pm$ standard deviation across multiple simulation windows. Polymer self-diffusion coefficients D (500 K) \pm standard error in slope of line fitted to MSD curves.

Figure 3.10 shows the MSDs for the amorphous systems, and the self-diffusion coefficients (D) computed from them are shown in Table 3.7. As expected, the short polymer chains diffuse more rapidly than the longer chains, leading to higher self-diffusion coefficients. The self-diffusion coefficient is seen to increase as the number of HV monomers increases. The self-diffusion coefficient is larger for PHV and PHVB, than for PHB. This could be a result of the increased free volume and lower density of the systems containing bulky HV side groups, allowing the PHVB and PHV chains to diffuse more readily throughout the matrix. It could also be attributed to the lower glass transition temperatures for PHV and PHVB, meaning that PHV is at a higher temperature relative to its $T_{\rm g}$. However, we would also expect the higher self-diffusion coefficient to correspond to a decrease in τ , so it is possible that the relatively small differences between these systems are within the level of uncertainty.

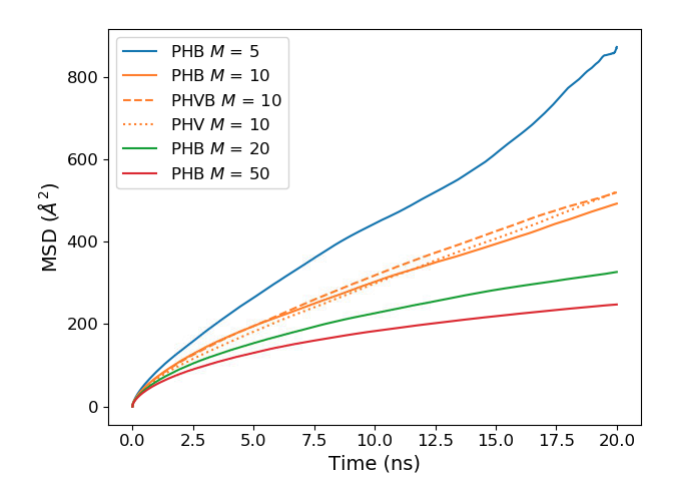


Figure 3.10: MSDs of amorphous polymer systems with different chain lengths, run in NPT ensemble at 500 K and 1 atm.

3.3.3 Diffusion of Oxygen and Water Molecules

We now turn to the diffusion of permeants in PHB and PHV. The diffusion coefficients for the various systems studied are shown in Table 3.8, along with experimental data from literature. For all systems, diffusion occurs much more rapidly at 500 K compared to 300 K, as expected, and the diffusion coefficients are approximately three orders of magnitude larger at 500 K. This difference could be due to the higher kinetic energy of the molecules themselves, or could be due to the increased mobility of the polymer matrix. As discussed previously, at 300 K the simulated PHB is in a glassy amorphous state with limited chain mobility, whereas at 500 K it is in a mobile, amorphous phase.

To test this conjecture, simulations were performed in which the polymer was kept immobile (with no thermostat applied) and the permeants had a temperature of 500 K. Based on the MSD data from the two replica simulations of the immobilised polymer at 500 K, both $D_{\rm O_2}$ and $D_{\rm H_2O}$ are approximately $0.3\times10^{-8}~\rm cm^2~\rm s^{-1}$, which is around four orders of magnitude slower than the 500 K simulations of the mobile, amorphous phase, and an order of magnitude lower than the 300 K simulations. Visual inspection of the trajectories of the permeant molecules in the immobilised polymer revealed that the water and oxygen molecules are mainly trapped within gaps in the polymer and only a few molecules experience an occasional "jump" to a different location. This can be seen in plots of the root mean squared displacement (RMSD), shown in Figure 3.11. The green plot shows the RMSD of a water molecule which is confined in a small gap within the polymer and remains there throughout the entire simulation. The molecule represented by the blue plot is also trapped for the duration of the simulation, al-

Polymer	M	Permeant	Source	T (K)	$D (\times 10^{-8} \text{ cm}^2 \text{ s}^{-1})$
PHB	10	$\mathrm{H_{2}O}$	Present	300	1.1 ± 0.1
PHB	20	H_2O	Present	300	2.2 ± 0.8
PHB	-	H_2O	Expt [18]	298	1.88 – 5.92
PHB	-	H_2O	Expt [19]	309.5	0.87 - 8.04
PHB	10	O_2	Present	300	6.1 ± 1.3
PHB	20	O_2	Present	300	5.5 ± 1.8
PHB	-	O_2	Expt [18]	298	4.62 - 9.86
PHB	10	$\mathrm{H_2O}$	Present	500	2370 ± 230
PHB	20	H_2O	Present	500	2310 ± 190
PHB	10	O_2	Present	500	3760 ± 250
PHB	20	O_2	Present	500	2460 ± 230
PHV	10	$\mathrm{H_{2}O}$	Present	500	2040 ± 320
PHV	10	O_2	Present	500	6320 ± 610

Table 3.8: Diffusion coefficients, D, computed from MSDs, and experimental results from literature [18, 19]. The uncertainty in D is the standard deviation of two repeat simulations at 500 K or three repeat simulations at 300 K.

though in a slightly larger region. The orange plot shows another water molecule that was able to "jump" to a new location in the polymer matrix, but only after 150 ns of being confined. These simulations allowed us to determine that the kinetic energy of the diffusing molecules alone is insufficient to overcome the energy barrier associated with "jumping" to new gaps in the immobile polymer matrix. Thus, polymer chain mobility plays a significant role in the diffusion of oxygen and water. The diffusion of small molecules through polymers via a "hopping" mechanism has been reported in the literature. Takeuchi modelled permeant diffusion through a glassy polymer well below its $T_{\rm g}$ and found that while many permeant molecules remained trapped in cages within the matrix, localised chain motions occasionally created transient channels and vacant cages [129]. These pathways allowed permeants to hop through the material without encountering significant energy barriers. A similar permeation mechanism for small molecules has also been described by Müller-Plathe and Hoffmann [130, 131].

Figure 3.12 shows the MSD of oxygen and water at 300 K and 500 K in PHB systems. For both temperatures, it can be seen that oxygen diffuses through PHB at a significantly higher rate than water. This trend is in agreement with experimental results that found the diffusion coefficients of oxygen to be higher than water [18]. This difference could be due to differences in molecular size, polarity,

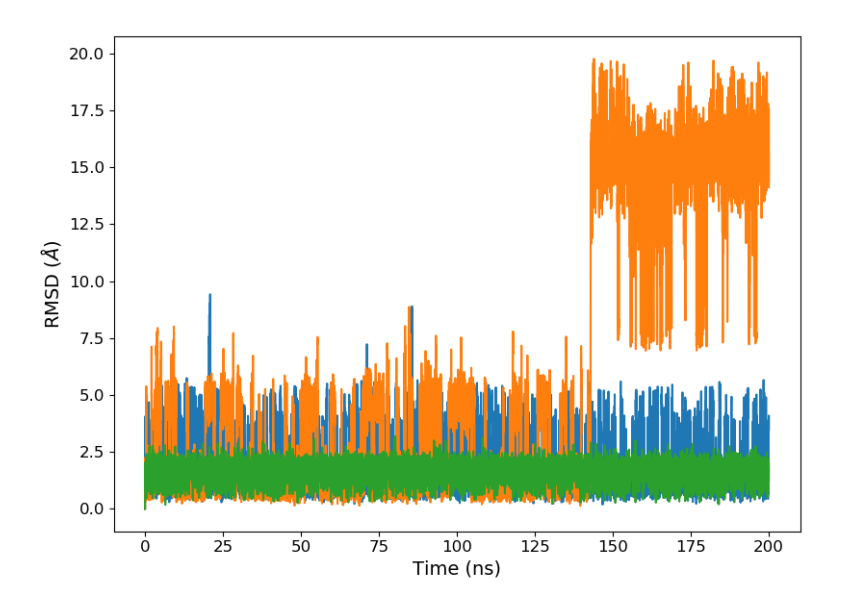


Figure 3.11: RMSDs of three water molecules within the immobilised PHB matrix.

and interactions with the polymer matrix. To understand more about the interactions with the polymer matrix, radial distribution functions (RDFs) for water and oxygen with ester groups and chain ends are shown in Figure 3.13.

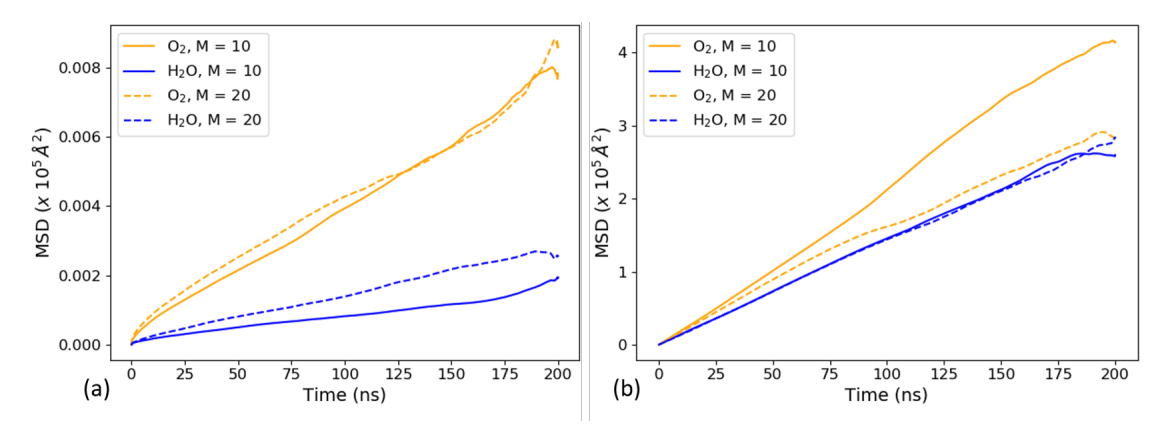


Figure 3.12: MSDs of oxygen (orange) and water (blue) in amorphous PHB at (a) 300 K and (b) 500 K. Solid lines represent the M=10 polymer systems and dashed lines represent the M=20 systems.

Figure 3.13(a) shows a stark difference in the RDFs for water and oxygen with the carbonyl ester group, with water exhibiting a strong peak at ≈ 2 Å. The polar water molecules tend to form hydrogen bonds with the carbonyl oxygen of the ester group in the PHB chains, hindering their passage through the matrix. In

contrast, the non-polar oxygen encounters fewer barriers and weaker interactions than water, allowing it to move more freely through the PHB matrix.

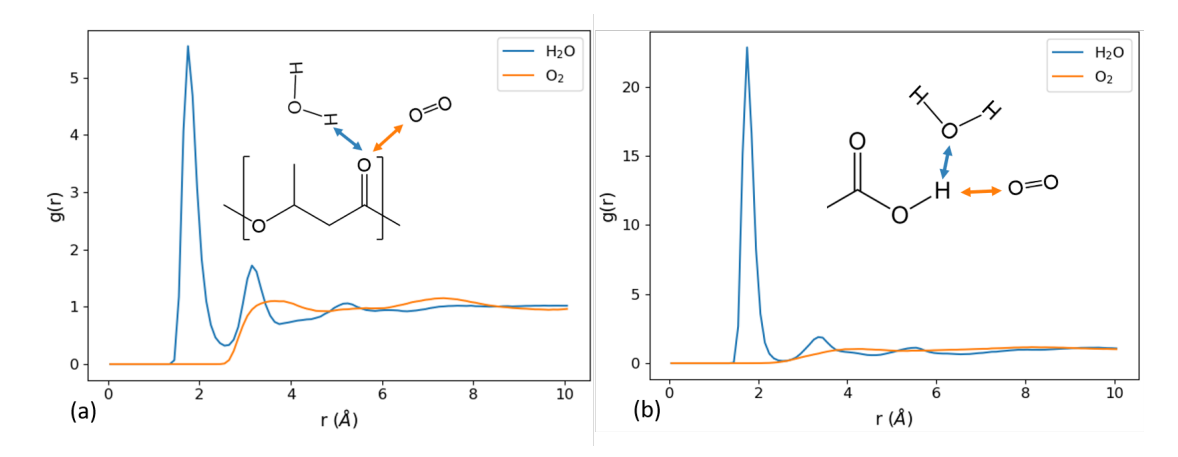


Figure 3.13: RDFs for permeant molecules around (a) the ester groups and (b) chain ends of the polymer molecules in the PHB M=10 system at T=300 K.

At 500 K, the oxygen diffuses faster in the more mobile M=10 system than in the M=20 system, as expected. At 300 K, the effect of the polymer chain length on diffusion is less clear and the polymer chain length has little effect on oxygen diffusion. For water at 500 K, there is little difference between the M=10 and M=20 systems but, surprisingly, at 300 K the diffusion of water is slightly faster for the M=20 system. However, this can be explained by the higher concentration of polar chain ends in the M=10 system, which interact with the polar water molecules and slow their diffusion. The strength of the interaction with the chain ends can be seen by comparing the peak height in the RDF for water with chain ends in Figure 3.13(b) to water with the ester linking groups in Figure 3.13(a), showing a much stronger association of water with the chain ends.

Our diffusion coefficients for water and oxygen in the M=20 systems at 300 K are within experimental ranges as shown in Table 3.8. For oxygen, our calculated value of $D_{\rm O_2}=5.45\times 10^{-8}~{\rm cm^2~s^{-1}}$ is in line with the experimental measurements by Follain et~al., who reported $D_{\rm O_2}=4.62-9.86\times 10^{-8}~{\rm cm^2~s^{-1}}$ at 298 K, depending on sample preparation [18]. For water, our calculated value of $D_{\rm H_2O}=2.23\times 10^{-8}~{\rm cm^2~s^{-1}}$ is also within the experimental range of $1.88-5.92\times 10^{-8}~{\rm cm^2~s^{-1}}$ at 298 K reported by Follain et~al. [18] and $0.87-8.04\times 10^{-8}~{\rm cm^2~s^{-1}}$ at 309.5 K reported by Yoon et~al. [19]. However, in both experimental studies, the diffusion experiments were carried out at temperatures higher than the experimental glass transition temperature for PHB and the polymer films used are semi-crystalline, with degree of crystallinity ranging from 41-48%, meaning that our simulated values cannot be directly compared to these

experimental measurements. It is generally agreed that permeants cannot diffuse through crystal regions and we can hypothesise that the permeants diffuse in the amorphous regions around the crystals. The amorphous polymer in the vicinity of the crystalline regions has restricted mobility due to steric constraints imposed by the crystals, and is referred to as the rigid amorphous region [132]. Given that in the current simulation model, the systems at 300 K are below $T_{\rm g}$, it is possible that the glassy state is a reasonable representation of the rigid amorphous region through which permeant diffusion takes place.

Finally, we compare diffusion in PHB with PHV, and MSD plots are shown in Figure 3.14. Water diffusion is similar through PHB and PHV, consistent with the above findings that water displacement is primarily governed by interactions with the polar groups in the polymer chains and is largely unaffected by the presence of the side chain in PHV. In contrast, oxygen diffusion is approximately twice as fast in PHV as in PHB. Since oxygen molecules do not interact with the polymer ester groups, they are able to diffuse more readily within the less dense PHV matrix. It should be noted that there is a scarcity of experimental data on pure PHV available in the literature. Overall, these findings suggest that although PHB and PHV exhibit similar water barrier properties, pure PHB provides a more effective barrier against oxygen diffusion.

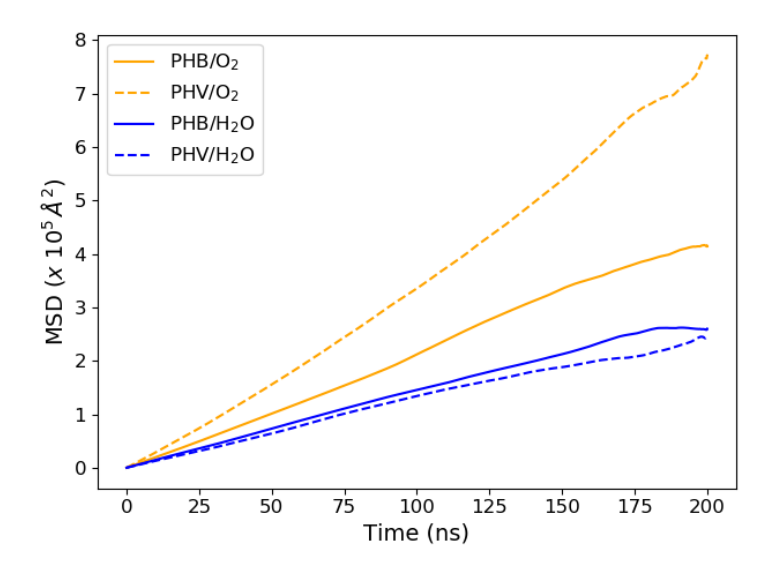


Figure 3.14: MSDs of permeants in amorphous PHB and PHV. Simulations were carried out at 500K and results were averaged over two repeats.

3.4 Summary and Conclusions

The transition towards sustainable materials is critical for addressing environmental challenges associated with conventional plastic packaging and PHAs represent a promising class of biodegradable polymers. MD simulations offer a powerful tool for probing the structural and dynamic properties of such materials at the molecular level. This study set out to create an effective MD force field for crystal and amorphous PHAs which can be used to investigate gas barrier properties.

Initially, a modified GAFF force field was implemented for PHB. The GAFF parameters were slightly modified to remove instabilities associated with the chain ends. Partial charges were adjusted to enable the force field to be easily applied to PHB, PHV and PHVB copolymers. The force field's ability to reproduce structure and dynamical properties of PHB, PHV and copolymers in crystal, glassy and melt states was tested.

For PHB and PHV crystals, the density and lattice parameters of both systems agreed well with experimental values. Structural analysis of the PHB backbone included torsional angles, which match those given in several experimental papers. The cohesive and surface energies of PHB were higher than those of PHV, which is consistent with PHB's higher melting temperature. In simulations, the melting temperatures of crystals were higher than experimental values; however, the observed trend of PHV exhibiting a lower melting temperature compared to PHB aligns with experimental data. Surface energies were also significantly higher than those reported in experimental papers, which could be attributed to the semi-crystalline nature of experimental samples, compared to the perfect crystal structures in the simulations.

For the amorphous PHA systems simulated in this work, densities were in good agreement with both simulation and experimental literature data. The glass transition temperatures were in line with previous simulation results; however, they were approximately 100 K higher than the experimental values, as well as higher than the crystal melting temperatures. The decrease in $T_{\rm g}$ observed on increasing HV content is consistent with trends observed in literature. The Hildebrand solubility parameters were consistent with the available literature data, with the longer chain systems approximately converging to the experimental value.

The diffusion coefficients of oxygen and water molecules through amorphous PHB were in good agreement with experimental values, with water diffusion being slower than oxygen diffusion due to hydrogen bonding interactions between water and PHB, which hinders diffusion. While the diffusion coefficient of water was comparable in PHB and PHV, that of oxygen was roughly double in PHV, due

to its lower density, rendering it a less effective oxygen barrier.

In summary, we have presented a force field that is versatile enough to provide insight into structural and barrier properties of PHAs, that can aid design of PHA-based plastics for applications such as sustainable food packaging.

Chapter 4

Water and Oxygen Diffusion in Crystalline and Filled Amorphous Polyhydroxyalkanoates

Abstract

This chapter presents molecular dynamics (MD) simulations investigating diffusion in crystalline and graphene-filled polyhydroxybutyrate (PHB) systems, to improve understanding of gas transport in compostable food packaging materials. Crystalline PHB models were constructed using both infinitely bonded and finite chain configurations. Simulations of oxygen and water in these crystalline systems revealed no significant diffusion in the timescale studied, indicating that molecular transport through crystalline domains is negligible compared to that through the mobile amorphous regions. Oxygen exhibited larger (but finite) displacements than water in the finite chain crystal, while water remained constrained by electrostatic interactions with the polymer matrix.

The influence of a graphite surface on water and oxygen diffusion in amorphous PHB has been investigated. The densification and alignment of polymer chains at the interface led to reduced polymer mobility relative to the bulk. In the graphite-filled system, the diffusion of water was 31% slower than that in bulk PHB. Oxygen diffusion was affected even more, showing a 47% decrease in diffusion coefficient when graphite was present. This was a result of (a) restricted polymer chain dynamics creating fewer channels for the permeant to migrate through and (b) interfacial accumulation of permeant molecules. Oxygen preferentially adsorbed near the surface due to van der Waals attractions,

while water remained on the outer side of the polymer phase where electrostatic interactions dominated. These findings demonstrate how crystalline structure and filler-induced interfacial ordering inhibit permeant mobility and should be considered when designing PHB-based films.

4.1 Introduction

Effective barrier performance is a key requirement in the design of polymer films for food packaging, where the ingress of oxygen or water vapour can significantly reduce product shelf life and quality. To optimise these materials, it is necessary to understand how gas molecules move through the complex semi-crystalline structure of the polymer matrix. MD simulations offer a powerful tool for probing gas diffusion at the molecular level, providing detailed insights into the interactions between permeant molecules and polymer chains, as well as the influence of local structure on diffusion behaviour. A validated MD model for polyhydroxyalkanoates (PHAs) has been previously developed to capture both the structural and dynamic behaviour of amorphous and crystalline phases [133]. This model was successfully used to investigate the diffusion of small molecules through amorphous PHA matrices, providing insight into the differences between oxygen and water transport in PHB and polyhydroxyvalerate (PHV). However, semicrystalline polymers such as PHB contain both amorphous and crystalline domains and so a complete understanding of their barrier properties requires characterising diffusion behaviour in each phase independently. It is widely accepted that crystalline regions in polymers present a significant barrier to gas diffusion due to their dense molecular packing and restricted chain mobility. Studies on synthetic polymers, including polyethylene and polyethylene terephthalate, have demonstrated that gas transport through crystalline domains is negligible compared to amorphous regions [85, 134, 135]. However, this assumption has not been rigorously tested for PHAs. The extent to which the crystalline domains of PHAs impede molecular transport remains unclear and a quantitative understanding is essential for accurate modelling of their barrier performance in practical applications such as food packaging.

The use of nanoscale filler particles is a widely studied strategy for enhancing the barrier properties of polymeric materials by (a) increasing crystallinity and (b) providing a physical barrier to diffusion. Additives such as layered silicates, metal oxides and carbon-based nanomaterials have been shown to improve mechanical, thermal and barrier properties of PHA composites [3, 49, 60]. Graphene, in particular, has emerged as a promising nanofiller due to its exceptional mechanical strength, chemical stability and high aspect ratio [60]. MD simulations have

shown that graphene can significantly enhance the mechanical performance of polymer composites. For example, Yuan *et al.* demonstrated improved interfacial strength in graphene composites with polyethylene, polystyrene and polyurethane matrices [77], while Lu *et al.* found that the incorporation of graphene flakes into high-density polyethylene enhanced its elastic properties, with the magnitude of improvement depending on flake size [78].

While many studies have focused on the mechanical reinforcement of polymer/graphene composites, the impact of graphene on gas diffusion behaviour, particularly at the polymer/filler interface, remains largely unexplored. To the best of our knowledge, PHB/graphene composites have not previously been investigated using MD simulations. However, graphene has been successfully employed as a model filler in a number of polymer composite studies using the GAFF force field [76, 136], demonstrating its suitability for capturing both structural and interfacial effects at the atomistic scale. In this context, graphene provides a well-defined and computationally tractable model surface, which allows the behaviour of polymer chains in close proximity to a filler to be examined in detail.

In polymer nanocomposites, graphene typically interacts with the matrix via van der Waals (vdW) forces, leading to a distinct interfacial region with potentially different local structure and dynamics to the bulk. These interfacial zones may affect gas transport in complex ways by altering local free volume, disrupting polymer chain packing or restricting segmental mobility. However, the diffusion of gas molecules at or near filler surfaces is rarely investigated in detail using MD methods. Furthermore, while several studies suggest that nanofillers enhance barrier properties by increasing the tortuosity of diffusion pathways or introducing obstacles that disrupt molecular transport [60, 62], these effects are often evaluated experimentally on a macroscopic scale. Molecular-level insights into how filler surfaces interact with gas molecules and the surrounding polymer chains are critical for designing composites with optimised performance, especially in compostable polymers such as PHB, where compatibility and degradation behaviour are also important considerations.

This chapter presents MD simulations designed to address two key knowledge gaps: (1) quantifying the diffusion of oxygen and water in crystalline PHB systems, and (2) exploring how the presence of a graphene filler surface affects gas transport in amorphous PHB. Together, these simulations aim to clarify the roles of both ordered (crystalline) and heterogeneous (filler-containing) microstructures in governing gas barrier behaviour in PHA-based materials.

4.2 Methodology

The methodology for modelling the PHB α -crystal unit cell, amorphous PHB and the water and oxygen models used in the previous study as well as the current work can be found in ref [133]. Described in this section are the additional steps for simulating diffusion through the bulk crystals, with finite and infinite chains, and a PHB/graphite composite system. To characterise the permeant diffusion behaviour, time-averaged mean squared displacement (MSD) data was calculated using MDAnalysis [71] and the root mean squared displacement (RMSD) trajectory tool in VMD [72] was used to extract RMSDs of individual molecules. Further details on the calculation of MSDs and diffusion coefficients can be found in the previous study [133].

4.2.1 Crystalline Models

To set up the infinite chain crystal, five PHB unit cells were bonded together along the z dimension to create helical crystal chains, each 10 monomers long. The resulting box dimensions were x=5.72 Å, y=13.13 Å and z=29.61 Å. The system was energy minimised using the steepest descents algorithm and then simulated in the NPT ensemble at 200 K and 1 atm for 10 ns while changes in the lattice parameters and torsional angles were monitored. Anisotropic pressure control was used for all crystal simulations in the NPT ensemble, allowing each of the three box lengths to change independently. The temperature of 200 K was chosen for simulating the crystalline systems as the PHB crystal model was previously found to be unstable at higher temperatures [133]. Once the stability of the longer crystalline chains was confirmed, the system was replicated in the x and y axes to create a bulk crystalline slab which was four chains wide in both x and y directions, shown in Figure 4.1(a), where periodic boundary conditions mean that the crystal model is infinite in all dimensions. The replicated system had box dimensions of x=23.51 Å, y=25.63 Å and z=28.52 Å.

To set up the finite chain crystal, five crystal unit cells were bonded together in the z direction and one monomer in the middle of each of the two chains was removed and replaced with PHB chain ends. The resulting structure was energy minimised and simulated in the NPT ensemble at 200 K and 1 atm to monitor lattice parameters and torsional angles. As with the infinite chain crystal, the system was then replicated in the x and y axes, creating a bulk slab with the chain ends forming a plane across the crystal. Snapshots of this process can be found in Appendix B. The final structure is shown in Figure 4.1(b). The equilibration protocol was the same as that for the infinite chain crystal system, with energy minimisation and NPT run carried out. Density, lattice parameters and torsional angles from the NPT run are compared to those for the infinite chain

crystal in order to establish how the new chain ends affect the crystalline structure.

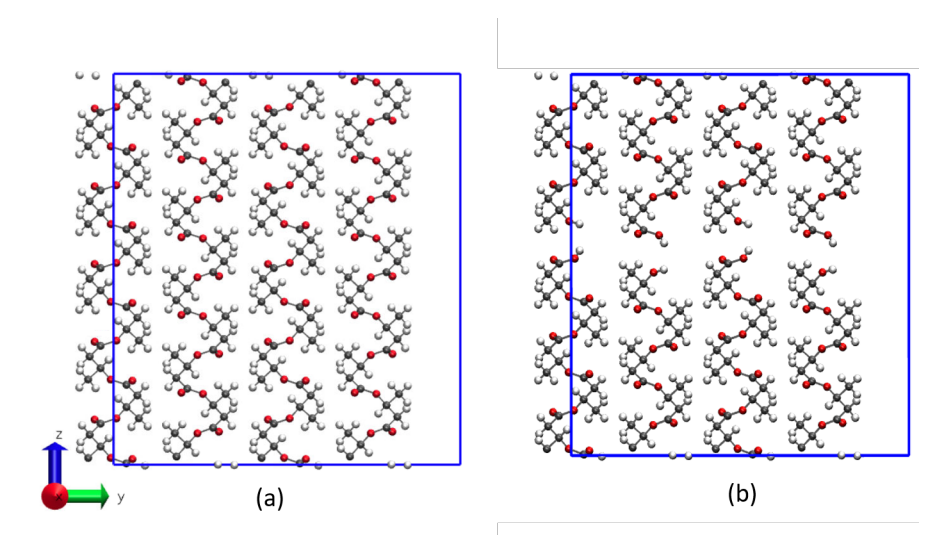


Figure 4.1: (a) Infinite chain bulk crystal model. (b) Finite chain bulk crystal model.

To simulate the diffusion of water and oxygen, the same procedure was used for both the finite chain and infinite chain crystal systems. The LAMMPS create_atoms command was used to insert 10 water or oxygen molecules at random positions and orientations in the crystal. An energy minimisation was carried out, followed by a 1 ns run in the NPT ensemble (200 K, 1 atm) to allow for any volume changes. To study the displacements of the permeants, an NVT simulation at 200 K was run for 100 ns. Two repeats of each system were simulated, using different starting configurations. The NVT ensemble was chosen for the production runs since it is generally faster to run compared to the NPT ensemble. Additionally, in their paper describing best practices for computing transport properties, Maginn et al. discourage the use of the NPT ensemble, stating the barostat can significantly affect the dynamics of the system [15].

4.2.2 Amorphous Model

In order to compare diffusion in crystalline versus amorphous PHB at the same temperature, diffusion of water and oxygen was also simulated in amorphous PHB at 200 K. The 300 K PHB/water and PHB/oxygen systems used in ref [133] were cooled to 200 K at a rate of 2.5×10^{10} K s⁻¹ and then thermally equilibrated in the NPT ensemble for 5 ns. The 200 K systems were then simulated in the NVT ensemble for 100 ns to track permeant diffusion. Two repeats of each system were simulated and MSD data was averaged.

4.2.3 Filled Amorphous PHB

To construct the graphite filler, a single graphene sheet was set up using the $Carbon\ Nanostructure\ Builder\ tool\ in\ VMD$. The sheet was approximately 40×40 Å in the x and y directions and periodic bonding was applied to the terminal carbon atoms along the x and y axes, effectively rendering the sheet infinite in those directions. Moltemplate [107] was then used to generate a LAMMPS data file containing all bonded and non-bonded force field parameters (see Section 3.2.1, Chapter 3 for further explanation of Moltemplate use). Graphene was modelled using GAFF, which has previously been demonstrated to be a suitable force field for modelling graphene sheets [76, 136, 137, 138, 139]. The carbon atoms were represented using the 'ca' atom type, which represents sp^2 -hybridised carbon in an aromatic environment [74]. No partial charges were assigned to the carbon atoms of graphene.

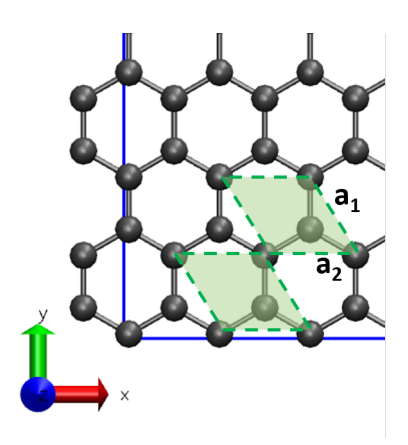


Figure 4.2: Graphene model with unit cells highlighted by green rhombus' with sides \mathbf{a}_1 and \mathbf{a}_2 .

Energy minimisation was performed, followed by a 100 ps NPT simulation at 500 K. The atoms maintained their hexagonal conformation throughout the run, indicating that the model was stable with the chosen force field. After energy minimisation and equilibration, the repeating unit of the sheet was compared to the graphene unit cell parameters reported in the literature. The two unit cell vectors, \mathbf{a}_1 and \mathbf{a}_2 in Figure 4.2, measured 2.45 \pm 0.04 Å, which is consistent with the known crystal lattice of graphene (2.46 Å [140]). Once the stability of a single graphene sheet was confirmed, three layers were stacked using the LAMMPS replicate command to create a multilayered graphite model, which better represents a filler particle. The middle sheet was shifted slightly in the x and y directions to mimic AB stacking, where half of the carbon atoms in one layer lie directly above the centres of hexagons in the adjacent layer, shown in Figure 4.3. This configuration optimises the short-range attraction between atoms in neighbouring

layers, producing a stable graphite structure [141]. The interlayer distance was set to 3.3 Å, the known equilibrium spacing for graphite [142]. At this spacing, three graphene layers were sufficient to prevent the polymer from interacting with its periodic image on the opposite side of the graphite, as this distance exceeded the 10 Å cutoff used for the Lennard-Jones potential. Although the polymer will still experience some residual long-range electrostatic interaction across the graphite layer, these are not expected to be significant because the partial charges in the system are relatively small.

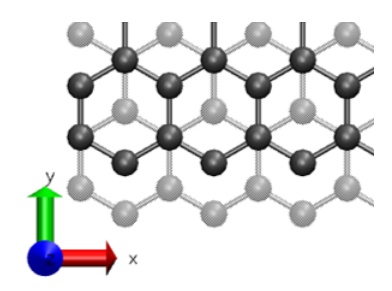


Figure 4.3: AB stacking in multilayer graphite model.

System Instability

The simulation box was expanded in the z dimension to accommodate the amorphous polymer chains. As an initial test, a single PHB chain was added to the graphite box, with vdW parameters computed using Lorentz-Berthelot mixing rules. To reduce computational cost, the graphite atoms were kept immobile by not applying a thermostat, eliminating the need to compute pairwise interactions between them at every timestep. This approach has been previously used when graphene-graphene self-interactions are not the focus of the study [124, 143]. After energy minimisation, a 100 ps NVT simulation was conducted, keeping the polymer thermostatted at 500 K to simulate its melt phase while the graphite remained effectively 'frozen.' Upon visualising the trajectory, the system exhibited instability due to the 'flying ice cube syndrome,' a rare artifact in MD simulations where energy is improperly distributed, violating the equipartition theorem, which states that energy should be evenly distributed among all degrees of freedom at thermal equilibrium [144]. The exact causes of this phenomenon are not fully understood, but it is known to be associated with certain thermostats and can lead to unphysical structural and dynamic behaviour. In this case, the PHB chain rapidly drifted away from the graphite. To counteract this, the fix recenter command was used to constrain the polymer centre of mass. However, this led to the PHB chain freezing over and eventually become completely immobile, despite the LAMMPS thermodynamic output showing no drop in temperature or kinetic energy. It was determined that the flying ice cube artifact resulted from the immobility of the graphite atoms, as the issue did not occur when a thermostat was applied to them. Consequently, despite the additional computational cost, it was decided to allow the carbon atoms in the three graphene sheets to move during the simulations.

Simulation Protocol

50 PHB chains were added to the graphite system and equilibrated for 30 ns in the NPT ensemble using anisotropic pressure control, following the protocol outlined in ref [133]. The system was periodic in all three directions to create a film of amorphous PHB confined between the graphite. To prevent system drift from artificially inflating MSD values, the fix spring command in LAMMPS was used to apply light tethering forces to the centre of mass of both the polymer and graphite atom groups, keeping each group close to its initial centre of mass position. Following polymer equilibration, 10 oxygen or water molecules were inserted into the system and the volume was re-equilibrated for 1 ns at 500 K and 1 atm, allowing the box volume to adjust to accommodate the extra molecules. The production run consisted of a 100 ns NVT simulation at 500 K, again employing the centre of mass constraints. Three repeat simulations were performed for each permeant using different initial polymer configurations prior to permeant insertion. Diffusion coefficients were determined from the MSD data, as described in ref [133]. Python scripts were used to characterise the behaviour of the permeant molecules by analysing their positions relative to the graphite.

4.3 Results and Discussion

This section begins by presenting the structural properties of the finite chain PHB crystal and comparing them with those of the infinite chain model. The diffusion behaviour of water and oxygen in both crystal systems is then examined. Finally, results from diffusion simulations in the amorphous PHB/graphite composite are discussed.

4.3.1 Finite Chain Crystal Properties

On visualising the simulation trajectories in VMD, it was clear to see that the finite chain crystal was stable using the current force field and simulation methods. Despite the fact that the chains were now free to move into a more disordered amorphous configuration, only the free ends moved significantly during the simulations, with the bulk of the crystal remaining in the helical structure. This is observed through analysis of the crystal density and lattice parameters, as well as measuring the backbone torsional angles, and comparing them to those of the

infinite chain crystal. The density and lattice parameters are given in Table 4.1 and torsional angles are plotted in Figure 4.4. All results are averaged over a 10 ns NPT simulation at 200 K and 1 atm. As seen in Table 4.1, the a, b and c lattice parameters (referring the the x, y and z box lengths) and density of the finite chain system are in good agreement with those for the infinitely bonded crystal. Although it has a slightly higher cell volume, the infinite chain system is marginally more dense due to its larger mass. The presence of the chain ends allows for greater rotation of the backbone, creating additional small peaks in the ω , ϕ and ψ plots (Figure 4.4). No extra peaks are present in the plot of τ , indicating this angle is largely unaffected by the chain ends. Despite the extra peaks in the finite chain system, the positions of the tallest peak for all four angles are the same as those of the infinite chain crystal.

	a (Å)	b (Å)	c (Å)	$\rho \; (\mathrm{g} \; \mathrm{cm}^{-3})$
Finite chains	5.88 ± 0.09	12.79 ± 0.17	28.26 ± 0.33	1.24 ± 0.02
Infinite chains	5.88 ± 0.08	12.81 ± 0.15	30.25 ± 0.33	1.25 ± 0.02

Table 4.1: Comparison of density and lattice parameters in crystalline PHB models. Data was sampled every picosecond during a 10 ns NPT run at 200 K and 1 atm. Errors given are standard deviations of the measured data.

4.3.2 Diffusion in Crystalline Models

The total MSDs of oxygen and water in the crystalline PHB systems are shown in Figures 4.5 and 4.6. Both permeants are able to move much further in the finite chain crystal than in the infinite chain. The presence of chain ends in the finite system introduces additional free volume and local disruption of the crystal lattice, which in turn permits greater segmental mobility of the polymer chains. These effects create transient voids or channels that can facilitate the movement of small molecules. As observed in the amorphous systems, oxygen consistently displaces more rapidly than water in both crystalline models, likely due to its smaller size and non-polar nature. To gain directional insight into the diffusion behaviour, the MSDs were decomposed into the x, y and z components, as shown in Figures 4.5 and 4.6 for infinite chain and finite chain crystals, respectively. In the infinite chain crystal, diffusion is extremely limited, with little or no displacement observed in any of the three crystal axes. This lack of movement reflects the rigidity and tight packing of the helical chains when no chain ends are present. In contrast, the finite chain model introduces chain ends, enabling limited but measurable permeant movement in certain crystal axes, as seen in Figure 4.6.

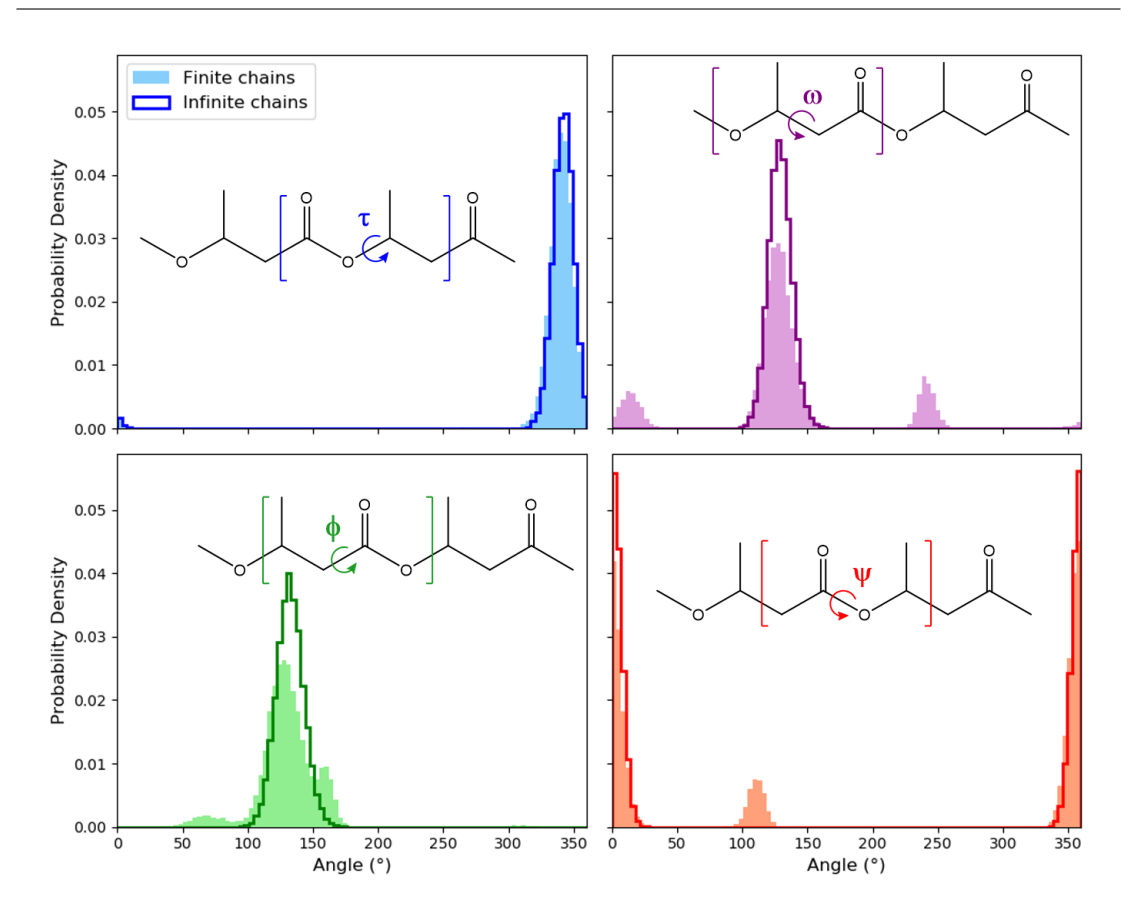


Figure 4.4: Torsional angles in the PHB backbone for finite and infinite chain crystalline systems. Averaged over 10 ns NPT run at 200 K and 1 atm.

To further characterise the nature of diffusion events, the RMSD of individual molecules between sampled configurations were calculated, and the minimum, maximum and average displacements are summarised in Table 4.2. The oxygen molecules show a pronounced increase in RMSD in the finite chain model, with an average displacement per time interval of 6.0 Å compared to just 1.8 Å in the infinite chain model. Moreover, the maximum displacement in the finite chain system was nearly twice that in the infinite one. For water, the differences are less marked; average displacements were 2.7 Å and 1.8 Å in the finite and infinite models, respectively. These findings reinforce the idea that oxygen transport is more sensitive to polymer chain structure, while water diffusion is more constrained by its stronger interactions with polar groups.

As seen in Figure 4.5, the MSD curves for permeants in the infinite chain system deviate from linearity, indicating that the permeants do not reach the diffusive regime as described by Einstein's relation and hence a linear fit to extract a diffusion coefficient is not appropriate. Instead, by examining the final MSD

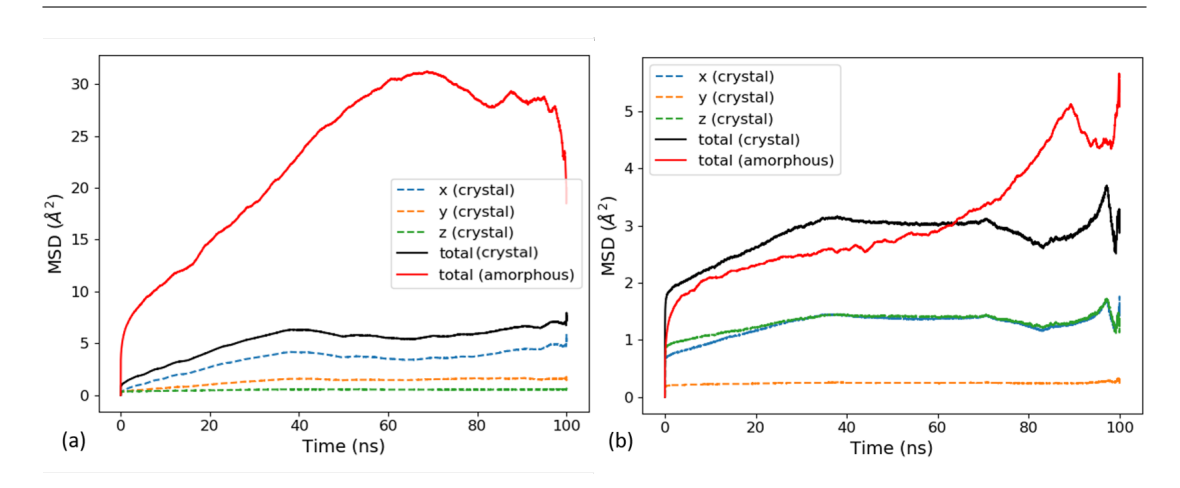


Figure 4.5: Diffusion of (a) oxygen and (b) water molecules in infinite chain crystals, showing total MSD and breakdown into each axis. Permeant diffusion in the amorphous polymer at 200 K is also plotted. Data has been averaged over two repeat simulations.

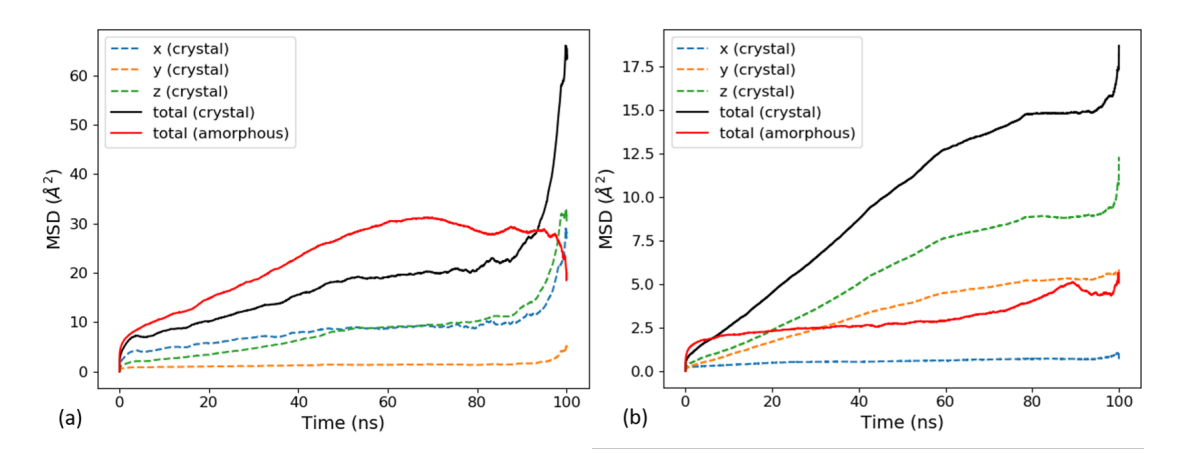


Figure 4.6: Diffusion of (a) oxygen and (b) water molecules in finite chain crystals, showing total MSD and breakdown into each axis. Permeant diffusion in the amorphous polymer at 200 K is also plotted. Data has been averaged over two repeat simulations.

values, excluding the anomalous region beyond 95 ns caused by poor statistics, the water molecules show a total MSD of only around 3 $Å^2$, while oxygen reaches 6 $Å^2$. On analysing the diffusion of permeants in amorphous PHB at 200 K, the final MSD values are similar to those in the crystalline systems, with the exception of oxygen in the infinite chain crystal, where the final MSD in the amorphous system is 5-6 times higher than in the crystal. These values are significantly lower than those for amorphous PHB systems at 300 K, where water and oxygen reach average MSDs of approximately 200 $Å^2$ and 800 $Å^2$, respectively [133], despite

		F	RMSD	(Å)
		Min	Max	Average
	Finite	0.3	9.3	6.0
\mathbf{O}_2	Infinite	0.1	4.3	1.8
пО	Finite	0.2	4.5	2.7
$\mathbf{H}_2\mathbf{O}$	Infinite	0.1	3.6	1.8

Table 4.2: Minimum, maximum and average RMSD of the permeant molecules over the 100 ns NVT simulations. Values are averaged over 10 molecules.

still being below the polymer glass transition temperature (T_g) . These findings suggest that at 200 K, as well as the reduced kinetic energy of the permeants, the mobility of the amorphous PHB chains is restricted to such an extent that permeant molecules remain trapped in cages within the matrix, with little or no local chain movement to create new channels.

Overall, even with the enhanced mobility introduced by chain ends in the finite chain crystal, the diffusion of oxygen and water in crystalline PHB is so small that it cannot be quantified by a diffusion coefficient in these 100 ns duration simulations. The results support the hypothesis that crystalline regions in polymers effectively act as impermeable domains. In crystalline systems, polymer chains are tightly packed into ordered, dense structures with limited free volume and minimal segmental motion. This rigidity severely restricts the ability of small molecules to navigate through the lattice. In contrast, amorphous regions at temperatures close to or above $T_{\rm g}$ are disordered and contain greater free volume, dynamic chain fluctuations and transient cavities, all of which facilitate the passage of permeant molecules. Therefore, the dominant pathway for gas and water diffusion in semi-crystalline PHAs is through the amorphous phase and the presence and distribution of crystalline domains significantly hinders overall permeability.

4.3.3 Effect of Graphene Surface on Diffusion

In experimental systems, filler particles incorporated into polymer matrices can range up to several microns in diameter, which is many orders of magnitude larger than what can be realistically captured in atomistic MD simulations. In the present model, the graphite additive is represented as a layered sheet ~ 10 Å thick in the z direction, with the surrounding amorphous PHB region extending ~ 40 Å in the same direction. Rather than modelling a complete filler particle, the approach taken here is to represent a filler surface in direct contact with the polymer. This allows the interfacial region to be probed at atomistic resolution, enabling characterisation of the molecular-level interactions that govern polymer-

filler interfacial behaviour.

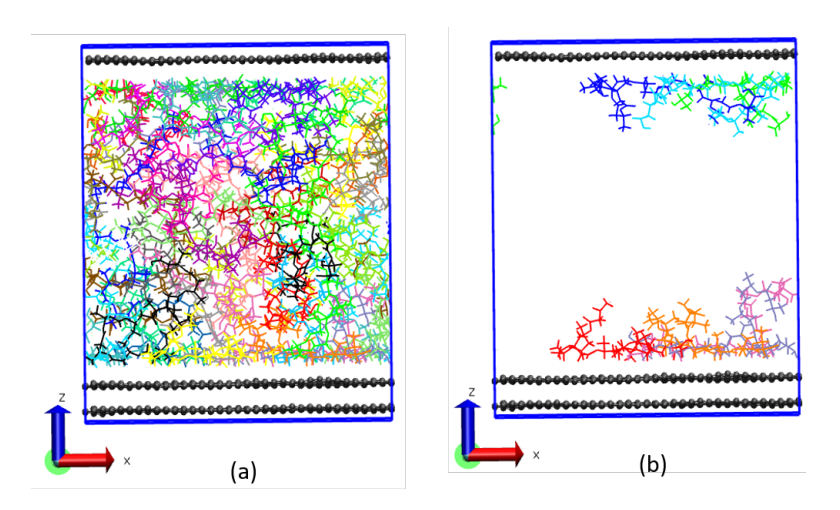


Figure 4.7: PHB/graphite system showing (a) formation of dense polymer layers and (b) elongation of polymer chains at the surface.

The presence of the graphite surface induces the formation of dense layers of polymer chains adjacent to the interface. In these interfacial regions, polymer chains tend to align and extend parallel to the surface, as shown in Figure 4.7(b). This behaviour arises from graphene's planar geometry, which encourages chains in close proximity to adopt extended conformations and pack more tightly compared to the bulk. As a result, a more ordered and densely packed polymer layer forms at the interface. McKechnie et al. observed higher radius of gyration and chain end-end distance for polymers next to a graphite surface compared to that in the bulk [124]. Through analysis of the chain orientation, they also found that the chains stretch parallel to the surface and flatten in the z direction. Similar behaviour has been reported for polystyrene chains at a gold surface [145]. Beyond this interfacial layer, a region of reduced density is observed, reflecting a compensation effect due to the local densification at the surface. The oscillations in polymer density as a function of distance from the graphite sheet, shown in Figure 4.8(a), indicate the presence of short-range ordering. The high density peaks become smaller further from the surface until density plateaus at approximately its bulk amorphous density of 1.05 g cm⁻³ in the centre of the box. This layering behaviour is typical of polymers at a surface [65, 124].

By decomposing the polymer density profile into contributions from carbon, hydrogen and oxygen atoms, a distinctive double peak was observed in the oxygen distribution near the graphite surface (Figure 4.8(b)). To investigate this feature, the two types of oxygen atoms in the PHB backbone were examined separately: the carbonyl oxygen (double bonded to carbon) and the ester oxygen (part of the

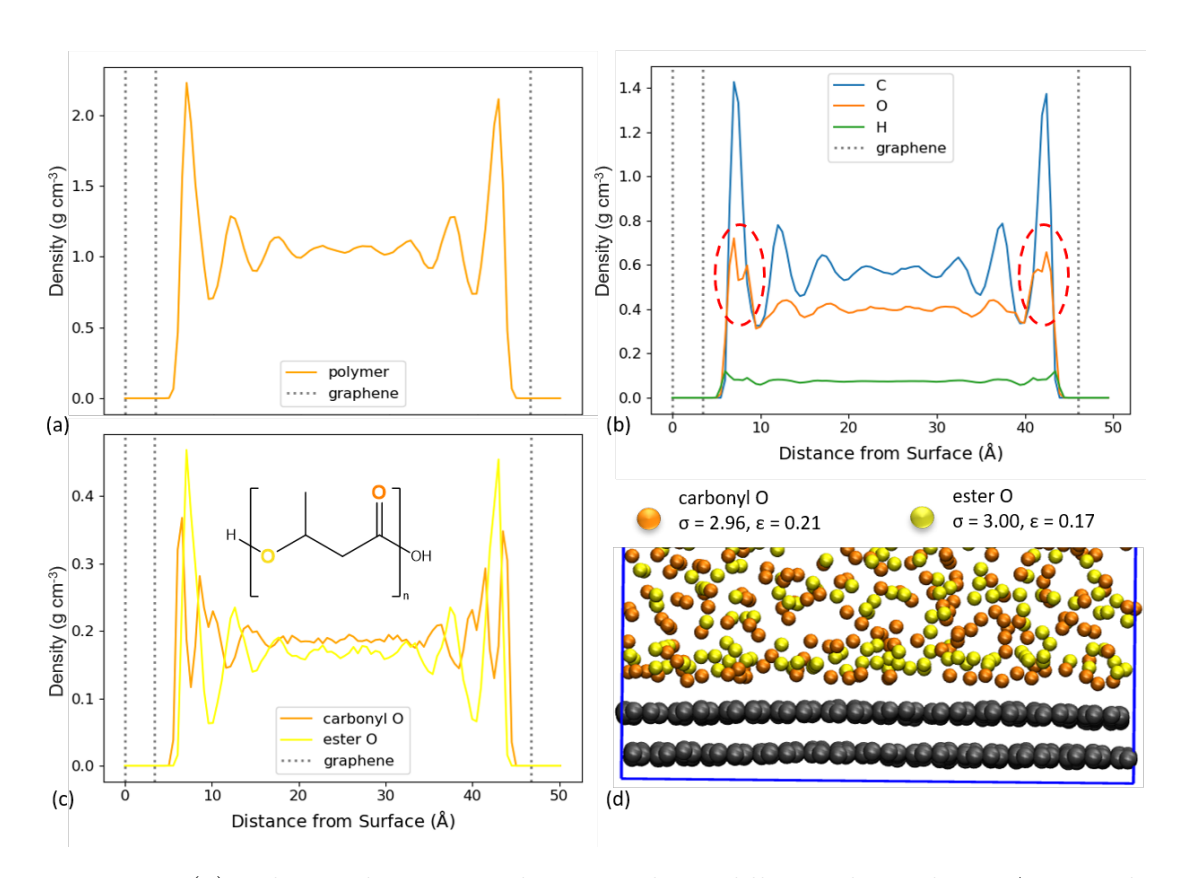


Figure 4.8: (a) Polymer density in relation to the middle graphene sheet. Averaged over 10 ns NVT simulation at 500 K. (b) Polymer density broken down into carbon, oxygen and hydrogen density. (c) Density profiles of the carbonyl and ester oxygen atoms. (d) Snapshot showing proximity of carbonyl and ester oxygen atoms to the graphite surface. σ is given in Å and ε in kcal mol⁻¹.

C-O-C ester linkage), hereafter referred to as carbonyl O and ester O, respectively. The chain ends were not included in this analysis due to their low concentration in the polymer matrix. As shown in Figure 4.8(c), the carbonyl O atoms exhibit a preference for positioning closer to the graphite surface than the ester O atoms. This spatial arrangement is also evident in the VMD snapshot in Figure 4.8(d), where polymer chains near the surface appear oriented such that the carbonyl O atoms point outward toward the surface, while the ester O atoms lie slightly further back. This preferential alignment can be rationalised by considering the vdW parameters of the two oxygen types. The carbonyl O atoms have a larger well depth ($\epsilon = 0.21$ kcal mol⁻¹) and a slightly smaller vdW radius ($\sigma = 2.96$ Å) compared to the ester O atoms ($\epsilon = 0.17$ kcal mol⁻¹, $\sigma = 3.00$ Å). These properties result in stronger attractive interactions and allow the carbonyl O atoms to

approach the surface more closely, contributing to the observed double peak in the oxygen density profile. Another factor contributing to the ester Os being further from the graphite is the steric hinderance caused by the proximity of the methyl group on the polymer chain. As seen in the inset in Figure 4.8(c), the ester O is closer to the side group than the carbonyl O which could create more restricted freedom in the orientation of the ester group, preventing it from aligning closer to the graphite.

To evaluate how the presence of graphite affects polymer mobility, the MSD of PHB chains in the composite system was compared to that in a bulk amorphous system without graphite. As shown in Figure 4.9, the polymer dynamics are noticeably slower in the presence of the filler. While chains further from the interface will likely remain largely unaffected, the reduced mobility of polymer segments within the dense interfacial layer contributes to a lower average MSD for the system. Similar effects have been observed in other polymer nanocomposites; for instance, Li et al. reported that polymer chains exhibited slower dynamics near filler surfaces in polyethylene/graphene systems [79].

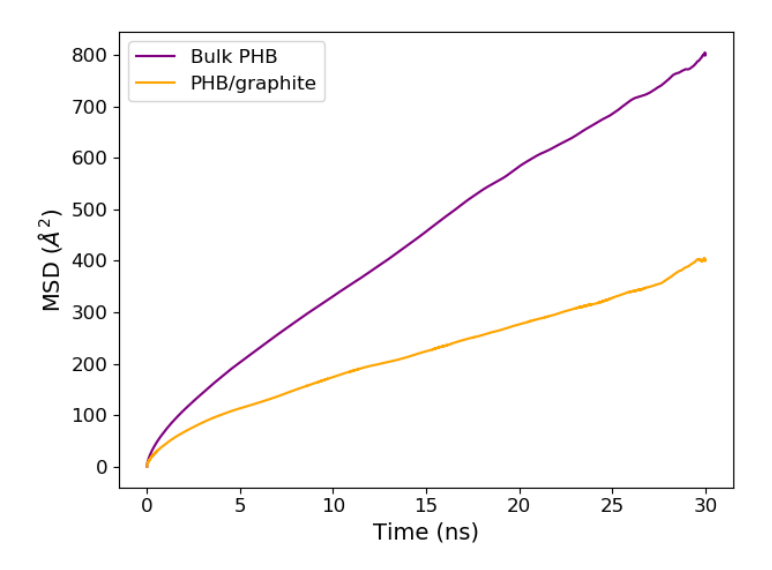


Figure 4.9: MSD of PHB in bulk system and graphite system during NPT simulation at 500 K and 1 atm.

Figure 4.10 shows the MSD of water molecules broken down into the x, y and z contributions. Due to the graphite creating finite distance for displacement in the z direction, the diffusion is primarily 2D, as can be seen from the flat z line in Figure 4.10. As a result of this, the diffusion coefficients were computed using a 2D model rather than 3D. While there is still some movement in the z direction

between the graphite and its periodic image at the top of the box, when compared to the displacements in the other two axes, it can be assumed that the diffusion taking place is 2D.

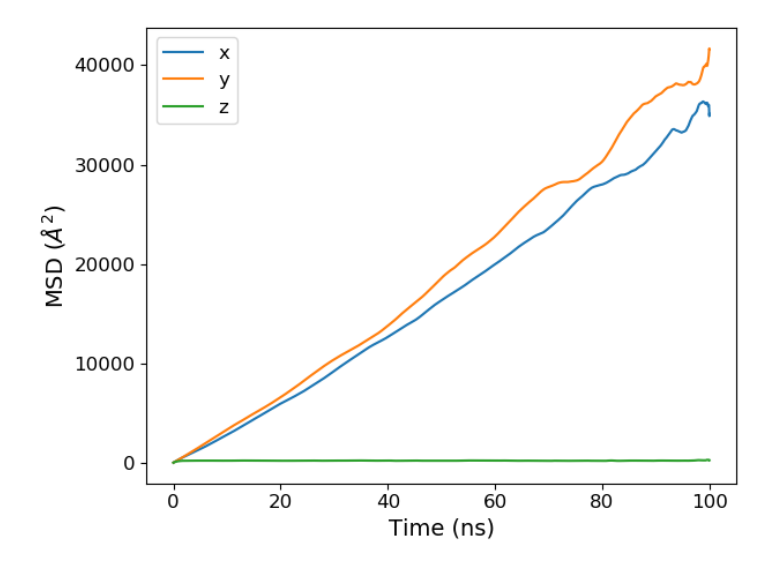


Figure 4.10: x, y and z MSD components of water molecules in PHB/graphite system.

The MSD, denoted S(t), is calculated using Equation 4.1:

$$S(t) = \left\langle \frac{1}{N} \sum_{i=1}^{N} |r_i(t+t_0) - r_i(t_0)|^2 \right\rangle_{t_0}$$
(4.1)

where N is the number of diffusing molecules of the target species, $r_i(t)$ represents the coordinates of the particle at time t and the angled brackets denote averaging over reference positions using multiple time origins t_0 . From this, the diffusion coefficient D is then obtained using Equation 4.2:

$$D = \frac{1}{2 \times \delta} \frac{d}{dt} S(t) \tag{4.2}$$

where δ refers to the dimensionality of the system. For diffusion in the bulk amorphous system, $\delta=3$ but for the graphite system, $\delta=2$. Therefore, when calculating diffusion coefficients in the current PHB/graphite system, the slope of the MSD line is divided by 4, rather than 6, as the diffusion in z is negligible compared to diffusion in x and y. Diffusion coefficients of the water and oxygen are given in Table 4.3, along with those from bulk PHB simulations for comparison [133]. Oxygen diffuses faster in both systems, although the difference is less significant in the graphite system. Both $D_{\rm H_2O}$ and $D_{\rm O_2}$ are lower in the graphite

system, which can be explained by the less mobile polymer chains creating fewer cavities for the permeants to diffuse through.

	D (×10 ⁻⁵	$(cm^2 s^{-1})$
	Water	Oxygen
PHB [133]	2.37 ± 0.23	3.76 ± 0.25
PHB/graphite	1.63 ± 0.36	1.99 ± 0.22

Table 4.3: Diffusion coefficients of water and oxygen in bulk PHB and PHB/graphite system. Average of three repeat runs \pm standard deviation. Simulations were run in the NVT ensemble at 500 K.

In order to characterise the permeant behaviour at the graphite/polymer interface, the density of polymer and permeants along the z axis was calculated. Density profiles, averaged over three repeat simulations, are shown in Figure 4.11. The plots for each separate run are shown in Appendix B. It can be seen from Figure 4.11(a) that water molecules are more concentrated ~ 4 A further from the surface than the dense polymer region. On the other hand, from Figure 4.11(b), it can be seen that the most densely populated region for oxygen is ~ 0.5 Å closer to the graphite than the polymer. Since the carbon atoms in the graphite model have no partial charges, the oxygen and water permeant models will be drawn to the surface via vdW forces only, rather than electrostatic interactions. The oxygen molecules can pass through the dense polymer layer and gather closer to the surface, since the non-polar oxygen doesn't experience significant interactions with the polymer atoms. On approaching the surface, the water molecules on the other hand get "trapped" on the far side of the dense polymer layer, as they have previously been shown to experience hydrogen bond interactions with the polymer [133].

4.4 Conclusions and Future Work

Diffusion in crystalline and graphene-filled PHB systems was investigated using MD simulations. Bulk models of crystalline PHB were constructed based on the α -crystal unit cell examined in the previous study [133]. In addition to the infinitely bonded model, where polymer chains are periodically connected along the crystallographic axis, a finite chain crystal was created by breaking the chains and capping them with chain ends. Despite the presence of chain ends introducing some mobility, the crystalline structure remained stable in its helical configuration throughout the simulations at 200 K. Analysis of backbone torsional angles

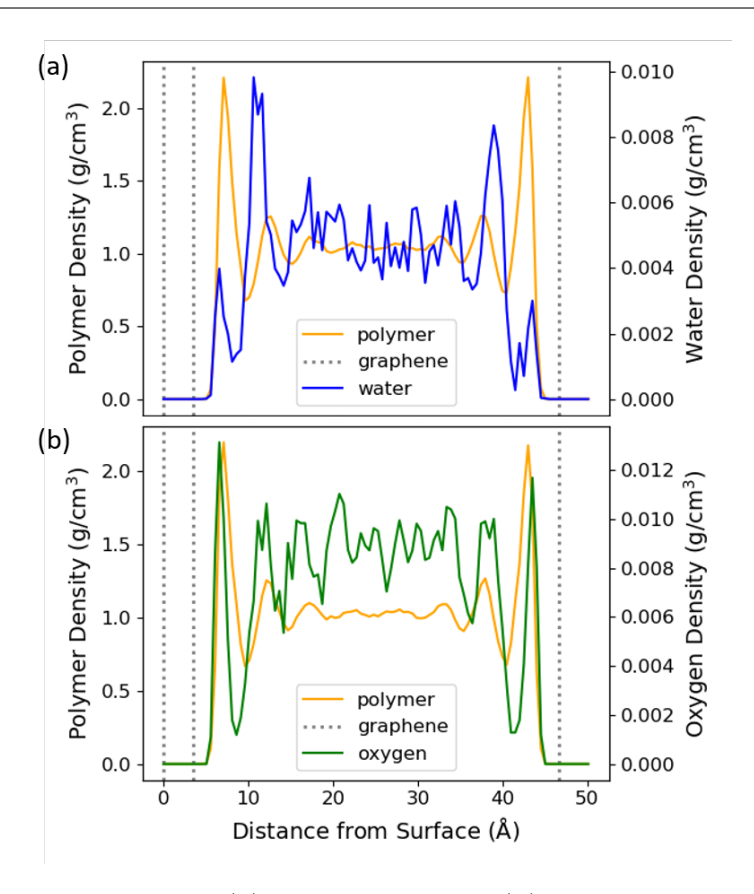


Figure 4.11: Density profiles (a) PHB and water (b) PHB and oxygen. Distance in relation to the middle graphene sheet. Dotted lines show the average positions of the three graphene sheets. Results are averaged over three simulations.

revealed that the free chain ends caused increased rotational flexibility in three of the four key dihedral angles. However, the most frequently adopted torsional states remained consistent with those in the infinite chain crystal. This suggests that the dense packing of the helical chains provides energetically favourable non-bonded interactions that stabilise the structure, even in the absence of continuous bonding along the chain axis.

Diffusion simulations of water and oxygen in the PHB crystal systems revealed that the MSDs were very small in both cases. Although the introduction of chain ends in the finite chain crystal model allowed some movement of permeants, the limited MSD values suggest that diffusion within crystalline domains is negligible on the 100 ns time scale of the simulations. As with the amorphous system, oxygen exhibited greater mobility than water in the finite crystal model, while water movement was strongly influenced by electrostatic interactions with the polymer, as reflected in the RMSDs.

The influence of a graphite surface on the diffusion of water and oxygen in amorphous PHAs was also examined. The presence of the surface induced densification and alignment of polymer chains near the interface, as observed through VMD trajectory visualisation and supported by density profile analysis. The PHB chains showed reduced mobility compared to the bulk system. When compared with simulations of bulk amorphous PHB, the diffusion coefficients of both water and oxygen were lower in the graphite-filled system. This reduction is likely due to (1) restricted polymer mobility, which limits the formation of transient cavities for permeants to move through, and (2) accumulation of permeants at the interface. The permeants exhibited distinct interfacial behaviours: oxygen molecules were able to penetrate into the dense polymer layer near the graphite due to vdW attractions, whereas water molecules preferentially localised on the opposite side of the polymer, where electrostatic interactions with the polymer dominated their diffusion behaviour.

These simulations enhance our understanding of how crystalline ordering and interfacial interactions influence gas transport in PHAs, offering molecular-level insights relevant to the design of compostable food packaging materials. In particular, the findings confirm that crystalline domains restrict diffusion, while the presence of a filler surface induces polymer alignment and alters permeant behaviour near the interface. Such effects should be carefully considered when engineering composite packaging films, where both crystallinity and filler content can be tuned to optimise barrier performance.

Building on this work, future studies could aim to develop more realistic models of PHA composites that capture the heterogeneous nature of semi-crystalline polymers. In practice, PHAs consist of crystalline regions embedded within an amorphous matrix, often in the presence of nanofillers. A combined model incorporating both amorphous and crystalline phases alongside a filler surface would provide a more accurate representation of the microstructure and enable more predictive simulations of gas transport. The graphite surface model used here could also be extended to other common fillers, such as hexagonal boron nitride (BN), which shares a similar layered structure. By assigning partial charges and adjusting force field parameters accordingly [146], the influence of polar surfaces on polymer structure and permeability could be investigated. This would provide a stronger link between the PHB/filler systems simulated and the filled polymer films investigated experimentally in Chapter 5.

Chapter 5

Characterisation of Solvent-Cast PHB Films

Abstract

This chapter investigates the influence of additives on the thermal, barrier, mechanical and microstructural properties of polyhydroxybutyrate (PHB) films prepared via solvent casting. Specifically, the study evaluates the effect of boron nitride (BN) as a filler and triacetin (TA) as a plasticiser on the crystallisation behaviour, melting characteristics, water barrier performance and mechanical properties of PHB. Differential scanning calorimetry (DSC), scanning electron microscopy (SEM), water contact angle, water vapour transmission measurements and texture analysis were employed to characterise the films. Results indicate that the incorporation of TA leads to a modest reduction in the melting temperature and an increase in spherulite size, whereas BN acts as an effective nucleating agent, increasing both the crystallisation temperature and the overall degree of crystallinity. These modifications in thermal behaviour suggest potential improvements in processing and production parameters. However, both additives were found to lower the water barrier properties of the films, as evidenced by increased water vapour permeability and decreased water contact angles. SEM analysis revealed the presence of additional holes and microvoids in the modified films, which likely contribute to the diminished moisture resistance. Texture analysis showed that TA improved film elasticity at the expense of strength, while lower concentrations of BN generally improved both strength and elasticity. Collectively, these findings offer valuable insights into the complex interplay between additive chemistry and the functional properties of sustainable polymer systems.

5.1 Introduction

Conventional petroleum-based plastics, such as polyethylene and polypropylene, dominate the packaging industry but are non-compostable, leading to accumulation in landfills and marine environments. As the demand for sustainable alternatives grows, PHB, a biopolymer produced by microbial fermentation, has emerged as a promising candidate for environmentally friendly food packaging. Derived from renewable resources, PHB is fully compostable under natural conditions, breaking down into carbon dioxide and water without leaving toxic residues [147], making it a potential solution to mitigate plastic pollution. Additionally, PHB films are inherently biocompatible and non-toxic [148], ensuring safety for food contact applications. PHB exhibits good mechanical strength in terms of tensile properties and rigidity, along with thermal stability and barrier performance, which are essential characteristics for preserving food quality and extending shelf life. However, its widespread adoption has been limited by drawbacks such as brittleness and poor elasticity, which reduce its suitability for applications requiring flexibility or impact resistance, as well as its relatively high production costs compared to conventional plastics. Research efforts are therefore increasingly focused on improving PHB's performance through the incorporation of additives, such as plasticisers and fillers and optimising production methods to reduce costs.

Filler particles are commonly incorporated into polymers to modify their thermal, mechanical and barrier properties. Fillers typically act as nucleating agents, influencing the crystallisation process and the development of spherulitic structures. The effect of these additives on PHB's barrier properties is highly dependent on their type and concentration. Manikandan et al. investigated a variety of graphene-based fillers [60] and found that all of them improved the water barrier of PHB to some extent. Conversely, Cretois et al. measured water permeability in polyhydroxyalkanoate (PHA) composites containing clay-based filler particles [62] and found that increasing the concentration of filler led to higher water permeation. BN is of interest as a filler due to its high thermal conductivity, chemical inertness and resistance to high temperatures [149]. BN has previously been shown to be an effective nucleant for PHB [150], allowing the polymer to crystallise from the melt at higher temperatures [59]. Additionally, BN can be surface-functionalised to enhance dispersion within a polymer matrix, making it a promising candidate for improving PHB's performance.

Plasticisers are typically added to help processability and can also influence the thermal properties of PHB by lowering its melting temperature $(T_{\rm m})$. The narrow temperature window between PHB's melting and thermal decomposition can cause issues during melt processing, and reducing $T_{\rm m}$ through plasticiser incorporation could mitigate these challenges. Majerczak *et al.* reported that plasticisers

could lower PHB's glass transition temperature $(T_{\rm g})$ by up to 297 K and its $T_{\rm m}$ by up to 286 K, depending on the type and concentration used [49]. In terms of water barrier, the effect of plasticisers has been found to vary. Quispe *et al.* studied the effect of glycerol-based plasticisers on water permeability in PHB films [151]. While some plasticisers enhanced the water barrier, others significantly increased water permeation, with the observed differences primarily attributed to variations in the size of the plasticiser molecules. TA is a particularly suitable plasticiser for food packaging applications due to its excellent compatibility with PHAs [49], biodegradability and low volatility. Additionally, its non-toxic nature and approval for food contact applications [152] make TA a viable option for improving PHB's processability without compromising safety.

The microstructure of semi-crystalline polymers such as PHB is strongly influenced by the formation of spherulites during crystallisation, where polymer chains arrange into ordered lamellae radiating outward from nucleation sites [47]. This microstructural arrangement plays a crucial role in determining PHB's bulk properties, including mechanical strength and barrier performance. Pure PHB is known for its brittleness, which is largely attributed to the formation of large spherulites that facilitate crack propagation. Majerczak et al. reviewed the effect of fillers on PHB crystallisation [3] and reported that fillers generally act as nucleating agents, promoting the formation of a higher number of smaller spherulites. This structural modification can enhance toughness and impact resistance by reducing the size of brittle crystalline domains. However, the relationship between crystallinity and mechanical properties in PHB composites remains complex, as some fillers improve strength and modulus while others weaken the material due to poor dispersion or adverse filler-polymer interactions.

A strong water barrier is essential for food packaging applications, as it helps prevent food spoilage and extends shelf life. Additionally, effective moisture resistance reduces the need for multilayer packaging, contributing to sustainability by minimising material usage and waste. The key parameters used to assess a polymer's water barrier performance include the water contact angle (θ) , water vapour transmission rate (WVTR) and the permeability coefficient. WVTR and permeability coefficient are closely related; the permeability coefficient can be calculated from the WVTR by accounting for the film thickness and the partial pressure difference of water vapour across the film (see Table 2.3, Chapter 2). A polymer with superior water resistance will exhibit a high θ , indicating hydrophobicity, and lower WVTR and permeability values. Conversely, a lower θ and increased WVTR and permeability suggest weaker barrier performance, leading to higher moisture ingress. In this study, θ , WVTR, and permeability are measured experimentally for different formulations of PHB films.

There is currently a gap in the literature regarding the relationship between the spherulitic microstructure of PHAs and their bulk properties. Consequently, the influence of fillers and plasticisers on the microstructure, mechanical performance and barrier properties of sustainable polymers remains insufficiently understood. The primary objectives of this experimental work are:

- Use DSC to investigate the thermal behaviour and crystallinity of solvent-cast PHB films.
- Measure the WVTR and θ of the films.
- Use SEM to analyse the crystalline microstructure.
- Assess the impact of additives on mechanical properties using texture analysis.

These objectives will help to relate the microstructure of PHB composites to their bulk properties.

The methodology used for film casting and characterisation can be found in Section 2.2 (Chapter 2).

5.2 Results and Discussion

5.2.1 NMR

NMR was used to check the purity of PHB. Analysis of the ¹H NMR spectra revealed three main peaks (excluding the residual solvent peak from deuterated chloroform). These peaks correspond to the characteristic proton environments in the PHB molecule, as shown in Figure 5.1. A key diagnostic peak for the presence of HV monomers would appear at approximately 0.9 ppm, attributed to the CH–CH₂–CH₃ protons, which are not present in PHB. The absence of a signal in this region confirms that the polymer is a PHB homopolymer rather than a poly(hydroxybutyrate-co-hydroxyvalerate) (PHVB) copolymer. Furthermore, no additional peaks indicative of impurities were observed, suggesting the ethanol purification step was effective.

5.2.2 Spherulitic Microstructure

SEM was used to investigate the spherulitic microstructure of the PHB films. SEM images for each formulation are shown in Figure 5.2. Attempts to image at higher magnification resulted in structural damage to some of the films, likely caused by the increased current density of the electron beam. The visibility of spherulites in

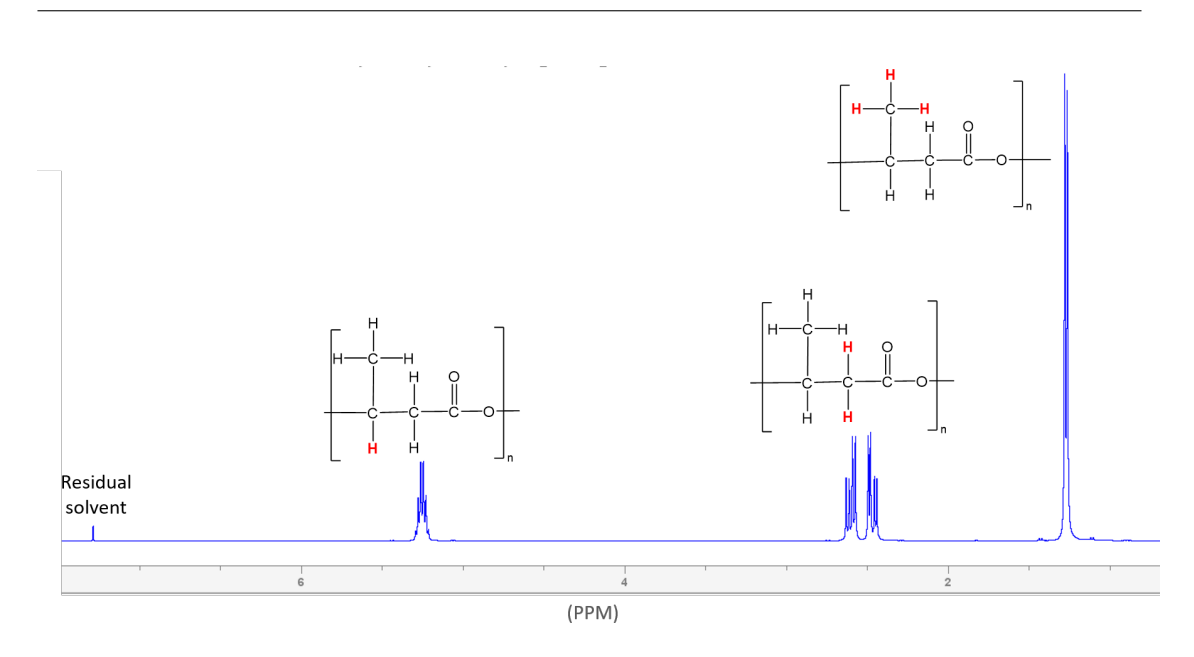


Figure 5.1: NMR spectra of purified PHB powder (in deuterated chloroform solution).

the SEM images varied depending on the film formulation. Spherulite boundaries are most clearly visible in the PHB_TA and PHB_1BN samples (Figures 5.2(b) and (d), respectively). Although less distinct, a spherulitic microstructure can also be observed in PHB, PHB_TA/1BN and PHB_0.25BN (Figures 5.2(a), (c), and (e), respectively). For the sample with the lowest BN concentration (PHB_0.06BN), imaging difficulties prevented the detection of any spherulites. A quantitative analysis of spherulite area distribution was attempted using automated boundary detection tools, including Segment Anything [14]. While spherulite boundaries were successfully identified in the PHB_TA samples, Segment Anything was ineffective for the other formulations, due to the spherulites being much smaller and their boundaries less defined. A voronoi analysis performed using ImageJ software was also explored for spherulite identification and area computation; however, similar limitations were encountered with unplasticised films. Example use of these tools is displayed in Figure 5.3. Consequently, it was determined that automatic detection and measurement of spherulite sizes were not feasible for all samples. Manual measurement was considered impractical for high-throughput analysis due to the large number of spherulites per image. Improved SEM imaging, particularly for pure PHB samples, may enable the application of image analysis software for quantitative assessment of spherulite size distribution in the future. For this study, a qualitative analysis was conducted to compare relative trends in microstructure across pure polymer, plasticised and filled samples.

Notably, distinct gaps and holes are present in PHB_TA and PHB_0.25BN

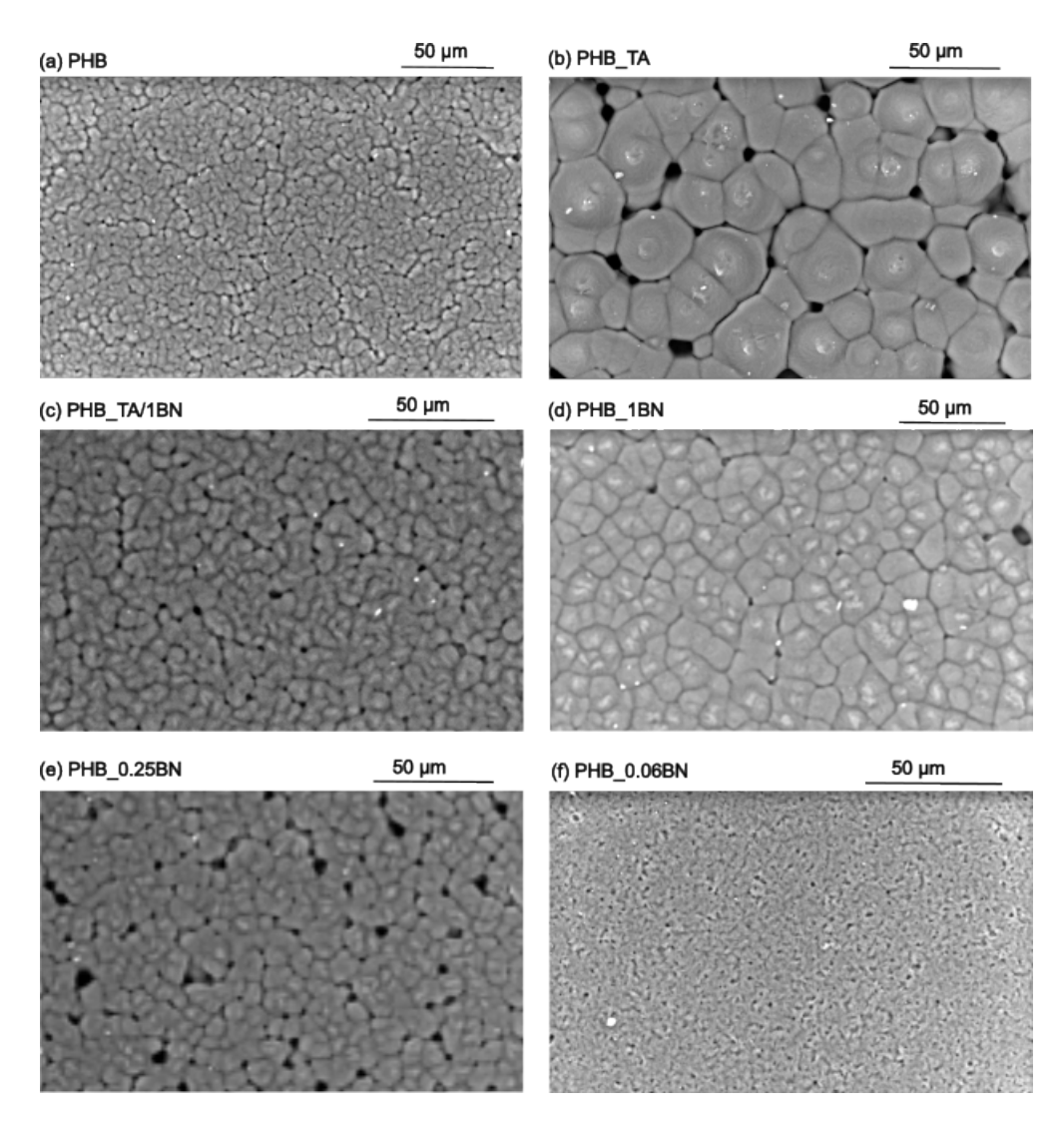


Figure 5.2: SEM images of PHB films.

(Figures 5.2(b) and (e)), suggesting a more porous microstructure that may result from the incorporation of additives. In their study on PHB microstructures, Quispe et al. also observed a uniform morphology in pure PHB, while samples containing additives exhibited increased porosity and the presence of microvoids [151]. For those films imaged at higher magnification, it was possible to qualitatively compare spherulite sizes. The plasticised film PHB_TA appears to have the largest spherulites, consistent with findings by Majerczak et al., who reported that plasticised PHB forms larger crystalline domains than pure and filled polymer [58]. This suggests that TA influences polymer chain arrangement during crystallisation, promoting the growth of larger spherulites and inhibiting nucleation at new sites. Comparing Figures 5.2(a) and (d), the spherulites in the filled sample PHB_1BN appear larger than those in pure PHB. This observation contra-

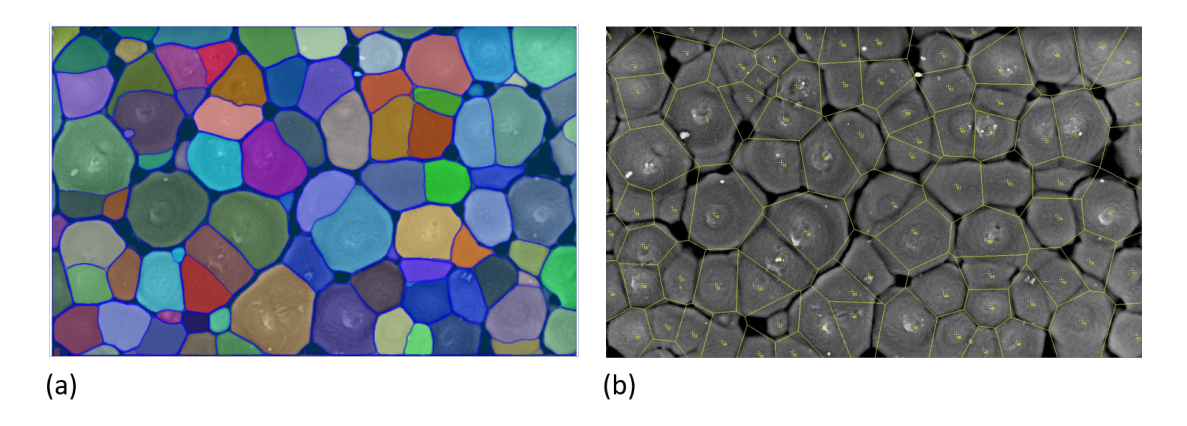


Figure 5.3: Spherulite area analyses on SEM images of PHB_TA film. (a) Output of the Segment Anything tool [14] (b) Voronoi analysis using ImageJ software.

dicts the findings of Puente et al., who reported that the addition of BN reduces spherulite size in PHB [59]. The discrepancy may be attributed to differences in filler dispersion, particle size or processing conditions. It is also important to note that imaging the spherulitic structure in pure PHB was more challenging than in the other formulations, resulting in reduced clarity and potential difficulty in accurately discerning spherulite boundaries. In their review of the effects of fillers on PHB microstructure, Majerczak et al. reported that in all studies reviewed, the addition of filler either reduced or had no effect on spherulite size [3]. Therefore, the apparent smaller spherulites in the pure PHB image may be an artefact of limited image resolution or contrast, rather than a true representation of the microstructure.

5.2.3 Crystallinity and Thermal Properties

Thermal properties and degree of crystallinity of the films were measured using DSC. The melting temperature $(T_{\rm m})$ of the film is taken as the peak of the first melting curve and the area under this curve was used for determining $X_{\rm c}$. The crystallisation temperature $(T_{\rm c})$ was taken as the peak of the exothermic crystallisation curve. Shifts in these peaks on the incorporation of additives can be seen in Figure 5.4. The results from the DSC analysis for all film formulations are given in Table 5.1.

The thermal analysis showed that TA incorporation resulted in a slight reduction in $T_{\rm m}$. This effect has been reported in the literature for PHB plasticised with TA [49, 151]. The decrease in $T_{\rm m}$ is attributed to the disruption of intermolecular forces and increased polymer chain mobility, which lower the energy required for the transition from solid to molten state. Plasticisers such as TA also increase free volume within the polymer matrix, further enhancing chain mobility

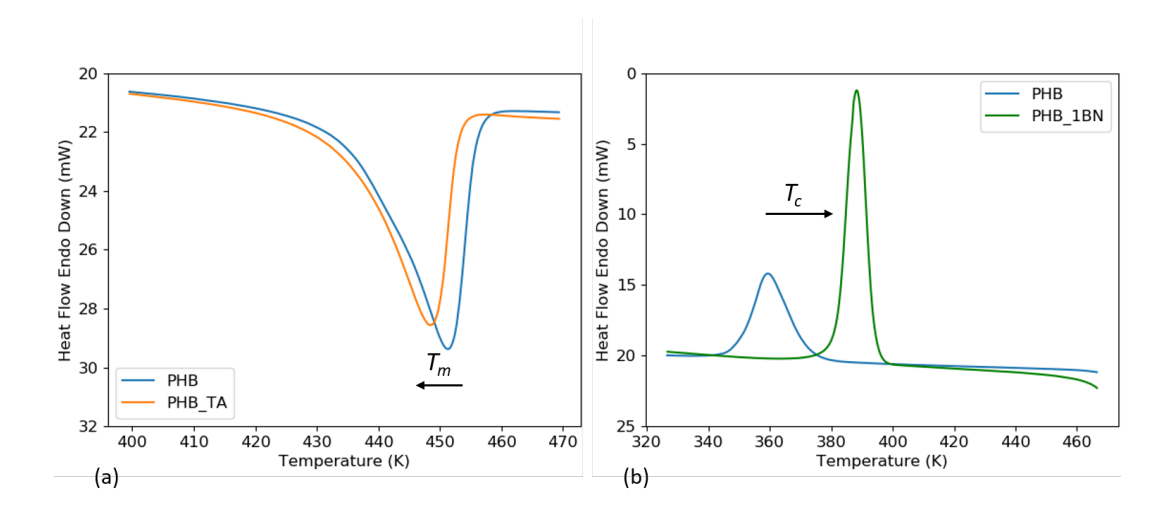


Figure 5.4: (a) increase in T_c on addition of BN and (b) decrease in T_m on addition of TA, compared to pure PHB.

	$T_m (\mathrm{K})$	T_c (K)	$X_c~(\%)$
PHB	451.3 ± 0.3	363.9 ± 5.5	41.0 ± 2.5
PHB_TA	449.4 ± 0.6	365.0 ± 6.4	48.7 ± 11.6
PHB_TA/1BN	448.6 ± 1.2	389.1 ± 0.9	69.5 ± 6.4
PHB_1BN	451.3 ± 0.7	387.9 ± 0.3	64.2 ± 4.1
PHB_0.25BN	451.2 ± 0.5	390.5 ± 0.3	65.1 ± 3.3
PHB_0.06BN	451.6 ± 0.6	388.3 ± 1.5	71.3 ± 1.3

Table 5.1: Thermal properties of PHB films. Results are an average of three repeats \pm the standard deviation. Values for each repeat are listed in Appendix C.

and lowering the melting temperature. In terms of crystallinity, due to high variation in X_c it is difficult to establish any trends on plasticiser addition. X_c was higher in all BN-filled samples compared to pure and plasticised PHB. The films containing the lowest concentration of BN had the highest X_c of 71.3 \pm 1.3%, versus 41.0 \pm 2.5% for pure PHB. The addition of BN increased the T_c without affecting T_m . These effects can be attributed to the nucleating role of BN, which provides additional surfaces for crystallisation, reducing the energy barrier for nucleation and promoting the formation of crystalline regions [66]. A similar effect has been observed in PHB composites with other nucleating fillers [59]. In their simulation study on polymer crystallisation, Wadkin-Snaith $et\ al$ attributed the observed increase in T_c to polymer-surface interactions [153], which lower the free energy of crystal nuclei at the surface and reduce the nucleation barrier through

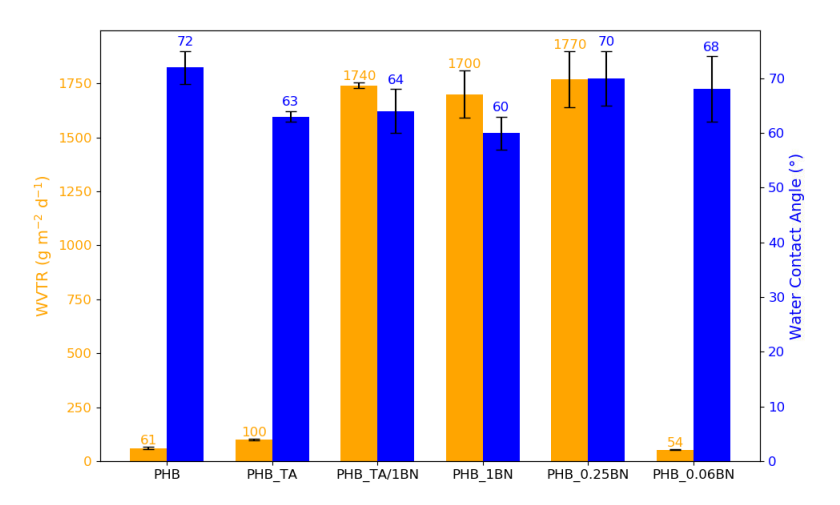


Figure 5.5: Water barrier properties of PHB films.

enhanced chain alignment. The increase in T_c suggests that BN facilitates earlier crystallisation, likely improving processing stability and mechanical consistency.

5.2.4 Water Barrier Properties

In order to evaluate the water barrier performance of the various films, θ , WVTR and permeability were measured. Results are given in Table 5.2 and Figure 5.5. A snapshot showing the water contact angle on a PHB film is shown in Figure 5.6.

	$\overline{ ext{WVTR} \left(ext{g.m}^{-2}. ext{d}^{-1} ight) }$		Permeability (Barrer)		θ (°)	
PHB	61	± 6	926	± 97	72	± 3
PHB_TA	100	± 5	1520	± 69	63	± 1
PHB_TA/1BN	1740	± 13	26400	± 193	64	± 4
PHB_1BN	1700	± 110	25700	± 1660	60	± 3
PHB_0.25BN	1770	± 130	26900	± 1970	70	± 5
PHB_0.06BN	54	± 1	815	± 22	68	± 6

Table 5.2: Water barrier properties of PHB films. WVTR and permeability are an average of three tests \pm standard deviation. θ values are an average of five tests \pm standard deviation. Individual measurements are listed in Appendix C.

Barrier property measurements indicate that TA reduced the hydrophobicity of PHB, as shown by a lower water contact angle (θ) and higher permeability. This could be due to the presence of microvoids between spherulites, as evidenced by SEM images (Figure 5.2). Increased free volume and disrupted polymer packing

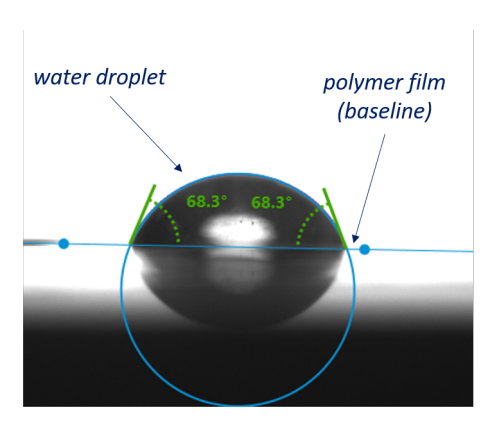


Figure 5.6: Snapshot from KRUSS Advance software, showing a water droplet placed on a PHB film.

can facilitate water molecule diffusion through the amorphous regions, reducing overall barrier performance. Despite the increase in crystallinity, BN addition negatively impacted water barrier properties. A significant increase in permeability and a noticable decrease in contact angle were measured for the two highest concentrations of BN (PHB_1BN and PHB_TA/1BN), indicating reduced hydrophobicity. Although fillers are often expected to enhance barrier properties by increasing tortuosity and restricting molecular diffusion [60], several studies have shown that water permeability can increase with filler incorporation [62, 154]. Cretois et al. reported increased water permeability in PHVB/clay composites due to hydrophilic interactions at the matrix-filler interface [62]. Similarly, Wu et al. found that SiO₂ fillers increased WVTR due to the formation of interfacial pores [154]. The results from this study suggest that BN may create similar interfacial defects, providing diffusion pathways for water molecules and counteracting the expected tortuosity effect. A good water barrier should have both a low WVTR and high contact angle. The two samples which performed best for both measurements were pure PHB and PHB₋0.06BN, which had the lowest concentration of BN.

5.2.5 Mechanical Properties

Force and distance to burst, as a function of BN concentration, are plotted in Figure 5.7. Tabulated results for all film formulations are also given in Table 5.3.

In terms of mechanical properties, TA slightly increased the film's elasticity, as indicated by a higher distance to burst for PHB_TA and PHB_TA/1BN compared to pure PHB. However, this enhancement in flexibility was accompanied by a decrease in film strength, observed through a reduction in force to burst. Similar trends have been reported in plasticised PHB studies, where elongation at break increased while tensile strength decreased [155]. These effects can be explained

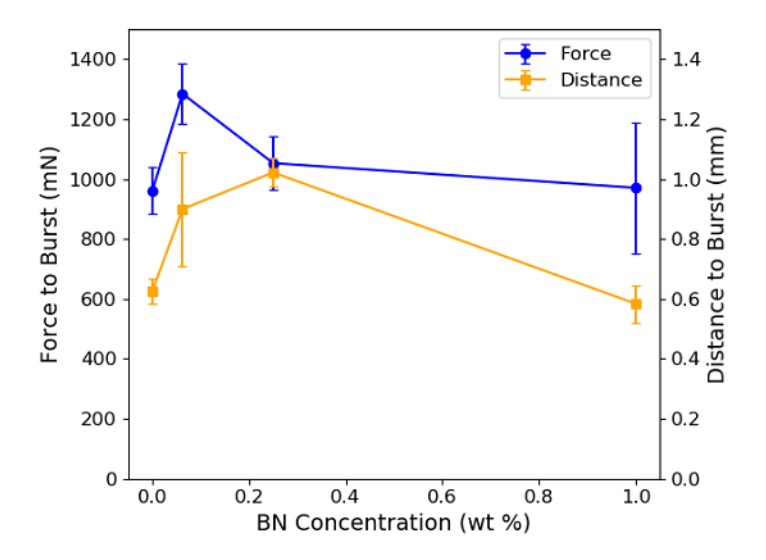


Figure 5.7: Mechanical properties of PHB films.

	Force to Burst (mN)	Distance to Burst (mm)
PHB	961 ± 76	0.63 ± 0.04
PHB_TA	559 ± 64	0.78 ± 0.09
PHB_TA/1BN	863 ± 118	0.72 ± 0.08
PHB_1BN	971 ± 218	0.58 ± 0.06
PHB_0.25BN	1053 ± 90	1.02 ± 0.05
PHB_0.06BN	1285 ± 102	0.90 ± 0.19

Table 5.3: Force and distance required to puncture PHB films. Results are an average of five repeats. Individual measurements can be found in Appendix C.

by the free volume theory, which states that plasticiser molecules interspersed between polymer chains reduce intermolecular forces and increase polymer mobility [156]. Given that TA is both small and compatible with PHB, it effectively increases free volume and reduces brittleness [155].

As seen from Figure 5.7, the effect of BN on the mechanical performance of PHB films appears to depend on the concentration used. Burst strengh increases with addition of BN, up to 0.25 wt %, after which it falls to a value similar to that of the unfilled sample. At the lowest BN concentration (PHB_0.06BN), an improvement was also observed in the distance to burst, however burst distance then fell at higher BN concentrations. At the highest BN concentration (PHB_1BN), no notable differences in mechanical properties were observed compared to pure PHB. Crystalline domain size plays a key role in determining mechanical perfor-

mance. Literature reports suggest that the addition of BN can reduce domain size [59, 66], which tends to improve flexibility, while simultaneously increasing overall crystallinity, which contributes to material strength. Among the concentrations tested, the lowest BN loading (PHB_0.06BN) may strike the best balance, potentially offering both mechanical reinforcement and enhanced barrier properties. This could be because a small amount of BN provides effective nucleation sites, leading to increased crystallinity and a finer crystalline microstructure, without introducing excessive aggregation or interfacial defects. At higher BN loadings, filler agglomeration and the presence of voids, as suggested by SEM images, may counteract these benefits and weaken both the barrier and mechanical performance. However, the lack of clarity in the SEM images obtained for PHB_0.06BN raise uncertainty regarding the actual change in spherulite size, highlighting the need for further investigation.

5.2.6 ANOVA Analysis of Measured Properties

ANOVA analysis was carried out to quantitatively assess the effect of formulation on the measured film properties (Table 5.4). Using a significance level (α value) of 0.05, the results show that formulation has a statistically significant effect on all measured properties, with the p value $\ll 0.01$ in all cases. Water permeability was most significantly affected by film formulation. While still statistically significant, $T_{\rm m}$ was least affected by formulation, with only the plasticised films showing a change in $T_{\rm m}$.

Property	p value
Water permeability	1×10^{-13}
$T_{\rm c}$	$5\times\!10^{-7}$
Force to burst	9×10^{-7}
Distance to burst	9×10^{-6}
$X_{\rm c}$	2×10^{-4}
θ	$4\times\!10^{-4}$
$T_{ m m}$	$7\times\!10^{-4}$

Table 5.4: p values determined from anova analysis of results.

5.3 Conclusions and Future Work

This study has demonstrated that the incorporation of additives in solvent-cast PHB films significantly affects their thermal, microstructural, mechanical and

water barrier properties. The incorporation of TA as a plasticiser led to a noticeable effect on these properties. There was a slight decrease in melting temperature, which can improve processability in polymers, and formation of much larger spherulites. TA also slightly improved the elasticity compared to pure PHB, however film strength and water barrier properties were reduced. BN acted as a nucleating agent, increasing both the crystallisation temperature and the degree of crystallinity. However, despite its expected role in enhancing barrier properties, higher concentrations of BN unexpectedly increased water permeability, likely due to the formation of interfacial defects. However for the lowest concentration of BN, there was a noticeable improvement in both water barrier and mechanical properties. These changes have important implications for polymer production and processing.

Future work should extend these findings through improved SEM imaging to better detect spherulite boundaries in PHB films. Additionally, the development and application of advanced analysis tools for quantifying spherulite area distributions could provide deeper insights into the relationship between spherulite size and bulk properties. Further studies should also investigate the role of interfacial interactions between the polymer matrix and fillers, particularly in the case of BN, to better understand its unexpected impact on water permeability. These findings contribute to a broader understanding of the interplay between additive chemistry, microstructure and functional properties, with implications for the future development of PHB-based materials in sustainable food packaging applications.

Chapter 6

Conclusions

Polyhydroxyalkanoates (PHAs), and in particular polyhydroxybutyrate (PHB), have attracted considerable interest as bioderived and compostable alternatives to conventional plastics in food packaging applications. However, the practical use of PHB is limited by its inherent brittleness, high crystallinity and modest gas barrier performance. Copolymerisation with other monomers, such as hydroxyvalerate (HV), and the incorporation of plasticisers and fillers offer promising strategies to tailor its properties and enhance its performance. Despite significant progress in this area, there remains a gap in the literature concerning the detailed relationship between additive inclusion, microstructural features (such as crystallinity and chain conformation) and the resulting bulk properties, particularly gas barrier behaviour.

The overarching aim of this project was to address this gap by employing a combination of molecular dynamics (MD) simulations and experimental characterisation to investigate how additives and polymer microstructure influence the performance of PHB-based materials. A particular focus was placed on understanding the interactions at the filler/polymer interface, as well as the morphological and dynamic behaviour of water and oxygen molecules in both amorphous and crystalline PHB systems. Through this approach, the work aimed to provide insight into the role of microstructure in determining barrier properties and to explore how these properties might be tuned through rational material design.

6.1 Summary of Results

In the first set of simulation studies (Chapter 3), models for both amorphous and crystalline PHAs were developed and validated against established experimental and simulation data from the literature. These models successfully captured key structural and thermodynamic properties, providing a robust framework for investigating polymer behaviour. Crystal surface and cohesive energy calculations

revealed that PHB exhibits higher values than polyhyrdroxyvalerate (PHV), helping to explain PHB's comparatively higher melting temperature and greater thermal stability. Simulations also showed that increasing the concentration of HV monomers led to a reduction in the glass transition temperature, attributed to the bulkier side groups in HV disrupting efficient chain packing. To assess barrier properties, MD simulations were used to examine the diffusion of water and oxygen through amorphous PHB and PHV. The resulting diffusion coefficients were consistent with experimental trends, where available, with oxygen found to diffuse more rapidly than water. This was attributed to the stronger electrostatic interactions between water molecules and the polar polymer backbone, which hindered water mobility. While PHB and PHV displayed comparable water barrier properties, due to its lower density, PHV was significantly more permeable to oxygen, making it a less effective oxygen barrier material.

Chapter 4 focussed on diffusion behaviour in crystalline PHB and in systems where a graphene surface was introduced. Two models of bulk crystalline PHB were constructed from the known unit cell: one featuring infinitely bonded polymer chains and another incorporating free chain ends. Both models were found to be structurally stable throughout the simulations, with the model containing free chain ends showing only minor deviations. This stability suggests that the tightly packed helical arrangement of PHB chains facilitates energetically favourable nonbonded interactions, which are sufficient to maintain structural integrity even in the absence of periodic bonding. Diffusion simulations with water and oxygen permeants confirmed that, while minimal movement was observed in the crystalline system with free chain ends, the overall mean squared displacement values indicated negligible diffusion, reinforcing the view that gas transport in PHB occurs primarily through the mobile amorphous phase. In the presence of a graphene surface, PHB chains were observed to form dense interfacial layers, resulting in reduced chain mobility near the filler. This densification contributed to a decrease in diffusion coefficients for both water and oxygen compared to the bulk amorphous system. Interestingly, spatial distribution analysis revealed distinct behaviours for the two permeants: oxygen molecules tended to accumulate slightly closer to the graphene surface, likely driven by van der Waals attractions, while water molecules preferentially located themselves just beyond the dense polymer region, consistent with their stronger electrostatic interactions with the polar polymer chains.

For the final results chapter (Chapter 5), experimental work was carried out to investigate the effect of additives on the microstructure and properties of PHB films. Thin, transparent and flexible PHB films were successfully produced using solvent casting. Two additives were evaluated: triacetin (TA), used as a plasticiser, and boron nitride (BN), employed as a filler. A comprehensive charac-

terisation of the resulting films was conducted, including assessments of polymer microstructure, water barrier performance, thermal behaviour and mechanical properties. The addition of TA led to the formation of larger spherulites, indicating altered crystallisation behaviour. While film flexibility was slightly improved with TA, this came at the cost of reduced tensile strength and diminished water barrier properties. The incorporation of TA also slightly lowered the melting temperature, which could be advantageous for improving the material's processability. In contrast, BN acted as an effective nucleating agent, increasing both the crystallisation temperature and overall crystallinity of the PHB films. However, the filler generally resulted in poorer water barrier properties, evidenced by a lower water contact angle and significantly higher water permeability. An exception was observed at the lowest BN concentration, where a modest improvement in water barrier performance was noted.

Taken together, the simulation and experimental results demonstrates that the microstructural features in PHB, including crystallinity, HV incorporation and the presence of additives, play a key role in determining barrier performance. The simulation studies established validated models for both crystalline and amorphous PHAs, provided the first molecular-level insights into diffusion behaviour in crystalline and filled PHB, and revealed how filler surfaces alter chain mobility and permeant distribution at the polymer interface. The experimental studies complemented this by showing how plasticisers and fillers influence spherulite formation, crystallinity and the resulting trade-offs between mechanical, thermal and barrier properties. By integrating molecular simulation with experimental characterisation, this work advances understanding of the structure-property relationships that govern PHB performance and contributes new mechanistic insights into how additives and microstructure can be manipulated to tailor barrier properties for packaging applications.

6.2 Outlook and Future Work

The use of PHB at scale as a packaging film remains constrained by several key factors. Among these is its commercial viability, which is currently limited by high production costs. These costs are largely attributable to the use of expensive high-carbon feedstocks, which contributes 30-50% of the production costs of PHAs [157]. As a result, PHB remains less economically competitive compared to petroleum-derived plastics, despite its favourable environmental profile. To address this economic barrier, a growing body of research has focused on identifying alternative, low-cost feedstocks for PHAs. Promising options include agricultural by-products, food waste and even municipal wastewater sludge, which offer the dual benefits of cost reduction and waste valorisation [157, 158]. Future work

should continue to explore these unconventional feedstocks, alongside improvements in fermentation efficiency, microbial strain engineering and downstream recovery processes.

From a functional perspective, while PHB has demonstrated moderate water barrier properties, it is unlikely to be suitable for packaging highly moisture-sensitive foods without further modification. Strategies such as surface coating with hydrophobic layers, blending with complementary biopolymers or incorporating nanofillers could be used to reduce water vapour permeability and extend the material's applicability. Further research should evaluate the long-term performance, recyclability and environmental impact of such modifications.

In terms of simulation, this study focused on purely crystalline and purely amorphous PHAs to isolate and understand the effects of microstructure and filler surfaces on diffusion. However, real-world PHB materials typically consist of a heterogeneous mix of crystalline, amorphous and rigid amorphous regions. Future modelling efforts should aim to construct more representative multi-phase models that integrate these domains and capture their interfacial interactions. Such models could also incorporate additives explicitly, including filler surfaces, plasticiser molecules and polymer blends, to better understand how they influence chain dynamics and gas transport at the molecular level.

On the experimental side, improvements in imaging techniques could enhance the quantitative analysis of microstructure. For instance, more advanced or higher-resolution scanning electron microscopy, potentially combined with image processing software, could enable accurate measurement of spherulite size distributions. This would facilitate a more precise correlation between microstructural features and bulk material properties, especially mechanical strength and barrier performance. Similarly, further characterisation of interfacial morphology in filled systems using techniques such as atomic force microscopy or X-ray scattering could provide deeper insights into the structure-property relationships governing PHB-based nanocomposites.

Finally, bridging the simulation and experimental domains more closely represents a promising future direction. Validating simulation predictions against experimental data, for example, comparing diffusion coefficients or crystallinity trends, would strengthen the reliability of computational tools in guiding material design. Coupling these simulations with machine learning approaches could accelerate the screening of new formulations, aiding in the discovery of PHB-based materials with optimised performance for sustainable food packaging.

Appendix A

Additional Force Field Details

This Appendix contains further information on the force field parameters used for modelling PHAs, relevant to Chapters 3 and 4. Lists of all the partial charges used for the PHA molecules are given, followed by additional details on the water and oxygen models used for diffusion simulations.

A.1 Partial Charges

Partial atomic charges for the PHA molecules were obtained from a Gaussian calculation followed by a RESP fitting using Antechamber [80, 81]. Trimers of PHB and PHV consisting of two end groups and a repeating unit were analysed. Some partial charges were scaled slightly to ensure charge neutrality when many repeat units are connected together. The trimer units and the partial charges of PHB and PHV are given in Figures A.1 and A.2, respectively. The charges for the middle (repeating) unit were applied to the unit cell when modelling the PHA crystals.

A.2 Force Field

In initial simulations of the polymer melt, an instability arose in which the hydroxyl hydrogen on the chain end collapsed into the carboxyl oxygen three bonds away. A snapshot of this occurring is shown in Figure A.3. This was caused by zero values for σ and ε on the hydroxyl hydrogen. To address this, the 1-4 non-bonded interactions between the hydrogen and oxygen were switched off, meaning they experienced no attraction or repulsion with each other.

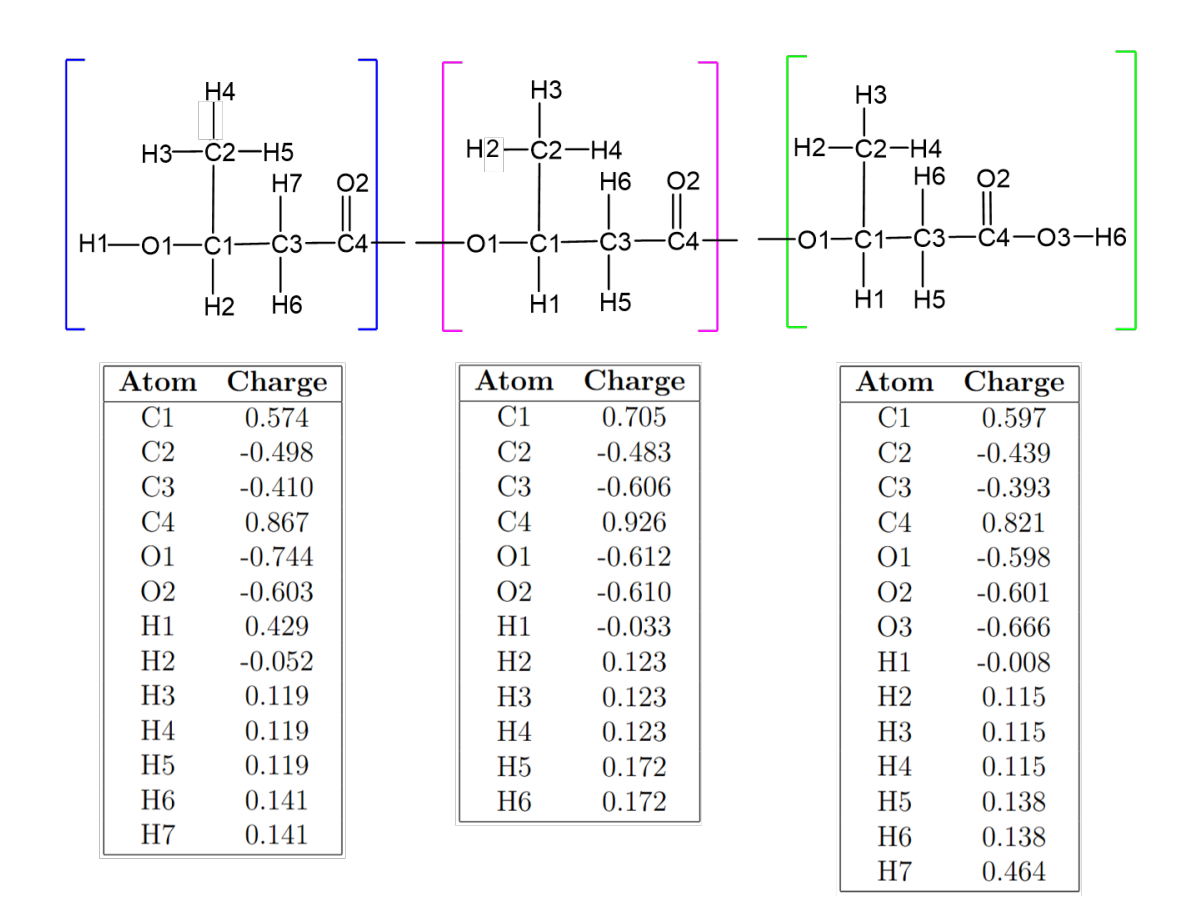


Figure A.1: Partial charges for each monomer in the PHB trimer. Units for charge = e (multiple of electron charge).

A.2.1 Water and Oxygen Models

The force field parameters for the SPC/E water model used in the current study are given in Table A.1 and the oxygen model parameters are given in Table A.2. The SHAKE algorithm was used to constrain the bonds and angles to their equilibrium values.

In Tables A.1 and A.2 K is the force constant of bonds and angles, q is the charge, m is mass, σ is van der Waals radius, ε is the Lennard-Jones potential well depth and b and θ are bond length and bond angle, respectively.

A.2.2 Bulk Water Properties

As seen from Table A.3, the density and diffusion coefficients calculated from an NPT simulation of pure water using the SPC/E model (298 K, 1 atm) are in agreement with the literature values derived from both simulation and experiment

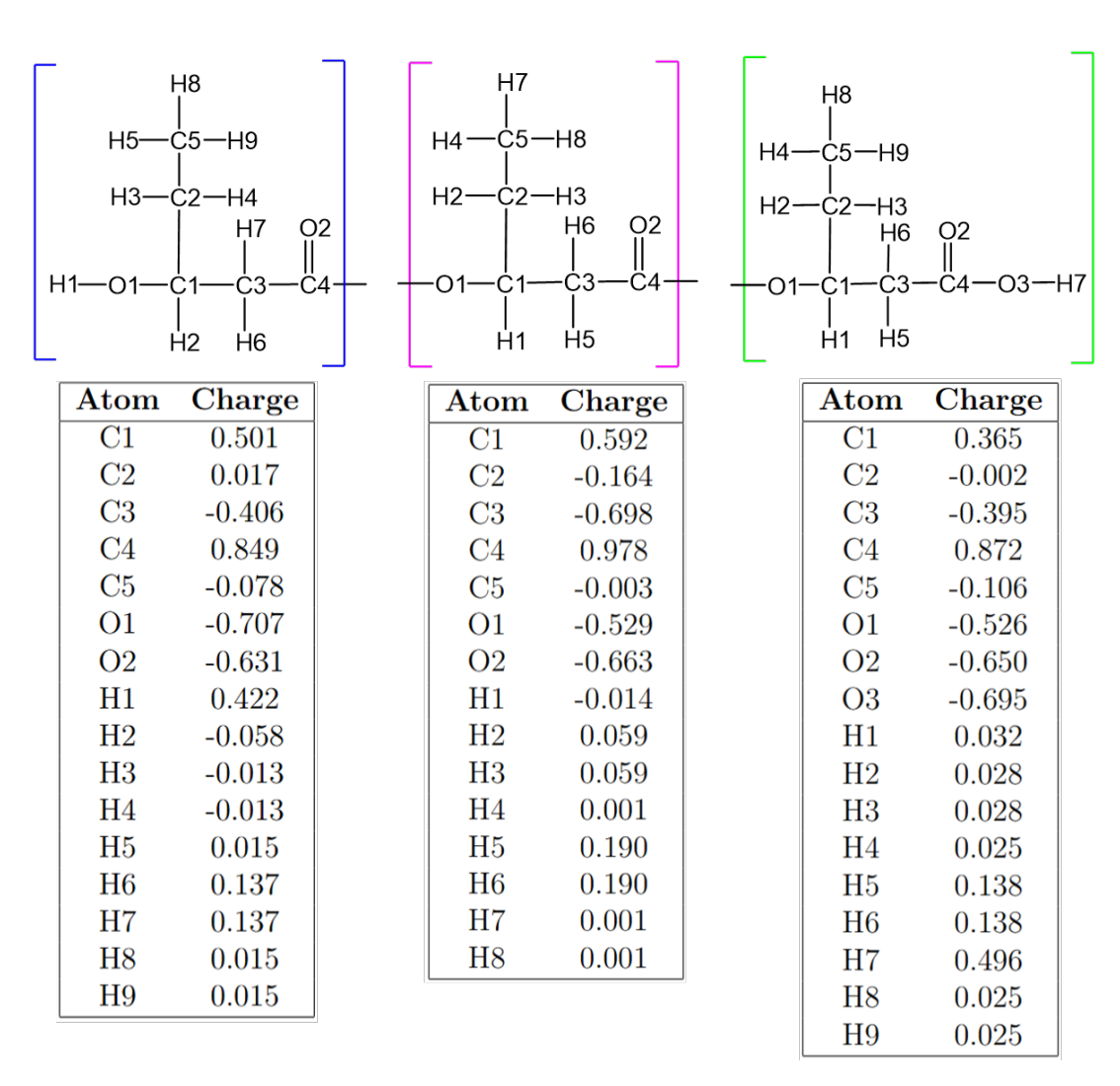


Figure A.2: Partial charges for each monomer in the PHV trimer. Units for charge = e (multiple of electron charge).

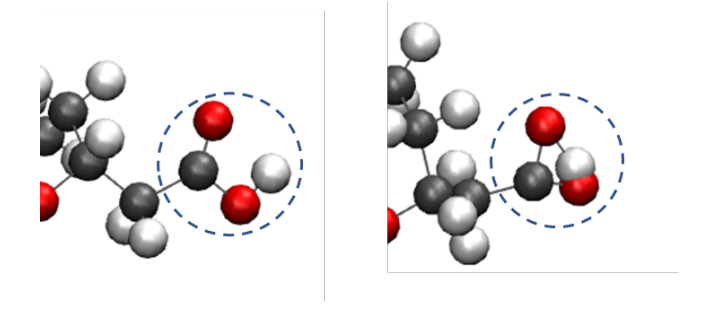


Figure A.3: Simulation failure caused by H (white) and O (red) atoms on carboxylic end group collapsing into each other.

q_O	-0.8476 e
q_H	0.4238 e
m_O	$15.9994 \text{ g mol}^{-1}$
m_H	1.008 g mol^{-1}
b_{OH}	1.0 Å
K_b	constrained
θ_{HOH}	109.47°
K_{θ}	constrained
ε_O	$0.1553 \text{ kcal mol}^{-1}$
σ_O	$3.166 \; {\rm \AA}$
$arepsilon_H$	0 kcal mol^{-1}
σ_H	0 Å

Table A.1: Force field parameters for SPC/E water model [20, 21].

q_O	0 e
m_O	16.0 g mol^{-1}
b_{OO}	$1.016~\mathrm{\AA}$
K_b	constrained
ϵ_O	$0.087~\mathrm{kcal~mol^{-1}}$
σ_O	$3.083~\mathrm{\AA}$

Table A.2: Force field parameters for Javanainen oxygen model [22].

[20, 23, 24].

	$\rho \; (\mathrm{g} \; \mathrm{cm}^{-3})$	$D (\times 10^{-9} \text{ cm}^2 \text{ s}^{-1})$
Present work	0.99 ± 0.01	2.6 ± 0.04
Simulation [20]	1.00	2.8
Experiment [23, 24]	1.00	2.3

Table A.3: Properties of liquid water using the SPC/E model in the current work compared to simulation results from literature [20] and the experimentally measured density [23] and diffusion coefficient [24].

Appendix B

Additional Simulation Results

This Appendix contains additional simulations results which are relevant to Chapters 3 and 4.

B.1 Crystalline Systems

B.1.1 Crystal Stability

To confirm stability of the crystalline systems, backbone torsional angles and lattice parameters were plotted with simulation time. The PHB torsional angle ϕ is shown as an example in Figure B.1(a) to fluctuate around a mean value of 132 °. PHB lattice parameter variation is shown in Figure B.1(b).

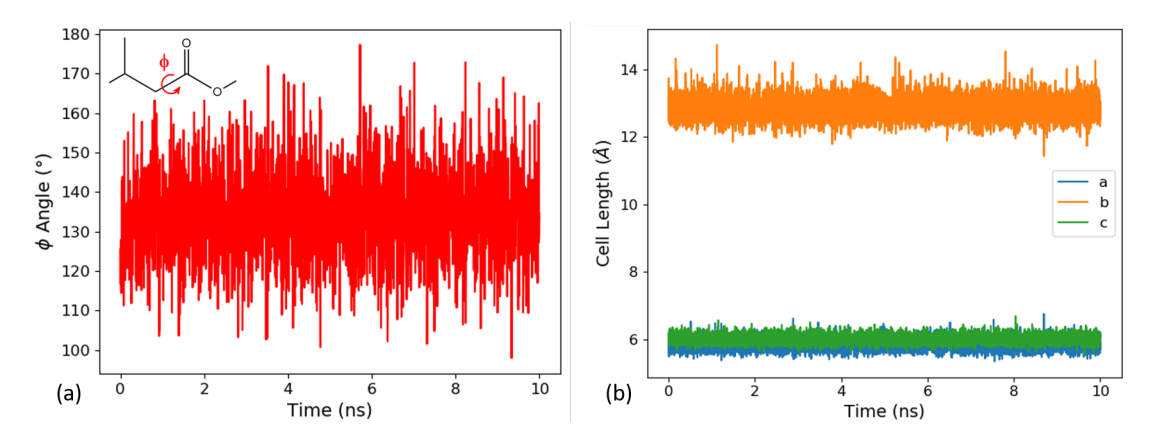


Figure B.1: (a) PHB crystal backbone dihedral and (b) lattice parameter variation during an NPT simulation at 200 K and 1 atm.

Thermal stability was tested by gradually increasing the temperature during an NPT run from 200 K to 400 K at a rate of 2.5×10^{10} K s⁻¹ and plotting the cell parameters, shown in Figure B.2. The spikes in cell length indicate the α -crystal

structure is unstable. This occurs at ≈ 327 K for PHB and ≈ 233 K for PHV. Both crystals adopt a different structure after heating past this temperature. While the PHB simulation ran to completion, the PHV simulation crashed just before 250 K.

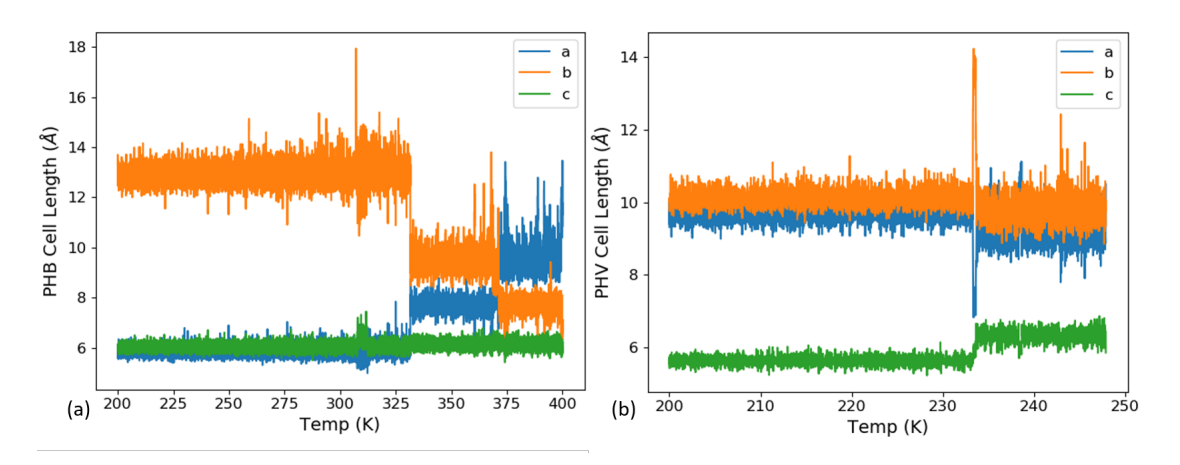


Figure B.2: Variation in crystal unit cell dimensions with increasing temperature (a) PHB and (b) PHV. Sudden deviations from the equilibrium cell lengths indicate thermal instability of the crystal.

B.1.2 Surface Energy

To calculate the (100) and (010) crystal surface energies, a vacuum layer was created by expanding the simulation box in 2 Å increments in the x or y direction, respectively. The length of the simulation cell in the z direction was left unchanged as the chains are infinite (bonded across the periodic boundary) in the z direction. VMD snapshots are shown as insets in Figures B.3 and B.4.

For each 2 Å box length increase, the potential energy of the system was compared to the potential energy of the reference system before any box expansion. The box length was increased until further changes in energy were negligible (< 4 J mol⁻¹ Å⁻²). The change in surface energy with increasing box length is plotted in Figures B.3 and B.4 (a), along with the change in relation to thickness of the crystalline slabs (R unit cells thick) (b).

B.1.3 Lattice Energy

Figure B.5 shows the crystal lattice energy as a function of chain separation. The inset shows the system used to compute the PHV crystal lattice energy. One chain

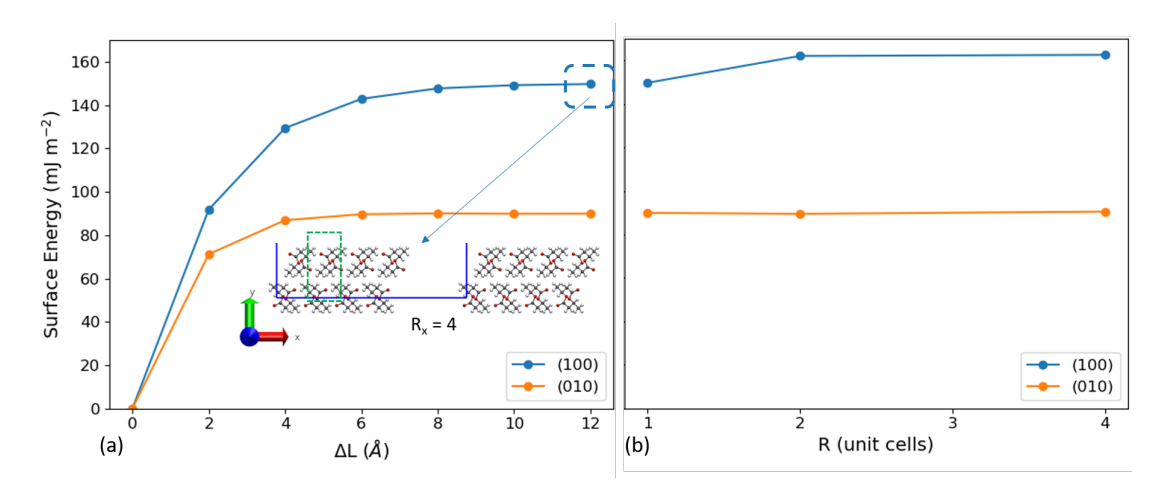


Figure B.3: Surface energy of PHB as a function of (a) vacuum layer thickness Δ L and (b) slab thickness R, for both the (100) and (010) surfaces.

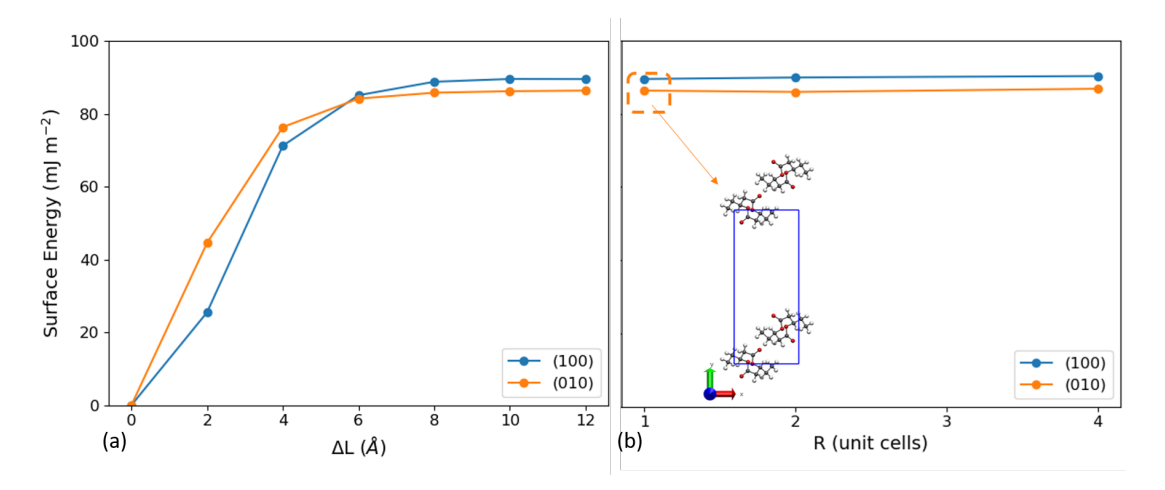


Figure B.4: Surface energy of PHV as a function of (a) vacuum layer thickness ΔL and (b) slab thickness R, for both the (100) and (010) surfaces.

has been removed from the unit cell and the box has been expanded by 12 Å in both the x and y dimensions.

B.2 Amorphous Polymer Simulations

B.2.1 Structure and Conformation

Table B.1 gives the ratios of the mean square end-to-end distance over the mean square radius of gyration, $R_{\rm e}^2/R_{\rm g}^2$, for amorphous PHB, PHV and PHVB systems

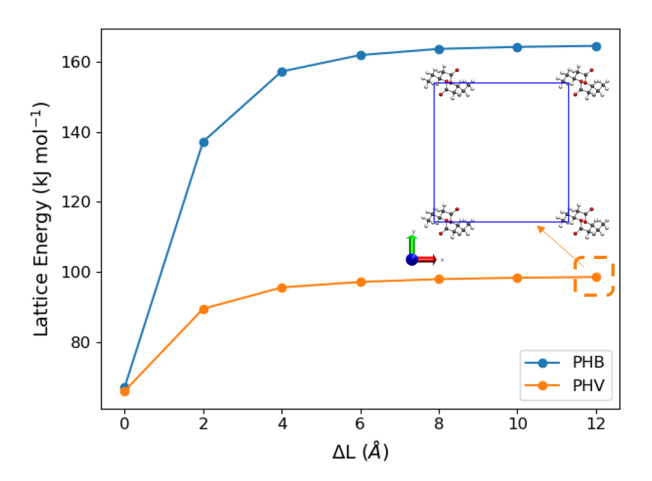


Figure B.5: Lattice energy of polymer crystals, where ΔL is the change in box length from the unit cell in x and y directions.

at 500 K. A ratio of ≈ 6 indicates the polymers melts have reached equilibration [110].

Polymer	M	$R_{ m e}^2/R_{ m g}^2$	
PHB	5	5.54	± 0.43
PHB	10	5.67	± 0.58
PHB	20	5.54	± 0.99
PHB	50	5.50	± 1.75
PHVB	10	5.71	± 0.58
PHV	10	5.53	± 0.62

Table B.1: Chain conformation properties of amorphous PHB, PHV and PHVB at $500~\mathrm{K}.$

B.2.2 Dynamical Properties

The $R_{\rm e}$ vector autocorrelation function with a fitted exponential decay, used to estimate the polymer decorrelation time τ , is shown in Figure B.6. τ was taken as the time required for the function to decay to 1/e.

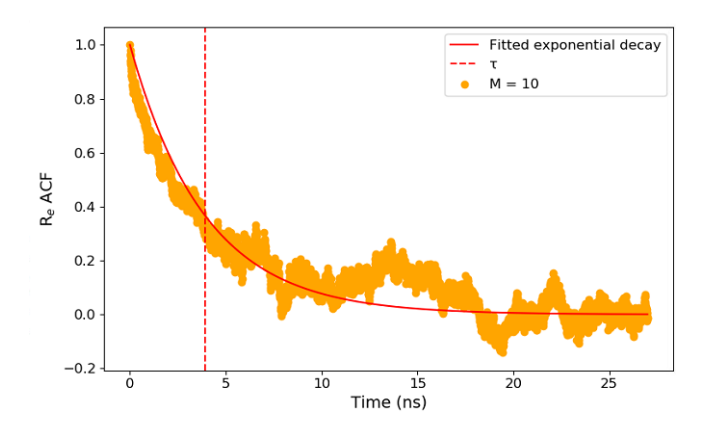


Figure B.6: End-to-end vector autocorrelation with fitted exponential decay.

B.2.3 Glass Transition

Figure B.7 shows block averaged densities for the PHB, PHV and PHVB (M = 10) systems.

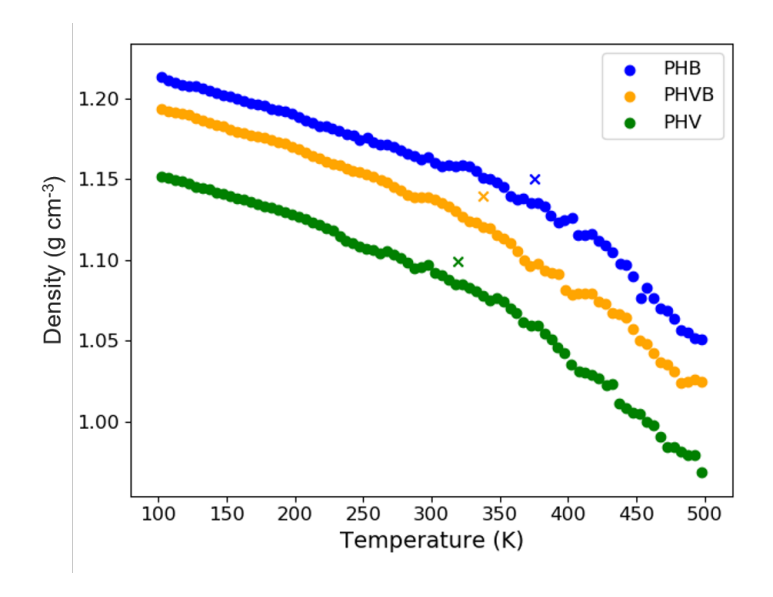


Figure B.7: Block averaged density vs temperature on cooling M=10 chains from 500 K to 100 K. The crosses mark the estimated $T_{\rm g}$ for each polymer. Block averaging was used only for visualisation purposes.

B.3 Diffusion Properties

A snapshot of the PHB and water system is shown in Figure B.8. Water molecules were inserted with random positions and orientations into the polymer matrix.

The density of each system with the permeant molecules inserted and equilibrated is given in Table B.2.

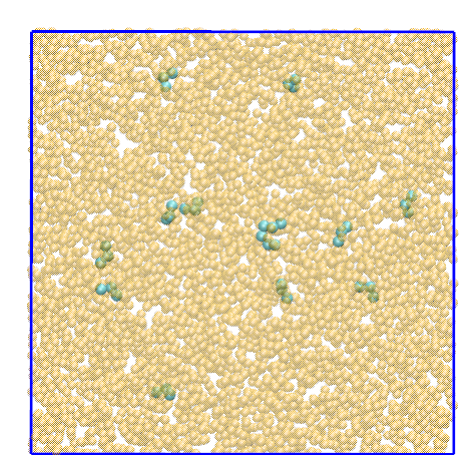


Figure B.8: Snapshot of water molecules (blue) within the amorphous PHB matrix (orange).

Polymer	M	Permeant	ρ (g o	em^{-3})
1 orymer	1V1	1 emieam	300 K	500 K
PHB	10	$\mathrm{H_{2}O}$	1.16	1.04
PHB	20	$\mathrm{H_{2}O}$	1.16	1.04
PHB	10	O_2	1.16	1.04
PHB	20	O_2	1.15	1.05
PHV	10	$\mathrm{H_{2}O}$	-	0.96
PHV	10	O_2	-	0.96

Table B.2: Density (ρ) of M-monomer systems at a temperature of 300 K or 500 K. Standard deviation in all systems is ≤ 0.01 g cm⁻³.

A short period at the start of the NVT simulation is not included in the calculation of diffusion coefficients as it shows anomalous diffusion corresponding to molecular vibrations. Likewise, the final portion of the trajectory is excluded due to poor statistics and increased noise. These sections are marked with green dashed lines in Figure B.9(a). Log-log plots of the MSD vs time data were also used to ensure the region chosen for calculation of D values represented Einstein diffusion [15]. A log-log plot for oxygen diffusion in PHB (M=10) is shown in Figure B.9(b).

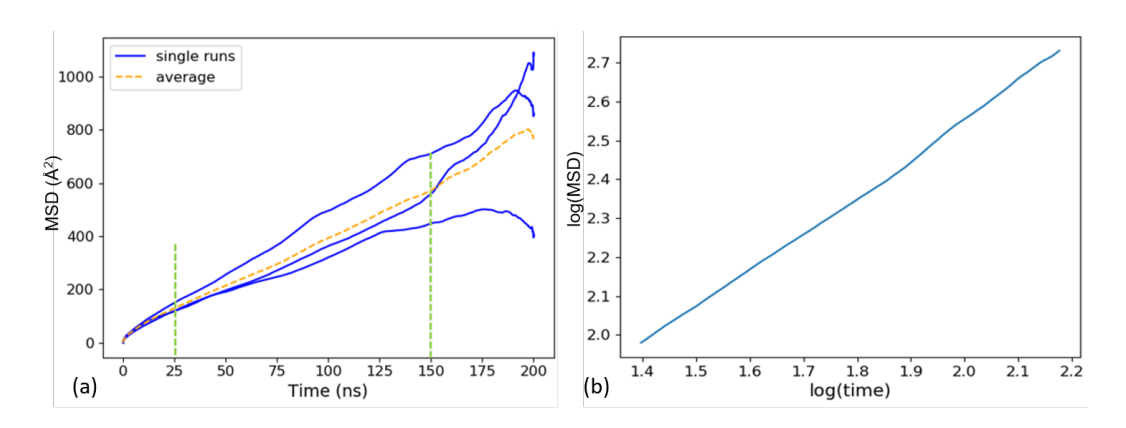


Figure B.9: (a) MSD data for oxygen in PHB with M=10 at 300 K, indicating the linear region in the middle of the graph used to compute the diffusion coefficient. (b) log-log plot of MSD data, with slope ≈ 1 indicating diffusion is in Einstein regime [15].

B.4 Finite Chain Crystal Model

Figure B.10 shows how the bulk finite chain PHB crystal model was created by removing two monomers from the infinite chain crystal model and replacing them with chain ends. The system was then replicated to create a bulk slab.

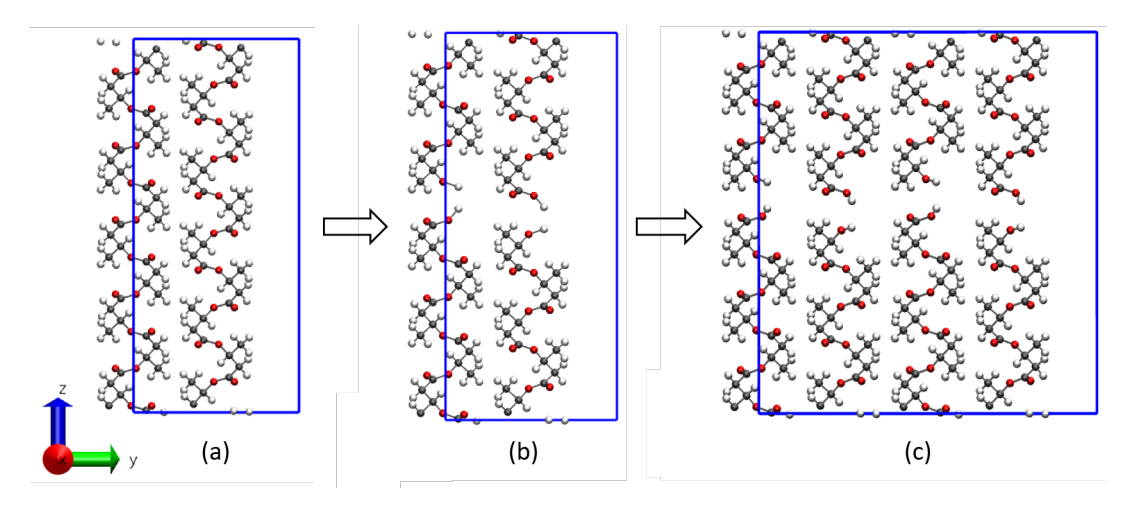


Figure B.10: (a) Infinite chain crystal containing five unit cells. (b) Finite chain model with free chain ends. (c) Finite chain crystal replicated into bulk slab.

B.5 Graphene Systems

Figures B.11 and B.12 show the density profiles for water and oxygen, respectively, from three independent runs. The average z position of the graphene sheets are also plotted.

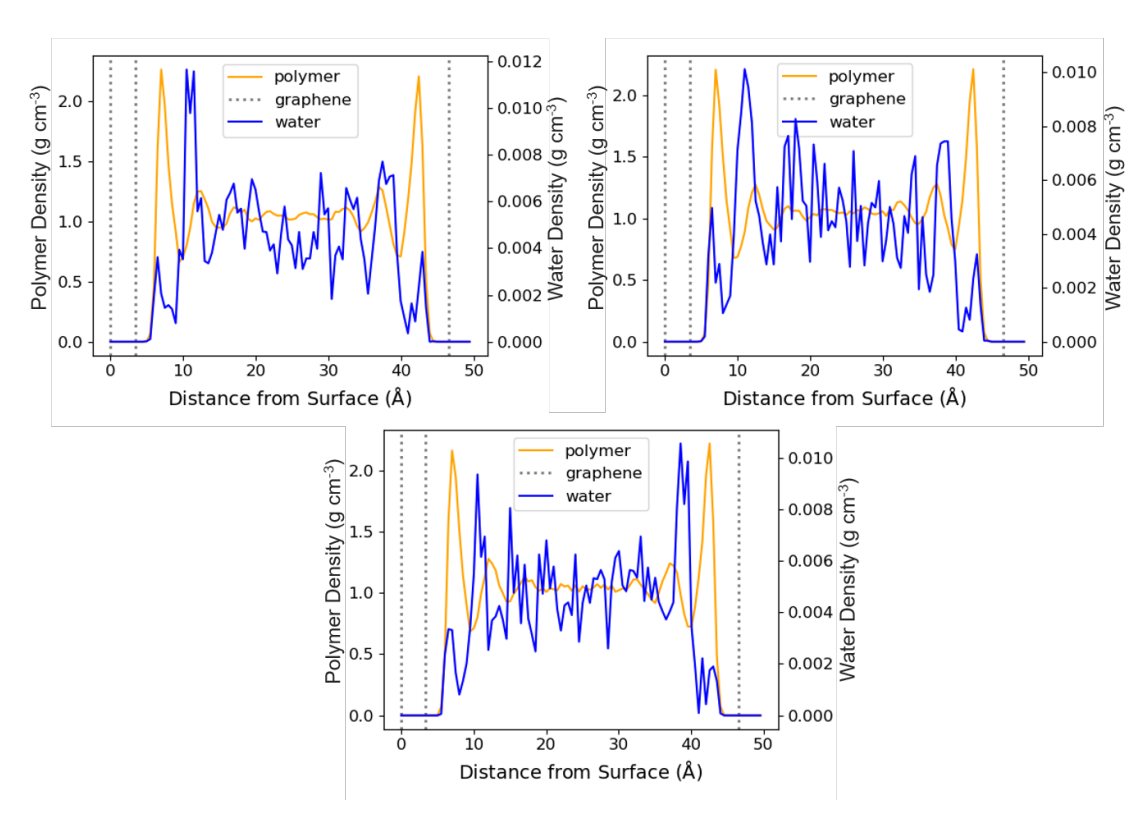


Figure B.11: Density profile plots from three water diffusion simulations. Density data was sampled every 1 ns from a 100 ns production run in the NVT ensemble at 500 K.

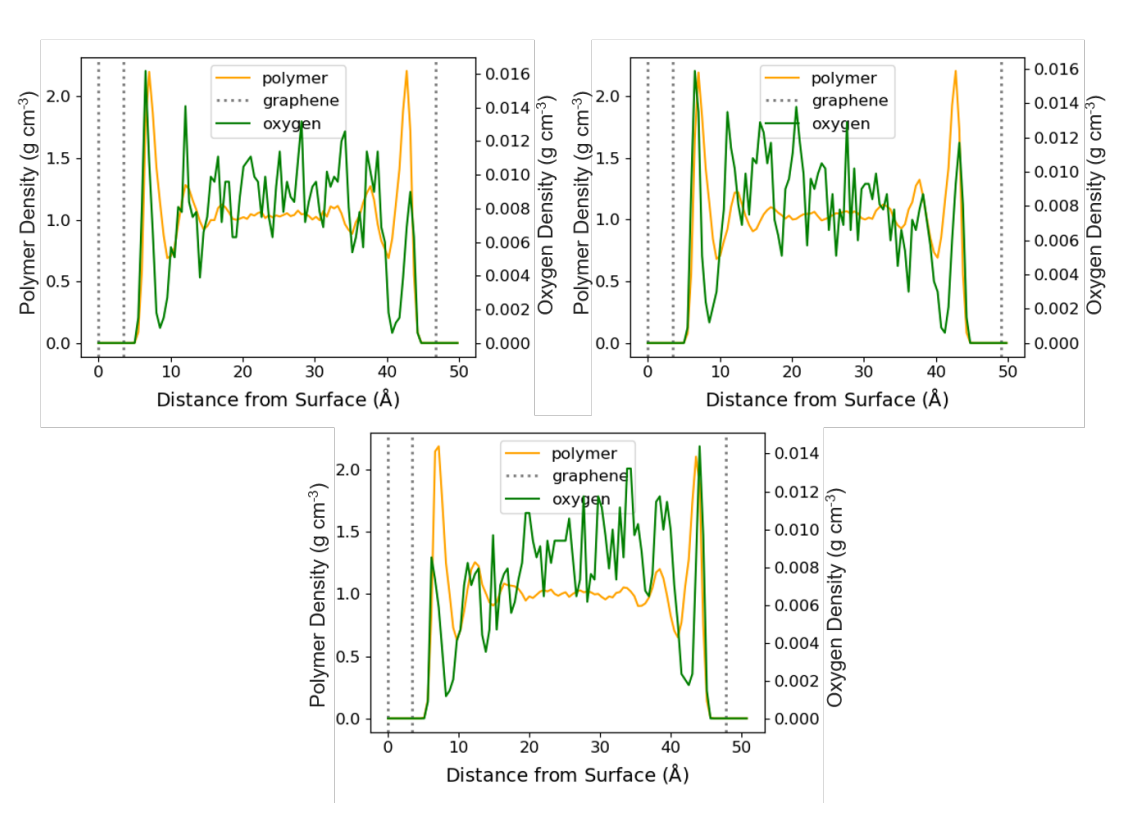


Figure B.12: Density profile plots from three oxygen diffusion simulations. Density data was sampled every 1 ns from a 100 ns production run in the NVT ensemble at $500~\rm{K}$.

Appendix C

Additional Experimental Results

This Appendix contains the tabulated results for each repeated experimental test, the averages of which are reported in Chapter 5.

C.1 Water Barrier Properties

C.1.1 Water Contact Angle

Contact angle measurements of water droplets on the polymer films are reported in Table C.1.

C.1.2 WVTR and Permeability

Water vapour transmission rate (WVTR) and water permeability results for the PHB films are given in Tables C.2 to C.7. Measurements for a PET film, used for validation of experimental setup, are given in Table C.8.

C.2 Crystallinity and Thermal Properties

Melting temperature $(T_{\rm m})$, crystallisation temperature $(T_{\rm c})$ and degree of crystallinity $(X_{\rm c})$ of the PHB films were measured using differential scanning calorimetry. Results are given in Tables C.9 to C.14.

C.3 Mechanical Properties

Mechanical properties of the PHB films were assessed using texture analysis testing. The force required to burst the films and the distance the films stretch before

	Water Contact Angle (°)				
	PHB	$\mathbf{PHB}_{-}\mathbf{TA}$	$\mathrm{PHB}_{-}\mathrm{TA}/\mathrm{1BN}$		
1	76	64	63		
2	74	63	64		
3	71	62	69		
4	71	62	60		
5	68	61	62		
ave.	72 ± 3	62 ± 1	64 ± 4		
	$PHB_{-}1BN$	$\mathrm{PHB}_0.25\mathrm{BN}$	$\mathrm{PHB}_0.06\mathrm{BN}$		
1	66	68	78		
2	62	64	65		
3	61	72	65		
4	58	77	66		
5	56	69	67		
ave.	60 ± 3	70 ± 5	68 ± 6		

Table C.1: Contact angle of water droplet placed on film surface.

	РНВ		
	WVTR Permeability		
	$({f g} \ {f m}^{-2} \ {f d}^{-1})$	(Barrer)	
1	66.5	1009	
2	54.0	820	
3	63.0	950	
ave.	61.0 ± 6.4	926 ± 97	

Table C.2: Water barrier properties of neat PHB.

bursting are given in Tables C.15 to C.20.

	$\mathrm{PHB}_{\scriptscriptstyle{-}}\mathrm{TA}$		
	WVTR Permeability		
	$({f g} \ {f m}^{-2} \ {f d}^{-1})$	(Barrer)	
1	104.2	1581	
2	101.5	1540	
3	95.3	1447	
ave.	100.3 ± 4.5	1523 ± 69	

Table C.3: Water barrier properties of PHB + 10 wt % TA.

	$\mathrm{PHB}_{-}\mathrm{TA}/\mathrm{1BN}$		
	WVTR Permeability		
	$({f g} \ {f m}^{-2} \ {f d}^{-1})$	(Barrer)	
1	1745.3	26489	
2	1728.6	26236	
3	1753.5	26614	
ave.	1742.5 ± 12.7	26446 ± 193	

Table C.4: Water barrier properties of PHB + 10 wt % TA + 1 wt % BN.

	$\mathrm{PHB}_{-1}\mathrm{BN}$		
	WVTR Permeabilit		
	$\left(\mathbf{g} \; \mathbf{m}^{-2} \; \mathbf{d}^{-1} \right)$	(Barrer)	
1	1773.1	26910	
2	1737.9	26376	
3	1568.4	23804	
ave.	1693.1 ± 109.4	25697 ± 1661	

Table C.5: Water barrier properties of PHB + 1 wt % BN.

	$\mathrm{PHB}_0.25\mathrm{BN}$		
	WVTR Permeability		
	$({f g} \ {f m}^{-2} \ {f d}^{-1})$	(Barrer)	
1	1700.5	25809	
2	1692.2	25682	
3	1921.5	29163	
ave.	1771.4 ± 130.1	26885 ± 1974	

Table C.6: Water barrier properties of PHB + 0.25 wt % BN.

	$\mathrm{PHB}_0.06\mathrm{BN}$	
	WVTR	Permeability
	$(\mathbf{g} \ \mathbf{m}^{-2} \ \mathbf{d}^{-1})$	(Barrer)
1	55.0	835
2	52.2	792
3	54.0	820
ave.	53.7 ± 1.4	815 ± 22

Table C.7: Water barrier properties of PHB + 0.0625 wt % BN.

	PET	
	WVTR Permeability	
	$({f g} \ {f m}^{-2} \ {f d}^{-1})$	(Barrer)
1	6.0	208.6
2	6.0	208.6
3	6.2	215.9
ave.	6.1 ± 0.1	211.0 ± 4.2

Table C.8: Water barrier properties of PET.

		PHB	
	$T_{\mathbf{m}}$ (\mathbf{K})	$T_{ m c} \; ({ m K})$	$X_{ m c}~(\%)$
1	451.52	355.23	41.30
2	451.37	359.43	43.30
3	451.02	369.96	38.31
ave.	451.3 ± 0.26	363.87 ± 5.45	40.97 ± 2.51

Table C.9: Thermal properties and crystallinity of neat PHB.

		$\mathrm{PHB}_{-}\mathrm{TA}$	
	$T_{\mathbf{m}}$ (\mathbf{K})	$T_{\mathbf{c}}$ (\mathbf{K})	$X_{ m c}~(\%)$
1	449.63	360.36	42.46
2	448.78	362.37	41.64
3	449.81	372.36	62.07
ave.	449.41 ± 0.55	365.03 ± 6.43	48.72 ± 11.57

Table C.10: Thermal properties and crystallinity of PHB + 10 wt % TA.

	$\mathrm{PHB}_{-}\mathrm{TA}/\mathrm{1BN}$		
	$T_{\mathbf{m}}$ (K)	$T_{ m c} \; ({ m K})$	$X_{ m c}~(\%)$
1	447.66	388.13	62.20
2	448.14	389.83	71.73
3	449.94	389.26	74.48
ave.	448.58 ± 1.20	389.07 ± 0.87	69.47 ± 6.45

Table C.11: Thermal properties and crystallinity of PHB + 10 wt % TA + 1 wt % BN.

		PHB_1BN	
	$T_{\mathbf{m}}$ (K)	$T_{ m c} \; ({ m K})$	$X_{ m c}~(\%)$
1	452.03	388.24	63.38
2	451.02	387.59	60.61
3	450.71	387.89	68.69
ave.	451.25 ± 0.69	387.91 ± 0.33	64.23 ± 4.11

Table C.12: Thermal properties and crystallinity of PHB + 1 wt % BN.

		$ m PHB_0.25BN$	
	$T_{ m m} \; ({ m K})$	$T_{ m c} \; ({ m K})$	$X_{ m c}~(\%)$
1	450.79	390.52	68.42
2	451.07	390.73	61.76
3	451.68	390.16	65.09
ave.	451.18 ± 0.46	390.47 ± 0.29	65.09 ± 3.33

Table C.13: Thermal properties and crystallinity of PHB + 0.25 wt % BN.

		PHB_0.06BN	
	$T_{\mathbf{m}}$ (K)	$T_{ m c} \; ({ m K})$	$X_{ m c}~(\%)$
1	451.89	387.47	70.06
2	452.08	387.27	72.64
3	450.90	390.03	71.16
ave.	451.62 ± 0.63	388.26 ± 1.54	71.28 ± 1.29

Table C.14: Thermal properties and crystallinity of PHB + 0.0625 wt % BN.

	РНВ	
	Force (mN)	Distance (mm)
1	1069	0.66
2	932	0.63
3	834	0.68
4	981	0.60
5	991	0.56
ave.	961 ± 88	0.63 ± 0.05

Table C.15: Force and distance to burst of neat PHB.

	$\mathrm{PHB}_{-}\mathrm{TA}$	
	Force (mN)	Distance (mm)
1	637	0.83
2	441	0.62
3	579	0.78
4	588	0.81
5	539	0.87
ave.	559 ± 69	0.78 ± 0.10

Table C.16: Force and distance to burst of PHB + 10 wt % TA.

	$\mathrm{PHB}_{-}\mathrm{TA}/\mathrm{1BN}$	
	Force (mN)	Distance (mm)
1	667	0.73
2	873	0.64
3	1030	0.87
4	843	0.69
5	912	0.67
ave.	863 ± 127	0.72 ± 0.09

Table C.17: Force and distance to burst of PHB + 10 wt % TA + 1 wt % BN.

	$\mathrm{PHB}_{-}1\mathrm{BN}$	
	Force (mN)	Distance (mm)
1	1049	0.60
2	834	0.52
3	1363	0.69
4	755	0.59
5	853	0.52
ave.	971 ± 245	0.58 ± 0.07

Table C.18: Force and distance to burst of PHB + 1 wt % BN.

	$\mathrm{PHB}_0.25\mathrm{BN}$	
	Force (mN)	Distance (mm)
1	932	0.95
2	1089	1.08
3	1157	1.07
4	1255	1.01
5	1383	1.00
ave.	1163 ± 167	1.02 ± 0.05

Table C.19: Force and distance to burst of PHB + 0.25 wt % BN.

	PHB_0.06BN	
	Force mN)	Distance (mm)
1	1422	0.84
2	1206	1.25
3	1157	0.68
4	1255	0.84
5	1383	0.89
ave.	1285 ± 118	0.90 ± 0.21

Table C.20: Force and distance to burst of PHB + 0.0625 wt % BN.

Bibliography

- [1] Statista. Plastic waste in the u.s. https://www.statista.com/study/60094/plastic-waste-in-the-us/, 2023. Accessed April 2025.
- [2] Waste and Resources Action Programme (WRAP). Roadmap 2025: Creating a circular economy for flexible plastic packaging. Technical report, Waste and Resources Action Programme, July 2024. Accessed April 2025.
- [3] Katarzyna Majerczak, Dominic Wadkin-Snaith, Vitor Magueijo, Paul Mulheran, John Liggat, and Karen Johnston. Polyhydroxybutyrate: a review of experimental and simulation studies of the effect of fillers on crystallinity and mechanical properties. *Polymer International*, 71(12):1398–1408, 2022.
- [4] Jinwu Wang, Douglas J Gardner, Nicole M Stark, Douglas W Bousfield, Mehdi Tajvidi, and Zhiyong Cai. Moisture and oxygen barrier properties of cellulose nanomaterial-based films. ACS Sustainable Chemistry & Engineering, 6(1):49–70, 2018.
- [5] AH Joshi, C Natarajan, SM Pawde, and NV Bhat. Grafting of cellophane films using magnetron-enhanced plasma polymerization. *Journal of applied polymer science*, 63(6):737–743, 1997.
- [6] Georgette L Siparsky, Kent J Voorhees, John R Dorgan, and Kevin Schilling. Water transport in polylactic acid (pla), pla/polycaprolactone copolymers, and pla/polyethylene glycol blends. *Journal of environmental polymer degradation*, 5:125–136, 1997.
- [7] Elodie Bugnicourt, Patrizia Cinelli, Andrea Lazzeri, and Vera Alejandra Alvarez. Polyhydroxyalkanoate (pha): Review of synthesis, characteristics, processing and potential applications in packaging. 2014.
- [8] Glykeria A Visvini, Georgios N Mathioudakis, Amaia Soto Beobide, Zoi Piperigkou, Aris E Giannakas, Stavros Messaritakis, Giannis Sotiriou, and George A Voyiatzis. Improvement of water vapor permeability in polypropylene composite films by the synergy of carbon nanotubes and β -nucleating agents. *Polymers*, 15(22):4432, 2023.

- [9] Paul E Keller and Richard T Kouzes. Water vapor permeation in plastics. Technical report, Pacific Northwest National Lab.(PNNL), Richland, WA (United States), 2017.
- [10] Michael P Allen et al. Introduction to molecular dynamics simulation. Computational soft matter: from synthetic polymers to proteins, 23(1):1–28, 2004.
- [11] Hai Wang and Kohji Tashiro. Reinvestigation of crystal structure and intermolecular interactions of biodegradable poly (3-hydroxybutyrate) α -form and the prediction of its mechanical property. *Macromolecules*, 49(2):581–594, 2016.
- [12] Artyom D. Glova, Stanislav G. Falkovich, Daniil I. Dmitrienko, Alexey V. Lyulin, Sergey V. Larin, Victor M. Nazarychev, Mikko Karttunen, and Sergey V. Lyulin. Scale-dependent miscibility of polylactide and polyhydroxybutyrate: Molecular dynamics simulations. *Macromolecules*, 51(2):552–563, 2018.
- [13] Mikio Terada and RH Marchessault. Determination of solubility parameters for poly (3-hydroxyalkanoates). *International Journal of Biological Macromolecules*, 25(1-3):207–215, 1999.
- [14] Alexander Kirillov, Eric Mintun, Nikhila Ravi, Hanzi Mao, Chloe Rolland, Laura Gustafson, Tete Xiao, Spencer Whitehead, Alexander C. Berg, Wan-Yen Lo, Piotr Dollár, and Ross Girshick. Segment anything, 2023.
- [15] Edward J Maginn, Richard A Messerly, Daniel J Carlson, Daniel R Roe, and J Richard Elliot. Best practices for computing transport properties 1. self-diffusivity and viscosity from equilibrium molecular dynamics [article v1. 0]. Living Journal of Computational Molecular Science, 1(1):6324–6324, 2019.
- [16] M Yokouchi, Y Chatani, H Tadokoro, K Teranishi, and H Tani. Structural studies of polyesters: 5. molecular and crystal structures of optically active and racemic poly (β -hydroxybutyrate). *Polymer*, 14(6):267–272, 1973.
- [17] Mitsuru Yokouchi, Yozo Chatani, Hiroyuki Tadokoro, and Hisaya Tani. Structural studies of polyesters. vii. molecular and crystal structures of racemic poly (β -ethyl- β -propiolactone). *Polymer Journal*, 6(3):248–255, 1974.
- [18] Nadege Follain, Corinne Chappey, Eric Dargent, Frederic Chivrac, Raphael Cretois, and Stephane Marais. Structure and barrier properties of biodegradable polyhydroxyalkanoate films. *The Journal of Physical Chemistry C*, 118(12):6165–6177, 2014.

- [19] Jin-San Yoon, Hae-Won Jung, Mal-Nam Kim, and Eun-Soo Park. Diffusion coefficient and equilibrium solubility of water molecules in biodegradable polymers. *Journal of applied polymer science*, 77(8):1716–1722, 2000.
- [20] Pekka Mark and Lennart Nilsson. Structure and dynamics of the tip3p, spc, and spc/e water models at 298 k. *The Journal of Physical Chemistry A*, 105(43):9954–9960, 2001.
- [21] Herman JC Berendsen, J-Raúl Grigera, and Tjerk P Straatsma. The missing term in effective pair potentials. *Journal of Physical Chemistry*, 91(24):6269–6271, 1987.
- [22] Matti Javanainen, Ilpo Vattulainen, and Luca Monticelli. On atomistic models for molecular oxygen. *The Journal of Physical Chemistry B*, 121(3):518–528, 2017.
- [23] Mary Vedamuthu, Surjit Singh, and G Wilse Robinson. Properties of liquid water: origin of the density anomalies. *The Journal of Physical Chemistry*, 98(9):2222–2230, 1994.
- [24] R Mills. Self-diffusion in normal and heavy water in the range 1-45. deg. *The Journal of Physical Chemistry*, 77(5):685–688, 1973.
- [25] Khaoula Houssini, Jinhui Li, and Quanyin Tan. Complexities of the global plastics supply chain revealed in a trade-linked material flow analysis. *Communications Earth & Environment*, 6(1):257, 2025.
- [26] The Ocean Cleanup. Ocean plastic pollution explained, 2024. Accessed April 2025.
- [27] Ioannis Antonopoulos, Giorgia Faraca, and Davide Tonini. Recycling of post-consumer plastic packaging waste in the eu: Recovery rates, material flows, and barriers. *Waste Management*, 126:694–705, 2021.
- [28] Oksana Horodytska, F Javier Valdés, and Andres Fullana. Plastic flexible films waste management—a state of art review. *Waste management*, 77:413—425, 2018.
- [29] Eunomia Research & Consulting. Flexible films market in europe: State of play. Technical report, Plastics Recyclers Europe, October 2022. Accessed April 2025.
- [30] Stephen Moss. The zero-waste revolution: how a new wave of shops could end excess packaging. *The Guardian*, April 2019. Accessed April 2025.

- [31] Food and Agriculture Organization of the United Nations. Food wastage footprint: Impacts on natural resources. https://www.fao.org/3/i3347e/i3347e.pdf, 2013. Accessed April 2025.
- [32] Waste and Resources Action Programme (WRAP). Food waste contributes 10% to global emissions but 9 out of 10 countries' ndcs fail to focus on food loss and waste, November 2024. Accessed April 2025.
- [33] U.S. Environmental Protection Agency. Understanding global warming potentials, 2025. Accessed April 2025.
- [34] British Plastics Federation. Standards for compostability, 2024. Accessed April 2025.
- [35] Nurul Aina Ismail, Syuhada Mohd Tahir, Norihan Yahya, Muhamad Firdaus Abdul Wahid, Nur Ezzati Khairuddin, Ibtihah Hashim, Nurfarhana Rosli, and Maryam Aqilah Abdullah. Synthesis and characterization of biodegradable starch-based bioplastics. In *Materials Science Forum*, volume 846, pages 673–678. Trans Tech Publ, 2016.
- [36] Xiang Qi, Yiwei Ren, and Xingzu Wang. New advances in the biodegradation of poly (lactic) acid. *International Biodeterioration & Biodegradation*, 117:215–223, 2017.
- [37] Jun Xu and Bao-Hua Guo. Poly (butylene succinate) and its copolymers: Research, development and industrialization. *Biotechnology journal*, 5(11):1149–1163, 2010.
- [38] S Ayu Rafiqah, Abdan Khalina, Ahmad Saffian Harmaen, Intan Amin Tawakkal, Khairul Zaman, M Asim, MN Nurrazi, and Ching Hao Lee. A review on properties and application of bio-based poly (butylene succinate). *Polymers*, 13(9):1436, 2021.
- [39] Verena Jost and Horst-Christian Langowski. Effect of different plasticisers on the mechanical and barrier properties of extruded cast phbv films. European Polymer Journal, 68:302–312, 2015.
- [40] Baki Hazer and Alexander Steinbüchel. Increased diversification of polyhydroxyalkanoates by modification reactions for industrial and medical applications. *Applied Microbiology and Biotechnology*, 74(1):1–12, 2007.
- [41] Helmut Brandl and Petra Püchner. Biodegradation of plastic bottles made from 'biopol'in an aquatic ecosystem under in situ conditions. *Biodegradation*, 2:237–243, 1991.

- [42] F Raquel Maia, Vitor M Correlo, Joaquim M Oliveira, and Rui L Reis. Natural origin materials for bone tissue engineering: Properties, processing, and performance. In *Principles of regenerative medicine*, pages 535–558. Elsevier, 2019.
- [43] M Lemoigne. Etudes sur l'autolyse microbienne acidification par formation d'acide β -oxybutyrique. Ann. Inst. Pasteur, 39:144–173, 1925.
- [44] PJ Barham. Nucleation behaviour of poly-3-hydroxy-butyrate. *Journal of materials science*, 19:3826–3834, 1984.
- [45] J Cornibert and RH Marchessault. Conformational isomorphism. a general 21 helical conformation for poly (β -alkanoates). *Macromolecules*, 8(3):296–305, 1975.
- [46] Michael C Zhang, Bao-Hua Guo, and Jun Xu. A review on polymer crystallization theories. *Crystals*, 7(1):4, 2016.
- [47] Carsten Dingler, Klaus Dirnberger, and Sabine Ludwigs. Semiconducting polymer spherulites—from fundamentals to polymer electronics. *Macro-molecular Rapid Communications*, 40(1):1800601, 2019.
- [48] Mael Kervran, Christelle Vagner, Marianne Cochez, Marc Ponçot, Mohammad Reza Saeb, and Henri Vahabi. Thermal degradation of polylactic acid (pla)/polyhydroxybutyrate (phb) blends: A systematic review. Polymer Degradation and Stability, 201:109995, 2022.
- [49] Katarzyna Majerczak and John J Liggat. Submission to journal of polymers and the environment evaluation of thermal properties and crystallinity in phb-based systems—a doe approach. *Journal of Polymers and the Environment*, pages 1–20, 2024.
- [50] Jayven Chee Chuan Yeo, Joseph K Muiruri, Warintorn Thitsartarn, Zibiao Li, and Chaobin He. Recent advances in the development of biodegradable phb-based toughening materials: Approaches, advantages and applications. *Materials Science and Engineering: C*, 92:1092–1116, 2018.
- [51] Deniz Aydemir and Douglas J Gardner. Biopolymer blends of polyhydroxybutyrate and polylactic acid reinforced with cellulose nanofibrils. *Carbohydrate polymers*, 250:116867, 2020.
- [52] LM Araque, TS Alves, and R Barbosa. Biodegradation of polyhydroxybutyrate and hollow glass microspheres composite films. *Journal of Applied Polymer Science*, 136(11):47195, 2019.

- [53] Estefanía Lidón Sánchez-Safont, Abdulaziz Aldureid, José María Lagarón, Jose Gamez-Perez, and Luis Cabedo. Effect of the purification treatment on the valorization of natural cellulosic residues as fillers in phb-based composites for short shelf life applications. Waste and Biomass Valorization, 12:2541–2556, 2021.
- [54] Rathish Rajan, PA Sreekumar, Kuruvilla Joseph, and Mikael Skrifvars. Thermal and mechanical properties of chitosan reinforced polyhydroxybutyrate composites. *Journal of applied polymer science*, 124(4):3357–3362, 2012.
- [55] WJ Orts, M Romansky, and JE Guillet. Measurement of the crystallinity of poly (β -hydroxybutyrate-co- β -hydroxyvalerate) copolymers by inverse gas chromatography. *Macromolecules*, 25(2):949–953, 1992.
- [56] Tizazu Mekonnen, Paolo Mussone, Hamdy Khalil, and David Bressler. Progress in bio-based plastics and plasticizing modifications. *Journal of Materials Chemistry A*, 1(43):13379–13398, 2013.
- [57] Jae Shin Choi and Won Ho Park. Effect of biodegradable plasticizers on thermal and mechanical properties of poly (3-hydroxybutyrate). *Polymer testing*, 23(4):455–460, 2004.
- [58] Katarzyna Majerczak and John Liggat. Evaluation of spherulite growth in phb-based systems—a doe approach. *Journal of Applied Polymer Science*, 140(40):1–17, 2023.
- [59] Jorge Arturo Soto Puente, Antonella Esposito, Frédéric Chivrac, and Eric Dargent. Effect of boron nitride as a nucleating agent on the crystallization of bacterial poly (3-hydroxybutyrate). *Journal of applied polymer science*, 128(5):2586–2594, 2013.
- [60] N Arul Manikandan, Kannan Pakshirajan, and G Pugazhenthi. Preparation and characterization of environmentally safe and highly biodegradable microbial polyhydroxybutyrate (phb) based graphene nanocomposites for potential food packaging applications. *International Journal of Biological Macromolecules*, 154:866–877, 2020.
- [61] Dana G Miloaga, Hazel-Ann A Hosein, Manjusri Misra, and Lawrence T Drzal. Crystallization of poly (3-hydroxybutyrate) by exfoliated graphite nanoplatelets. *Journal of applied polymer science*, 106(4):2548–2558, 2007.
- [62] R Crétois, Nadège Follain, Eric Dargent, J Soulestin, Serge Bourbigot, Stéphane Marais, and Laurent Lebrun. Microstructure and barrier properties of phbv/organoclays bionanocomposites. *Journal of Membrane Science*, 467:56–66, 2014.

- [63] Ching-Hung Lan and Yi-Ming Sun. Influence of the surface properties of nano-silica on the dispersion and isothermal crystallization kinetics of phb/silica nanocomposites. *Materials Chemistry and Physics*, 199:88–97, 2017.
- [64] Prodyut Dhar, Umesh Bhardwaj, Amit Kumar, and Vimal Katiyar. Poly (3-hydroxybutyrate)/cellulose nanocrystal films for food packaging applications: barrier and migration studies. *Polymer Engineering & Science*, 55(10):2388–2395, 2015.
- [65] Artyom D Glova, Sergey V Larin, Victor M Nazarychev, Mikko Karttunen, and Sergey V Lyulin. Grafted dipolar chains: Dipoles and restricted freedom lead to unexpected hairpins. *Macromolecules*, 53(1):29–38, 2020.
- [66] Zonglin Li, Junjun Kong, Lijing Han, Huiliang Zhang, and Lisong Dong. Effect of crystallinity on the thermal conductivity of poly (3-hydroxybutyrate)/bn composites. *Polymer Bulletin*, 75:1651–1666, 2018.
- [67] Robert E Kyles and Alan E Tonelli. Conformational characteristics of poly (d-β-hydroxybutyrate). *Macromolecules*, 36(4):1125–1131, 2003.
- [68] Kseniya Papchenko, Eleonora Ricci, and Maria Grazia De Angelis. Modelling across multiple scales to design biopolymer membranes for sustainable gas separations: 1—atomistic approach. *Polymers*, 15(7):1805, 2023.
- [69] Michael P Allen and Dominic J Tildesley. Computer simulation of liquids. Oxford university press, 2017.
- [70] A. P. Thompson, H. M. Aktulga, R. Berger, D. S. Bolintineanu, W. M. Brown, P. S. Crozier, P. J. in 't Veld, A. Kohlmeyer, S. G. Moore, T. D. Nguyen, R. Shan, M. J. Stevens, J. Tranchida, C. Trott, and S. J. Plimpton. LAMMPS a flexible simulation tool for particle-based materials modeling at the atomic, meso, and continuum scales. *Comp. Phys. Comm.*, 271:108171, 2022.
- [71] Richard J Gowers, Max Linke, Jonathan Barnoud, Tyler JE Reddy, Manuel N Melo, Sean L Seyler, Jan Domanski, David L Dotson, Sébastien Buchoux, Ian M Kenney, et al. Mdanalysis: a python package for the rapid analysis of molecular dynamics simulations. In *Proceedings of the 15th python in science conference*, volume 98, page 105. SciPy Austin, TX, 2016.
- [72] William Humphrey, Andrew Dalke, and Klaus Schulten. VMD Visual Molecular Dynamics. *Journal of Molecular Graphics*, 14:33–38, 1996.

- [73] James W Eastwood, Roger Williams Hockney, and DN Lawrence. P3m3dpthe three-dimensional periodic particle-particle/particle-mesh program. Computer Physics Communications, 19(2):215–261, 1980.
- [74] Junmei Wang, Romain M Wolf, James W Caldwell, Peter A Kollman, and David A Case. Development and testing of a general amber force field. Journal of computational chemistry, 25(9):1157–1174, 2004.
- [75] Scott J Weiner, Peter A Kollman, David A Case, U Chandra Singh, Caterina Ghio, Guliano Alagona, Salvatore Profeta, and Paul Weiner. A new force field for molecular mechanical simulation of nucleic acids and proteins. Journal of the American Chemical Society, 106(3):765–784, 1984.
- [76] Maarten Boomstra, Bernard Geurts, and Alexey Lyulin. Molecular weight segregation and thermal conductivity of polydisperse wax–graphene nanocomposites. *Polymers*, 15(9):2175, 2023.
- [77] Zeshuai Yuan, Zixing Lu, Zhenyu Yang, Jian Sun, and Fan Xie. A criterion for the normal properties of graphene/polymer interface. *Computational Materials Science*, 120:13–20, 2016.
- [78] Chang-Tsan Lu, Asanka Weerasinghe, Dimitrios Maroudas, and Ashwin Ramasubramaniam. A comparison of the elastic properties of graphene-and fullerene-reinforced polymer composites: the role of filler morphology and size. *Scientific reports*, 6(1):31735, 2016.
- [79] Ying Li, Martin Kroger, and Wing Kam Liu. Nanoparticle geometrical effect on structure, dynamics and anisotropic viscosity of polyethylene nanocomposites. *Macromolecules*, 45(4):2099–2112, 2012.
- [80] M. J. Frisch, G. W. Trucks, H. B. Schlegel, G. E. Scuseria, M. A. Robb, J. R. Cheeseman, G. Scalmani, V. Barone, G. A. Petersson, H. Nakatsuji, X. Li, M. Caricato, A. V. Marenich, J. Bloino, B. G. Janesko, R. Gomperts, B. Mennucci, H. P. Hratchian, J. V. Ortiz, A. F. Izmaylov, J. L. Sonnenberg, D. Williams-Young, F. Ding, F. Lipparini, F. Egidi, J. Goings, B. Peng, A. Petrone, T. Henderson, D. Ranasinghe, V. G. Zakrzewski, J. Gao, N. Rega, G. Zheng, W. Liang, M. Hada, M. Ehara, K. Toyota, R. Fukuda, J. Hasegawa, M. Ishida, T. Nakajima, Y. Honda, O. Kitao, H. Nakai, T. Vreven, K. Throssell, J. A. Montgomery, Jr., J. E. Peralta, F. Ogliaro, M. J. Bearpark, J. J. Heyd, E. N. Brothers, K. N. Kudin, V. N. Staroverov, T. A. Keith, R. Kobayashi, J. Normand, K. Raghavachari, A. P. Rendell, J. C. Burant, S. S. Iyengar, J. Tomasi, M. Cossi, J. M. Millam, M. Klene, C. Adamo, R. Cammi, J. W. Ochterski, R. L. Martin, K. Morokuma, O. Farkas, J. B. Foresman, and D. J. Fox. Gaussian 16 Revision C.01, 2016. Gaussian Inc. Wallingford CT.

- [81] Junmei Wang, Wei Wang, Peter A Kollman, David A Case, et al. Antechamber: an accessory software package for molecular mechanical calculations. J. Am. Chem. Soc, 222(1):2001, 2001.
- [82] Suleyman Selim Cinaroglu and Philip C Biggin. Evaluating the performance of water models with host–guest force fields in binding enthalpy calculations for cucurbit [7] uril–guest systems. The Journal of Physical Chemistry B, 125(6):1558–1567, 2021.
- [83] Konstantinos D Papavasileiou, Othonas A Moultos, and Ioannis G Economou. Predictions of water/oil interfacial tension at elevated temperatures and pressures: A molecular dynamics simulation study with biomolecular force fields. Fluid Phase Equilibria, 476:30–38, 2018.
- [84] Kara K Grotz and Nadine Schwierz. Optimized magnesium force field parameters for biomolecular simulations with accurate solvation, ion-binding, and water-exchange properties in spc/e, tip3p-fb, tip4p/2005, tip4p-ew, and tip4p-d. Journal of chemical theory and computation, 18(1):526–537, 2021.
- [85] Jasmine C Lightfoot, Antoine Buchard, Bernardo Castro-Dominguez, and Stephen C Parker. Comparative study of oxygen diffusion in polyethylene terephthalate and polyethylene furanoate using molecular modeling: computational insights into the mechanism for gas transport in bulk polymer systems. *Macromolecules*, 55(2):498–510, 2021.
- [86] William G Hoover. Canonical dynamics: Equilibrium phase-space distributions. *Physical review A*, 31(3):1695, 1985.
- [87] Glenn J Martyna, Douglas J Tobias, and Michael L Klein. Constant pressure molecular dynamics algorithms. *J. chem. Phys*, 101(4177):10–1063, 1994.
- [88] R Klessig and E Polak. Efficient implementations of the polak–ribière conjugate gradient algorithm. SIAM Journal on Control, 10(3):524–549, 1972.
- [89] B Jaidhan, P Srinivasa Rao, and Allam Apparao. Energy minimization and conformation analysis of molecules using steepest descent method. *Int J Comput Sci Inf Technol*, 5(3):3525–3528, 2014.
- [90] Kumar Sudesh, Hideki Abe, and Yoshiharu Doi. Synthesis, structure and properties of polyhydroxyalkanoates: biological polyesters. *Progress in polymer science*, 25(10):1503–1555, 2000.
- [91] Hiroshi Mitomo, Peter J Barham, and Andrew Keller. Crystallization and morphology of poly (β -hydroxybutyrate) and its copolymer. *Polymer Journal*, 19(11):1241–1253, 1987.

- [92] Nicolas Jacquel, Chi-Wei Lo, Ho-Shing Wu, Yu-Hong Wei, and Shaw S Wang. Solubility of polyhydroxyalkanoates by experiment and thermodynamic correlations. *AIChE journal*, 53(10):2704–2714, 2007.
- [93] Valentina Siracusa, Svetlana Karpova, Anatoliy Olkhov, Anna Zhulkina, Regina Kosenko, and Alexey Iordanskii. Gas transport phenomena and polymer dynamics in phb/pla blend films as potential packaging materials. *Polymers*, 12(3):647, 2020.
- [94] O Miguel, MJ Fernandez-Berridi, and JJ Iruin. Survey on transport properties of liquids, vapors, and gases in biodegradable poly (3-hydroxybutyrate)(phb). *Journal of applied polymer science*, 64(9):1849–1859, 1997.
- [95] Valentina Siracusa, Carlo Ingrao, Svetlana G Karpova, Anatoly A Olkhov, and Alexey L Iordanskii. Gas transport and characterization of poly (3 hydroxybutyrate) films. *European Polymer Journal*, 91:149–161, 2017.
- [96] Viviana P Cyras, Ma Soledad Commisso, Adriana N Mauri, and Analía Vázquez. Biodegradable double-layer films based on biological resources: Polyhydroxybutyrate and cellulose. *Journal of Applied Polymer Science*, 106(2):749–756, 2007.
- [97] Guoxiang Cheng, Zhijiang Cai, and Ling Wang. Biocompatibility and biodegradation of poly (hydroxybutyrate)/poly (ethylene glycol) blend films. *Journal of Materials Science: Materials in Medicine*, 14(12):1073–1078, 2003.
- [98] Renate MR Wellen, Marcelo S Rabello, Guilhermino JM Fechine, and Eduardo L Canedo. The melting behaviour of poly (3-hydroxybutyrate) by dsc. reproducibility study. *Polymer testing*, 32(2):215–220, 2013.
- [99] ASTM International. Standard test methods for gravimetric determination of water vapor transmission rate of materials. ANSI, 2016.
- [100] H Yasuda. Units of gas permeability constants. *Journal of Applied Polymer Science*, 19(9):2529–2536, 1975.
- [101] Goodfellow. Properties of polyethylene terephthalate polyester (pet, petp). Technical report, Azo Materials, www.azom.com/article.aspx?ArticleID=2047, 2003. accessed on 16/01/25.
- [102] MJ Kloppers, Francesco Bellucci, RM Latanision, and JE Brennan. Transport and dielectric properties of poly (ethylene terephthalate) as determined via electrochemical techniques. *Journal of applied polymer science*, 48(12):2197–2205, 1993.

- [103] Michiel De Smet. The new plastics economy—rethinking the future of plastics. In European Conference on Plastics in Freshwater Environments 21–22 June 2016 in Berlin, page 51, 2016.
- [104] Rajendran Muthuraj, Oscar Valerio, and Tizazu H Mekonnen. Recent developments in short-and medium-chain-length polyhydroxyalkanoates: Production, properties, and applications. *International Journal of Biological Macromolecules*, 187:422–440, 2021.
- [105] Christopher Thellen, Sarah Cheney, and Jo Ann Ratto. Melt processing and characterization of polyvinyl alcohol and polyhydroxyalkanoate multilayer films. *Journal of applied polymer science*, 127(3):2314–2324, 2013.
- [106] Katarzyna Majerczak, Dominic Wadkin-Snaith, Vitor Magueijo, Paul Mulheran, John Liggat, and Karen Johnston. Polyhydroxybutyrate: a review of experimental and simulation studies of the effect of fillers on crystallinity and mechanical properties. *Polymer International*, 71(12):1398–1408, 2022.
- [107] Andrew I. Jewett, David Stelter, Jason Lambert, Shyam M. Saladi, Otello M. Roscioni, Matteo Ricci, Ludovic Autin, Martina Maritan, Saeed M. Bashusqeh, Tom Keyes, Remus T. Dame, Joan-Emma Shea, Grant J. Jensen, and David S. Goodsell. Moltemplate: A tool for coarse-grained modeling of complex biological matter and soft condensed matter physics. *Journal of Molecular Biology*, 433(11):166841, 2021. Computation Resources for Molecular Biology.
- [108] Alexei Nikitin. Non-zero lennard-jones parameters for the toukan—rahman water model: more accurate calculations of the solvation free energy of organic substances. *Journal of Computer-Aided Molecular Design*, 34(4):437—441, 2020.
- [109] David L Mobley, Caitlin C Bannan, Andrea Rizzi, Christopher I Bayly, John D Chodera, Victoria T Lim, Nathan M Lim, Kyle A Beauchamp, David R Slochower, Michael R Shirts, et al. Escaping atom types in force fields using direct chemical perception. *Journal of chemical theory and computation*, 14(11):6076–6092, 2018.
- [110] Michael Rubinstein and Ralph H. Colby. *Polymer Physics*. Oxford University Press, 2003.
- [111] Thomas E Gartner III and Arthi Jayaraman. Modeling and simulations of polymers: a roadmap. *Macromolecules*, 52(3):755–786, 2019.
- [112] Jr. Billmeyer, Fred W. Lattice Energy of Crystalline Polyethylene. *Journal of Applied Physics*, 28(10):1114–1118, 10 1957.

- [113] Chun-Sheng Liu, Ghanshyam Pilania, Chenchen Wang, and Ramamurthy Ramprasad. How critical are the van der waals interactions in polymer crystals? *The Journal of Physical Chemistry A*, 116(37):9347–9352, 2012.
- [114] Katsuhito Mori, Shota Mukoyama, Ying Zhang, Harumi Sato, Yukihiro Ozaki, Hikaru Terauchi, Isao Noda, and Isao Takahashi. Crystalline lamellae and surface morphology of biodegradable polyhydroxyalkanoate thin films: thermal behavior and comparison between poly (3-hydroxybutyrate-co-3-hydroxyhexanoate) and poly (3-hydroxybutyrate). *Macromolecules*, 41(5):1713–1719, 2008.
- [115] P Slepička, S Stýblová, N Slepičková Kasálková, S Rimpelova, and V Švorčík. Cytocompatibility of polyhydroxybutyrate modified by plasma discharge. *Polymer Engineering & Science*, 54(6):1231–1238, 2014.
- [116] DS Syromotina, Roman A Surmenev, Maria A Surmeneva, AN Boyandin, ED Nikolaeva, O Prymak, Matthias Epple, M Ulbricht, Christian Oehr, and TG Volova. Surface wettability and energy effects on the biological performance of poly-3-hydroxybutyrate films treated with rf plasma. *Materials Science and Engineering: C*, 62:450–457, 2016.
- [117] BMP Ferreira, LMP Pinheiro, PAP Nascente, MJ Ferreira, and EAR Duek. Plasma surface treatments of poly (l-lactic acid)(plla) and poly (hydroxybutyrate-co-hydroxyvalerate)(phbv). *Materials Science and Engineering:* C, 29(3):806–813, 2009.
- [118] Ahmad Rezaei Kolahchi, Abdellah Ajji, and Pierre J Carreau. Enhancing hydrophilicity of polyethylene terephthalate surface through melt blending. *Polymer Engineering & Science*, 55(2):349–358, 2015.
- [119] Yi-Hsuan Huang, Yun Chang, Cheng-Jyun Huang, Jhih-Min Lin, Shih-Huang Tung, Guang-Way Jang, and Cheng-Liang Liu. Electrospun biomass polyethylene furanoate nonwoven substrates for flexible thermoelectric generators. *Polymer*, 312:127619, 2024.
- [120] PA Barker, F Mason, and PJ d Barham. Density and crystallinity of poly (3-hydroxybutyrate/3-hydroxyvalerate) copolymers. *Journal of materials science*, 25:1952–1956, 1990.
- [121] Thomas G Fox Jr and Paul J Flory. Second-order transition temperatures and related properties of polystyrene. i. influence of molecular weight. *Journal of Applied Physics*, 21(6):581–591, 1950.
- [122] Katharina Vollmayr, Walter Kob, and Kurt Binder. How do the properties of a glass depend on the cooling rate? a computer simulation study of a

- lennard-jones system. The Journal of chemical physics, 105(11):4714–4728, 1996.
- [123] Joachim Buchholz, Wolfgang Paul, Fathollah Varnik, and Kurt Binder. Cooling rate dependence of the glass transition temperature of polymer melts: Molecular dynamics study. *The Journal of chemical physics*, 117(15):7364–7372, 2002.
- [124] David McKechnie, Jordan Cree, Dominic Wadkin-Snaith, and Karen Johnston. Glass transition temperature of a polymer thin film: Statistical and fitting uncertainties. *Polymer*, 195:122433, 2020.
- [125] Roohi, Mohd Rehan Zaheer, and Mohammed Kuddus. Phb (poly-β-hydroxybutyrate) and its enzymatic degradation. Polymers for Advanced Technologies, 29(1):30–40, 2018.
- [126] Omar Atiq, Eleonora Ricci, Marco Giacinti Baschetti, and Maria Grazia De Angelis. Modelling solubility in semi-crystalline polymers: a critical comparative review. *Fluid Phase Equilibria*, 556:113412, 2022.
- [127] Yuji Sasanuma and Shiori Katsumata. Elucidation of conformational characteristics and configurational properties of poly ((r)-3-hydroxybutyrate) by ab initio statistical mechanics. *Polymer journal*, 45(7):727–737, 2013.
- [128] G Beaucage, S Rane, S Sukumaran, MM Satkowski, LA Schechtman, and Y Doi. Persistence length of isotactic poly (hydroxy butyrate). *Macromolecules*, 30(14):4158–4162, 1997.
- [129] Hisao Takeuchi. A jump motion of small molecules in glassy polymers: A molecular dynamics simulation. *The Journal of chemical physics*, 93(3):2062–2067, 1990.
- [130] Florian Müller-Plathe. Diffusion of penetrants in amorphous polymers: A molecular dynamics study. *The Journal of chemical physics*, 94(4):3192–3199, 1991.
- [131] D Hofmann, L Fritz, J Ulbrich, and D Paul. Molecular simulation of small molecule diffusion and solution in dense amorphous polysiloxanes and polyimides. *Computational and Theoretical Polymer Science*, 10(5):419–436, 2000.
- [132] Christoph Schick, Andreas Wurm, and Alaa Mohammed. Formation and disappearance of the rigid amorphous fraction in semicrystalline polymers revealed from frequency dependent heat capacity. *Thermochimica Acta*, 396(1-2):119–132, 2003.

- [133] Nisha Middleton, Dominic Wadkin-Snaith, Karen Johnston, and Paul Mulheran. A versatile molecular dynamics force field for modelling polyhydroxyalkanoate structure and barrier properties. Manuscript under review at Journal of Macromolecular Theory and Simulations, 2025.
- [134] Shain J Doong and WS Winston Ho. Diffusion of hydrocarbons in polyethylene. *Industrial & engineering chemistry research*, 31(4):1050–1060, 1992.
- [135] Alan S Michaels, Wolf R Vieth, and James A Barrie. Diffusion of gases in polyethylene terephthalate. *Journal of Applied Physics*, 34(1):13–20, 1963.
- [136] MW Boomstra, BJ Geurts, and AV Lyulin. Reducing kapitza resistance of graphene-paraffin interfaces by alkyl functionalisation. *Chemical Physics Letters*, 846:141341, 2024.
- [137] Rasha Alqus, Stephen J Eichhorn, and Richard A Bryce. Molecular dynamics of cellulose amphiphilicity at the graphene–water interface. *Biomacro-molecules*, 16(6):1771–1783, 2015.
- [138] ER Azhagiya Singam, Yuntao Zhang, Geraldine Magnin, Ingrid Miranda-Carvajal, Logan Coates, Ravindra Thakkar, Horacio Poblete, and Jeffrey Comer. Thermodynamics of adsorption on graphenic surfaces from aqueous solution. *Journal of chemical theory and computation*, 15(2):1302–1316, 2018.
- [139] Oscar M Matus Rivas and Alejandro D Rey. Molecular dynamics on the self-assembly of mesogenic graphene precursors. *Carbon*, 110:189–199, 2016.
- [140] Gao Yang, Lihua Li, Wing Bun Lee, and Man Cheung Ng. Structure of graphene and its disorders: a review. Science and technology of advanced materials, 19(1):613–648, 2018.
- [141] Xiaobin Chen, Fuyang Tian, Clas Persson, Wenhui Duan, and Nan-xian Chen. Interlayer interactions in graphites. *Scientific reports*, 3(1):3046, 2013.
- [142] Baris Demir, Luke C Henderson, and Tiffany R Walsh. Design rules for enhanced interfacial shear response in functionalized carbon fiber epoxy composites. ACS applied materials & interfaces, 9(13):11846–11857, 2017.
- [143] Siva Dasetty, John K Barrows, and Sapna Sarupria. Adsorption of amino acids on graphene: assessment of current force fields. *Soft Matter*, 15(11):2359–2372, 2019.

- [144] Efrem Braun, Seyed Mohamad Moosavi, and Berend Smit. Anomalous effects of velocity rescaling algorithms: the flying ice cube effect revisited. Journal of chemical theory and computation, 14(10):5262–5272, 2018.
- [145] Karen Johnston and Vagelis Harmandaris. Hierarchical multiscale modeling of polymer–solid interfaces: Atomistic to coarse-grained description and structural and conformational properties of polystyrene–gold systems. *Macromolecules*, 46(14):5741–5750, 2013.
- [146] Akarsh Verma, Avinash Parashar, and M Packirisamy. Atomistic modeling of graphene/hexagonal boron nitride polymer nanocomposites: a review. Wiley Interdisciplinary Reviews: Computational Molecular Science, 8(3):e1346, 2018.
- [147] Alistair J Anderson and EA372789 Dawes. Occurrence, metabolism, metabolic role, and industrial uses of bacterial polyhydroxyalkanoates. *Microbiological reviews*, 54(4):450–472, 1990.
- [148] Zulfiqar Ali Raza, Shanza Khalil, and Sharjeel Abid. Recent progress in development and chemical modification of poly (hydroxybutyrate)-based blends for potential medical applications. *International Journal of Biological Macromolecules*, 160:77–100, 2020.
- [149] Dongju Lee, Sung Ho Song, Jaewon Hwang, Sung Hwan Jin, Kwang Hyun Park, Bo Hyun Kim, Soon Hyung Hong, and Seokwoo Jeon. Enhanced mechanical properties of epoxy nanocomposites by mixing noncovalently functionalized boron nitride nanoflakes. *Small*, 9(15):2602–2610, 2013.
- [150] Shichao Wang, Wei Chen, Hengxue Xiang, Junjie Yang, Zhe Zhou, and Meifang Zhu. Modification and potential application of short-chain-length polyhydroxyalkanoate (scl-pha). *Polymers*, 8(8):273, 2016.
- [151] Mayte M Quispe, Olivia V Lopez, Dhahabia Abdallah Boina, Jean-François Stumbé, and Marcelo A Villar. Glycerol-based additives of poly (3-hydroxybutyrate) films. *Polymer Testing*, 93:107005, 2021.
- [152] Food Standards Agency. Approved additives and e numbers. Online, December 2024.
- [153] Dominic Wadkin-Snaith, Paul Mulheran, and Karen Johnston. Filler-induced heterogeneous nucleation of polymer crystals investigated by molecular dynamics simulations. *Polymer*, 281:126113, 2023.
- [154] Yingke Wu, Jianzhong Ma, Chao Liu, and Hongxia Yan. Surface modification design for improving the strength and water vapor permeability of

- waterborne polymer/sio2 composites: Molecular simulation and experimental analyses. *Polymers*, 12(1):170, 2020.
- [155] Hanna Nosal, Kevin Moser, Marek Warzała, Andrei Holzer, Dorota Stańczyk, and Ewa Sabura. Selected fatty acids esters as potential phb-v bioplasticizers: Effect on mechanical properties of the polymer. *Journal of Polymers and the Environment*, 29:38–53, 2021.
- [156] Alessandro Bonifacio, Lorenzo Bonetti, Etienne Piantanida, and Luigi De Nardo. Plasticizer design strategies enabling advanced applications of cellulose acetate. *European Polymer Journal*, 197:112360, 2023.
- [157] Dafne Crutchik, Oscar Franchi, Luis Caminos, David Jeison, Marisol Belmonte, Alba Pedrouso, Angeles Val del Rio, Anuska Mosquera-Corral, and José Luis Campos. Polyhydroxyalkanoates (phas) production: a feasible economic option for the treatment of sewage sludge in municipal wastewater treatment plants? Water, 12(4):1118, 2020.
- [158] Fernando Morgan-Sagastume, Sara Heimersson, Giuseppe Laera, Alan Werker, and Magdalena Svanström. Techno-environmental assessment of integrating polyhydroxyalkanoate (pha) production with services of municipal wastewater treatment. *Journal of Cleaner Production*, 137:1368–1381, 2016.